

# Fixed Pattern Noise Compensation in a Mercury Cadmium Telluride Infrared Focal Plane Array

by

**Praven Reddy**

Submitted to the Department of Electrical Engineering  
in partial fulfilment of the requirements for the degree of

**Master of Science in Engineering**

at the

**University of Cape Town**

September 1998

© University of Cape Town 1998

Signature of Author .....

Signed by candidate

Digital Image Processing Research Group  
Department of Electrical Engineering  
30 September 1998

Certified by .....

Prof. Gerhard de Jager  
Digital Image Processing Research Group

Accepted by .....

Prof. Barry J. Downing  
Head of Department Electrical Engineering

The copyright of this thesis vests in the author. No quotation from it or information derived from it is to be published without full acknowledgement of the source. The thesis is to be used for private study or non-commercial research purposes only.

Published by the University of Cape Town (UCT) in terms of the non-exclusive license granted to UCT by the author.

# Declaration

I declare that this dissertation is my own work. It is being submitted for the Degree of Master of Science in Engineering at the University of Cape Town. It has not been submitted before for any other degree or examination at this or any other university.

Signed by candidate

**Praven Reddy**

(Signature of Candidate)

# Acknowledgements

I would like to thank the following people for the time, effort and assistance they offered:

- My supervisor, Professor Gerhard de Jager, for his support and guidance during the project period.
- My Parents, Mully and my sister Melissa.
- My good friends Jayavani and Amaran. Thank you both for the inspiration and spiritual guidance.
- All of my cousins, especially Urishka, Jerusha and Prieshka.
- All the members of the Digital Image Processing Research Group for their patience, support and enthusiasm. Thanks especially to Marc, Willie, Jerome, Philip, Ben, Karen, Fred, Brendt, Brian and Yon.
- Kentron, for sponsoring this project.
- Moe, Dip 5 and, most importantly, Dip 2. Without you guys, I would not have got any work done. Thank you for the multi-tasking and all of the background processes.

# Abstract

*This thesis describes techniques for the correction of spatial noise artifacts in a mercury cadmium telluride infrared camera system. The spatial noise artifacts are a result of nonuniformities within the infrared focal plane detector array. The techniques presented dispense with the need for traditional temperature references, and provide nonuniformity compensation by using only the statistics of the moving infrared scene and motion of the camera assembly for calibration.*

*Frame averaging is employed, assuming that all of the detector pixels will eventually be irradiated with the same levels of incident flux after some extended period of time. Using a statistical analysis of the camera image data, the correction coefficients are re-calculated and updated. These techniques also ensure that the calculated coefficients continually track the variations in the dark currents as well as temperature changes within the dewar sensor cooling vessel.*

*These scene-based reference free approaches to the calculation of compensation coefficients in the infrared camera are shown to be successful in compensating for the effects of fixed pattern spatial noise.*

# Contents

<b>Declaration</b>	<b>i</b>
<b>Acknowledgements</b>	<b>ii</b>
<b>Abstract</b>	<b>iii</b>
<b>List of Figures</b>	<b>xii</b>
<b>List of Tables</b>	<b>xiv</b>
<b>Glossary</b>	<b>xv</b>
<b>List of Symbols</b>	<b>xvi</b>
<b>1 Introduction</b>	<b>1</b>
<b>2 Background on Infrared Radiation and Thermal Imaging</b>	<b>5</b>
2.1 A Brief Historical Account of the Discovery and Use of Infrared Radiation . . .	5
2.2 Sources of Infrared Radiation . . . . .	9
2.3 Transmission of Infrared Radiation . . . . .	13
2.4 Detection of Infrared Radiation . . . . .	15
2.4.1 Thermal Detectors . . . . .	15
2.4.2 Non-Thermal Detectors . . . . .	19
2.4.3 Some Important Focal Plane Array Detector Properties . . . . .	27

---

<b>3 Infrared Camera System Overview</b>	<b>29</b>
3.1 Infrared Camera System Constituents . . . . .	29
3.1.1 The Camera Head . . . . .	29
3.1.2 The Auxiliary Electronics Box . . . . .	31
3.1.3 Display Devices . . . . .	31
3.1.4 Cryo-Cooling Devices . . . . .	31
3.1.5 Temperature Measurements and Correction Criteria . . . . .	33
3.2 The Mercury Cadmium Telluride Infrared Camera . . . . .	34
3.2.1 Electrical Interface . . . . .	35
3.2.2 Optical Interface . . . . .	36
3.2.3 Thermal Interface . . . . .	38
<b>4 Noise Mechanisms in the Detection Process</b>	<b>39</b>
4.1 Temporal and Spatial Noise . . . . .	39
4.1.1 Temporal Noise . . . . .	40
4.1.2 Spatial Noise . . . . .	43
<b>5 Techniques of Nonuniformity Compensation</b>	<b>46</b>
5.1 Correction Schemes Using Temperature References . . . . .	48
5.1.1 Single-Point Compensation . . . . .	48
5.1.2 Two-Point Compensation . . . . .	49
5.1.3 Multi-Point Compensation . . . . .	51
5.2 Reference Free Correction Schemes . . . . .	53
5.2.1 The Reference-Free Compensation Scheme . . . . .	53
5.2.2 The Constant-Statistics Algorithm . . . . .	55
5.2.3 The Fading-Memory Polynomial Filter . . . . .	55
<b>6 Implementation of Reference Free Correction Schemes</b>	<b>61</b>
6.1 Infrared Camera Data Storage on Video Cassette . . . . .	61

6.2	Convergence Criteria . . . . .	62
6.3	Obtaining the Infrared Sequences . . . . .	63
6.4	Implementation of the Nonuniformity Correction Algorithms . . . . .	64
6.4.1	Reference-Free Nonuniformity Compensation Algorithm . . . . .	65
6.4.2	Constant-Statistics Algorithm . . . . .	67
6.4.3	Fading-Memory Polynomial Filters . . . . .	67
6.5	Dead Pixel Correction . . . . .	68
6.6	Varying the Portions of Standard Deviation Used . . . . .	70
6.7	Signal to Noise Ratio Determination . . . . .	71
6.7.1	Signal to Noise Ratio Determination from Image Averaging . . . . .	71
6.7.2	Validity of Signal to Noise Ratio Evaluation Using Time Averaged Output and Input Images . . . . .	75
<b>7</b>	<b>Results</b>	<b>81</b>
7.1	Results of Short Sequence Analysis . . . . .	83
7.1.1	Performance of the Reference-Free Compensation Algorithm . . . . .	85
7.1.2	Performance of the Constant-Statistics Compensation Algorithm . . . . .	85
7.1.3	Performance of the Fading-Memory Polynomial Filters . . . . .	85
7.2	Results of Long Sequence Analysis . . . . .	85
7.2.1	Performance of the Reference-Free Compensation Algorithm . . . . .	85
7.2.2	Performance of the Constant-Statistics Compensation Algorithm . . . . .	86
7.2.3	Performance of the Fading-Memory Polynomial Filters . . . . .	86
<b>8</b>	<b>Discussion</b>	<b>92</b>
8.1	Visible Differences between Original and Compensated Images . . . . .	92
8.2	Analytical Differences between Original and Compensated Images . . . . .	96
8.3	Contrast Enhancement . . . . .	98
8.4	Motion Dependence and Ghosting Artifacts . . . . .	101
8.5	Compensated Image Post-Processing . . . . .	101

<b>9</b>	<b>Conclusions and Recommendations</b>	<b>104</b>
9.1	Conclusions . . . . .	104
9.2	Recommendations . . . . .	105
<b>Bibliography</b>		<b>106</b>
<b>A</b>	<b>Graphical Results Obtained using the Reference-Free Compensation Algorithm</b>	<b>110</b>
<b>B</b>	<b>Graphical Results Obtained using the Constant-Statistics Algorithm</b>	<b>115</b>
<b>C</b>	<b>Graphical Results Obtained using the Fading-Memory Polynomial Filter with a Window Size of 20</b>	<b>120</b>
<b>D</b>	<b>Graphical Results Obtained using the Fading-Memory Polynomial Filter with a Window Size of 50</b>	<b>125</b>
<b>E</b>	<b>Graphical Results Obtained using the Fading-Memory Polynomial Filter with a Window Size of 100</b>	<b>130</b>
<b>F</b>	<b>Graphical Results Comparing the Peak Signal-to-Noise Ratios of the Output Image using Horizontal and Vertical Band Regions</b>	<b>135</b>
<b>G</b>	<b>True Input and Output Image PSNR compared to Time Averaged Input and Output Image PSNR</b>	<b>140</b>
<b>H</b>	<b>The CD-ROM</b>	<b>142</b>

# List of Figures

2.1	Location of Infrared in the Electro-Magnetic Spectrum [39] . . . . .	6
2.2	Typical Blackbody Cavity Radiators . . . . .	9
2.3	Variation of Energy per Interval of Wavelength with Wavelength [39] . . . . .	12
2.4	Atmospheric Transmission of Infrared Radiation over 1 mile [39] . . . . .	13
2.5	Atmospheric Transmission of Infrared Radiation over 2 km at Sea Level [32] .	14
2.6	Schematic Diagram of a Golay Cell Detector . . . . .	16
2.7	A Thermocouple Detector . . . . .	16
2.8	Bolometers in Bridged and Unbridged Configurations . . . . .	17
2.9	Spontaneous Electrical Polarisation versus Temperature for a Ferroelectric Material . . . . .	18
2.10	A Pyroelectric Detector . . . . .	19
2.11	Energy Diagram indicating Energy required by an Electron to move from Valence Band to Conduction Band . . . . .	20
2.12	Photo-conductor Bias Circuit . . . . .	21
2.13	Photo-diodes operated in Photo-conductive and Photo-voltaic modes . . . . .	22
2.14	Schematic Diagram of Photo-electric Cell . . . . .	23
2.15	Cutoff Wavelength as a Function of x Concentration for HgCdTe . . . . .	26
3.1	Infrared Camera System Assembly . . . . .	30
3.2	Electronic Circuit Diagram of the Input Stage . . . . .	35
3.3	Schematic Diagram illustrating the Dewar Vessel housing the Focal Plane Array	37
4.1	Schematic Diagram of the Noise Spectrum for a Photo-conductive Detector .	42

5.1	Output Voltages of Individual Detector Elements when a Single Flux Source is used . . . . .	49
5.2	Output Voltages of Individual Detector Elements when Two Different Sources of Incident Flux are used . . . . .	50
5.3	Individual Detector Element Offset and Responsivity . . . . .	51
5.4	3-Point Linear Interpolation Technique using 3 Different Flux Sources . . . . .	52
5.5	Simulated Analog Magnitude Response of the Fading-Memory Polynomial Filter	58
5.6	Simulated Analog Phase Response of the Fading-Memory Polynomial Filter (Normal Frequency) . . . . .	59
5.7	Simulated Analogue Phase Response of the Fading-Memory Polynomial Filter (Log Frequency) . . . . .	60
6.1	Constellation Diagram indicating the Location of Dead Pixels . . . . .	69
6.2	Streaking Artifacts in Time Averaged Output Image . . . . .	73
6.3	Horizontal and Vertical Band Regions . . . . .	73
6.4	Time Average and Standard Deviation of Pixels in the Uncorrupted Video Sequence . . . . .	76
6.5	Noise Fingerprints used as Fixed Pattern Noise . . . . .	77
6.6	Performance of the Reference-Free Compensation Algorithm . . . . .	79
6.7	True Input and True Output Image PSNR compared to Time Averaged Input and Output PSNR when Noise Fingerprint 1 is used . . . . .	80
7.1	Performance of the Reference-Free Compensation Algorithm over time . . . . .	82
7.2	Image Statistics obtained during the use of the Reference-Free Compensation Algorithm . . . . .	83
7.3	Input and Output Image PSNR for Long Night Sequence when the Reference-Free Compensation Algorithm is used . . . . .	84
8.1	Original Image compared to Output Image corrected using the Reference-Free Compensation scheme . . . . .	93
8.2	Output Image corrected using the Reference-Free Compensation scheme compared to Original Image . . . . .	94
8.3	Visible Performance of Various Compensation Algorithms on the Same Sequence	95

8.4	Indication of Contrast Enhancement in the Output Image by variation of P Value . . . . .	100
8.5	True Output Image compared to Output Image with Ghosting Artifacts . . .	102
A.1	Performance of Reference-Free Compensation Scheme on Short Day Sequence 1	110
A.2	Performance of Reference-Free Compensation Scheme on Short Day Sequence 2	111
A.3	Performance of Reference-Free Compensation Scheme on Short Day Sequence 3	111
A.4	Performance of Reference-Free Compensation Scheme on Short Day Sequence 4	112
A.5	Performance of Reference-Free Compensation Scheme on Short Night Sequence	112
A.6	Performance of Reference-Free Compensation Scheme on Long Day Sequence 1	113
A.7	Performance of Reference-Free Compensation Scheme on Long Day Sequence 2	113
A.8	Performance of Reference-Free Compensation Scheme on Long Night Sequence	114
B.1	Performance of Constant-Statistics Algorithm on Short Day Sequence 1 . . .	115
B.2	Performance of Constant-Statistics Algorithm on Short Day Sequence 2 . . .	116
B.3	Performance of Constant-Statistics Algorithm on Short Day Sequence 3 . . .	116
B.4	Performance of Constant-Statistics Algorithm on Short Day Sequence 4 . . .	117
B.5	Performance of Constant-Statistics Algorithm on Short Night Sequence . . .	117
B.6	Performance of Constant-Statistics Algorithm on Long Day Sequence 1 . . .	118
B.7	Performance of Constant-Statistics Algorithm on Long Day Sequence 2 . . .	118
B.8	Performance of Constant-Statistics Algorithm on Long Night Sequence . . . .	119
C.1	Performance of Fading-Memory Polynomial Filter (Window Size = 20) on Short Day Sequence 1 . . . . .	120
C.2	Performance of Fading-Memory Polynomial Filter (Window Size = 20) on Short Day Sequence 2 . . . . .	121
C.3	Performance of Fading-Memory Polynomial Filter (Window Size = 20) on Short Day Sequence 3 . . . . .	121
C.4	Performance of Fading-Memory Polynomial Filter (Window Size = 20) on Short Day Sequence 4 . . . . .	122
C.5	Performance of Fading-Memory Polynomial Filter (Window Size = 20) on Short Night Sequence . . . . .	122

---

C.6 Performance of Fading-Memory Polynomial Filter (Window Size = 20) on Long Day Sequence 1 . . . . .	123
C.7 Performance of Fading-Memory Polynomial Filter (Window Size = 20) on Long Day Sequence 2 . . . . .	123
C.8 Performance of Fading-Memory Polynomial Filter (Window Size = 20) on Long Night Sequence . . . . .	124
D.1 Performance of Fading-Memory Polynomial Filter (Window Size = 50) on Short Day Sequence 1 . . . . .	125
D.2 Performance of Fading-Memory Polynomial Filter (Window Size = 50) on Short Day Sequence 2 . . . . .	126
D.3 Performance of Fading-Memory Polynomial Filter (Window Size = 50) on Short Day Sequence 3 . . . . .	126
D.4 Performance of Fading-Memory Polynomial Filter (Window Size = 50) on Short Day Sequence 4 . . . . .	127
D.5 Performance of Fading-Memory Polynomial Filter (Window Size = 50) on Short Night Sequence . . . . .	127
D.6 Performance of Fading-Memory Polynomial Filter (Window Size = 50) on Long Day Sequence 1 . . . . .	128
D.7 Performance of Fading-Memory Polynomial Filter (Window Size = 50) on Long Day Sequence 2 . . . . .	128
D.8 Performance of Fading-Memory Polynomial Filter (Window Size = 50) on Long Night Sequence . . . . .	129
E.1 Performance of Fading-Memory Polynomial Filter (Window Size = 100) on Short Day Sequence 1 . . . . .	130
E.2 Performance of Fading-Memory Polynomial Filter (Window Size = 100) on Short Day Sequence 2 . . . . .	131
E.3 Performance of Fading-Memory Polynomial Filter (Window Size = 100) on Short Day Sequence 3 . . . . .	131
E.4 Performance of Fading-Memory Polynomial Filter (Window Size = 100) on Short Day Sequence 4 . . . . .	132
E.5 Performance of Fading-Memory Polynomial Filter (Window Size = 100) on Short Night Sequence . . . . .	132
E.6 Performance of Fading-Memory Polynomial Filter (Window Size = 100) on Long Day Sequence 1 . . . . .	133

---

E.7	Performance of Fading-Memory Polynomial Filter (Window Size = 100) on Long Day Sequence 2 . . . . .	133
E.8	Performance of Fading-Memory Polynomial Filter (Window Size = 100) on Long Night Sequence . . . . .	134
F.1	PSNR of Output Image obtained using the Total Image as well as Horizontal and Vertical Band Regions for Short Day Sequence 1 . . . . .	135
F.2	PSNR of Output Image obtained using the Total Image as well as Horizontal and Vertical Band Regions for Short Day Sequence 2 . . . . .	136
F.3	PSNR of Output Image obtained using the Total Image as well as Horizontal and Vertical Band Regions for Short Day Sequence 3 . . . . .	136
F.4	PSNR of Output Image obtained using the Total Image as well as Horizontal and Vertical Band Regions for Short Day Sequence 4 . . . . .	137
F.5	PSNR of Output Image obtained using the Total Image as well as Horizontal and Vertical Band Regions for Short Night Sequence . . . . .	137
F.6	PSNR of Output Image obtained using the Total Image as well as Horizontal and Vertical Band Regions for Long Day Sequence 1 . . . . .	138
F.7	PSNR of Output Image obtained using the Total Image as well as Horizontal and Vertical Band Regions for Long Day Sequence 2 . . . . .	138
F.8	PSNR of Output Image obtained using the Total Image as well as Horizontal and Vertical Band Regions for Long Night Sequence . . . . .	139
G.1	True Input and True Output Image PSNR compared to Time Averaged Input and Output PSNR when Noise Fingerprint 1 is used . . . . .	140
G.2	True Input and True Output Image PSNR compared to Time Averaged Input and Output PSNR when Noise Fingerprint 2 is used . . . . .	141

# List of Tables

6.1	Standard Deviations of Pixels in Infrared Sequences . . . . .	70
6.2	Peak Signal to Noise Ratio of Output Image Sequences Using Total Output Image and Band Regions . . . . .	74
6.3	True PSNR Improvement compared to PSNR improvement obtained by Time Averaging Input and Output Images . . . . .	78
7.1	PSNR Improvement in the Short Sequences using the Reference-Free Compensation Algorithm . . . . .	87
7.2	PSNR Improvement in the Short Sequences using the Constant-Statistics Compensation Algorithm . . . . .	87
7.3	PSNR Improvement in the Short Sequences using the Fading-Memory Polynomial Filter with Window Size 20 . . . . .	88
7.4	PSNR Improvement in the Short Sequences using the Fading-Memory Polynomial Filter with Window Size 50 . . . . .	88
7.5	PSNR Improvement in the Short Sequences using the Fading-Memory Polynomial Filter with Window Size 100 . . . . .	89
7.6	PSNR Improvement in the Long Sequences using the Reference-Free Compensation Algorithm . . . . .	89
7.7	PSNR Improvement in the Long Sequences using the Constant-Statistics Compensation Algorithm . . . . .	90
7.8	PSNR Improvement in the Long Sequences using the Fading-Memory Polynomial Filter with Window Size 20 . . . . .	90
7.9	PSNR Improvement in the Long Sequences using the Fading-Memory Polynomial Filter with Window Size 50 . . . . .	91
7.10	PSNR Improvement in the Long Sequences using the Fading-Memory Polynomial Filter with Window Size 100 . . . . .	91

8.1 Overall PSNR Improvement in the Short Sequences . . . . .	96
8.2 Overall PSNR Improvement in the Long Sequences . . . . .	97

# Glossary

<b>1D</b>	One-dimensional
<b>2D</b>	Two-dimensional
<b>3D</b>	Three-dimensional
<b>ADC</b>	analog-to-digital converter
<b>CCD</b>	charge-coupled-device
<b>CMOS</b>	complementary metal-oxide semiconductor
<b>DAC</b>	digital-to-analog converter
<b>EM</b>	electro-magnetic
<b>FLIR</b>	foward-looking infrared
<b>FPA</b>	focal plane array
<b>FPDA</b>	focal plane detector array
<b>HgCdTe</b>	mercury cadmium telluride
<b>IR</b>	infrared
<b>IRCMOS</b>	infrared complementary metal-oxide semiconductor
<b>IRFPA</b>	infrared focal plane array
<b>IR-ST</b>	infrared search and track
<b>LWIR</b>	long-wavelength infrared
<b>MOS</b>	metal-oxide semiconductor
<b>MWIR</b>	medium-wavelength infrared
<b>PSNR</b>	Peak Signal-to-Noise ratio
<b>SNR</b>	Signal-to-Noise ratio
<b>SWIR</b>	short-wavelength infrared

# List of Symbols

- $c$  speed of light in a vacuum =  $2.99792458 \times 10^8 \text{m.s}^{-1}$   
 $e$  2.718281828  
 $h$  Planck's constant =  $6.6260755 \times 10^{-34} \text{J.s}$   
 $k$  Boltzmann's constant =  $1.380658 \times 10^{-23} \text{J.K}^{-1}$   
 $q$  charge of an electron =  $1.60217733 \times 10^{-19} \text{C}$   
 $\pi$  3.141529654  
 $\sigma$  Stefan's constant =  $5.67 \times 10^{-8} \text{W.m}^{-2} \text{K}^{-4}$

# Chapter 1

## Introduction

*It is an interesting exercise to consider how different our picture of the world would be if one or the other of our special senses had never been created. Without an organ of vision, for example, there would be no astronomy, very little chemistry, biology and geology, and only a small fraction of physics left to us. All the visual arts would go - or at least the two dimensional ones. We are each rather like a prisoner in a round tower permitted to look out through five slits in the walls at the landscape outside. It is presumptuous to suppose that we can perceive the whole of the landscape through these slits.*

**Raynor C. Johnson in *The Imprisoned Splendour***

As miraculous as are the achievements of Life in the evolution of organisms, perhaps nothing is more impressive than the intricacy, accuracy and ingenuity in the construction of the human eye. The development of such a small, specialised organ as this only serves to emphasise the evidence of its purpose. The human eye is a remarkable organ that has biologically adapted to sense blue to red light, only a small portion of the electro-magnetic spectrum but a portion wherein the greater part of our knowledge of the external world has been derived.

The perception of colour and form in our environment occurs primarily due to the reflection of visible light, emanating from various sources, off objects and their surroundings. Sometimes objects become hot enough to glow at visible colours. Most objects, however, are at room temperature and are thus too cold to glow visibly making them invisible at night where there is an absence of light. But their finite temperature does allow them to glow in the infrared region of the spectrum. It is this glow (or its reflection of other objects and surfaces) that infrared thermal imaging devices strive to see.

Practical infrared thermal imaging has evolved to become a key technology with devices

being used successfully by civilian, military and paramilitary organisations. The field of thermal imaging has also seen unprecedented growth over the past 30 years due to the many superior properties that the infrared spectrum presents over the visible spectrum. Infrared radiation is able to penetrate cloud and mist much better than visible light and is also able to be detected at night. Thermal imaging devices have found uses in areas such as security and surveillance, navigation and flight control, as well as medical science and astronomy. Environmental assessment, including pollution level monitoring, relative humidity profiles and the distribution of different gases in the atmosphere, is also a new developing market for infrared thermal imaging technology. Night vision devices are used extensively by military and law enforcement organisations as they allow officers to conduct covert surveillance at night, and approach suspect sites without bright lights [15].

The demand for better devices to suit increasing markets, particularly the military, has increased the need for better thermal imaging detectivity. In military environments adverse operating conditions influence the detectivity of thermal devices, hence the stable performance of such devices are required. Mercury cadmium telluride (HgCdTe) focal plane arrays are currently used in such thermal imaging applications. Reasons that have favoured this choice of detector material include good detectivity over the wavelength range of interest as well as the relatively high temperatures that this material is able to operate at.

However, the sensitivity of focal plane arrays fabricated from HgCdTe are limited by nonuniformities that exist in the material itself. These nonuniformities are due to the experimental nature of the HgCdTe material doping techniques and fabrication processes. The presence of such nonuniformities lead to spatial noise mechanisms in the detector array. Focal plane arrays created from HgCdTe exhibit spatial variations in dark signal and photo-response. Individual detectors in the array also exhibit differences in spectral response. Thus, as a direct result of these nonuniform responses, the uncompensated imagery of HgCdTe infrared cameras usually exhibit embedded fixed pattern noise.

Adequate compensation for the effects of fixed pattern noise and artifacts of array nonuniformity is a particularly important problem for detectors operating in the infrared region of the spectrum. Infrared scenes are inherently of low contrast, so pertinent detail can be easily masked by pattern noise. The presence of fixed pattern spatial noise in uncompensated infrared imagery obscures low contrast detail in the scene under view and limits camera sensitivity. In order to address the problems associated with spatial noise mechanisms in HgCdTe focal plane arrays noise compensation techniques are required.

Previous methods of nonuniformity correction in infrared detectors arrays have involved schemes where the sensor is calibrated by presenting uniform temperature sources of constant intensity over the sensor's field of view. If the individual detector elements are perfectly

linear (within the calibration range) and stable in time, then a once performed ‘factory’ temperature calibration would allow for the correction of pixel nonuniformities. However,  $1/f$  noise [34], nonuniform cooling of the sensor array within the dewar housing, and system instabilities (due to varying operating conditions) increase the overall system noise and create the need for frequent recalibration. In current infrared camera systems, this is normally achieved by repeatedly inserting uniform temperature sources into the optical field of view. These cameras require complex electro-optical/electro-mechanical shutter assemblies which lead to greater system design overhead. An elegant, yet efficient, approach would be to perform the calibration in real time based on the statistics of the radiant photon flux from the scene being viewed.

The aim of this thesis was to investigate the implementation of such scene-based corrective techniques and to determine if they offer adequate methods of calibration in compensating for the effects of fixed pattern noise in a HgCdTe infrared camera. As the implemented techniques use scene statistics in performing the nonuniformity compensation, they all dispense with the traditional need for temperature references. In these methods the statistics of the moving infrared scene as well as motion of the detector assembly are used in the calibration procedure. The motion of the infrared detector array includes panning of the camera in horizontal and vertical directions. The time averaging of frames is implemented, as it is assumed that all the detector pixels will eventually be irradiated with the same levels of flux after some extended period of time. Using the continuous time average of the data, the correction coefficients may be re-calculated and updated.

These scene-based techniques were also created to ensure that the calculated coefficients continuously track variations in the dark currents as well as temperature changes within the dewar sensor cooling vessel associated with a HgCdTe infrared camera. This camera operates in the  $3 - 5\mu\text{m}$  portion of the infrared spectrum and requires cooling with liquid nitrogen to perform effectively. The above changes may be a result of varying environmental and operational conditions. A comparison of the various scene-based methods implemented as well as a determination of their overall levels of success in compensating for the effects of fixed pattern spatial noise is presented in this dissertation.

The **layout of the thesis** is as follows

- Chapter 2 contains a brief introduction to the science of infrared thermal imaging. Infrared sources and detectors as well as aspects affecting the transmission of infrared radiation in the atmosphere are described.
- Chapter 3 presents general system overviews of current infrared cameras. A detailed system overview of the HgCdTe camera used for the duration of this project is also

given.

- Chapter 4 describes the noise mechanisms present in the camera system. Both temporal and spatial noise mechanisms are discussed and their respective differences established.
- Chapter 5 highlights previous techniques of nonuniformity compensation as applied to focal plane arrays. Correction schemes using temperature references and reference free correction schemes are described.
- Chapter 6 provides a detailed account of the implementation of reference free correction techniques in compensating for the effects of fixed pattern noise.
- Chapter 7 documents both visual and analytical results obtained by the implementation of the reference free correction algorithms.
- Chapter 8 discusses the improvements in overall image quality in terms of fixed pattern noise compensation when reference free corrective techniques are used. These improvements are examined from both a visual and an analytical point of view.
- Chapter 9 concludes this report, yielding the major findings and several recommendations.
- Appendices A, B, C, D, E, F and G provide graphical results obtained during the implementation of reference free corrective techniques on various sequences.

A CD-ROM (Appendix H) has also been included with this thesis. It contains the source code for the implemented reference free corrective techniques. An original infrared sequence and compensated sequence using the Reference-Free Compensation scheme with  $P = 0.5$  are also included on the CD.

## Chapter 2

# Background on Infrared Radiation and Thermal Imaging

*Any person who has enjoyed the warmth of the sun must have had some concept of the nature of infrared radiation.*

*Ivan Simon in *Infrared Radiation**

### 2.1 A Brief Historical Account of the Discovery and Use of Infrared Radiation

Sir William Herschel is credited with the discovery of infrared (IR) radiation whilst engaged with the study of solar spectroscopy during the earlier part of the 19th century [32]. Herschel was looking for a substance that would stop solar radiation from heating the lenses of a telescope. Although he did not find the material he was looking for he did discover the cause of the effect. The *Philosophical Transactions* of 1800 contain an account of an experiment he carried out: he produced a solar spectrum with the aid of a prism and, on exploring this visible spectrum with a mercury thermometer, he found a considerable increase of temperature just past the red end of the spectrum [35]. Herschel himself became convinced that he discovered a new type of radiation. It was not clear at the time that heat rays and light rays were of the same kind. The question of the similarity of the infrared and visible radiation, with regards to propagation, reflection and absorption, was not raised until 1835, by Ampère. In 1834 J. D. Forbes showed that heat radiation can be polarised in the same manner as light. It was only after A. H. L. Fizeau and J. B. L. Foucault actually determined the wavelength of near infrared waves from interference fringes (in 1837) that the identity of infrared with visible

## 2.1. A BRIEF HISTORICAL ACCOUNT OF THE DISCOVERY AND USE OF INFRARED RADIATION

light became generally accepted. The electro-magnetic (EM) nature of infrared radiation was experimentally verified by E. F. Nichols and J. D. Tear in 1924. They succeeded in generating far-infrared waves of  $220\mu\text{m}$  by means of a miniature spark oscillator, thus showing beyond any doubt that infrared radiation is also a part of the electro-magnetic spectrum [32].

Infrared radiation comprises of the thermal radiation that is released from bodies when they are heated to certain temperatures. It also has the strongest heating effect of all types of radiation. All radiation can be absorbed and degraded to heat. Infrared is, however, the most common radiation, found in abundance everywhere, coming from all sources, even from comparatively cool objects. Mankind has come to realise that heating effects of his own sun, which heats and lights the earth over the vast expanse of interstellar space, is essential to all life.

The essential property that distinguishes infrared radiation from light is its position in the electro-magnetic spectrum. The infrared spectrum extends from  $0.75\mu\text{m}$ , which lies just after the deep red, to  $1000\mu\text{m}$ , which lies before the microwave band.

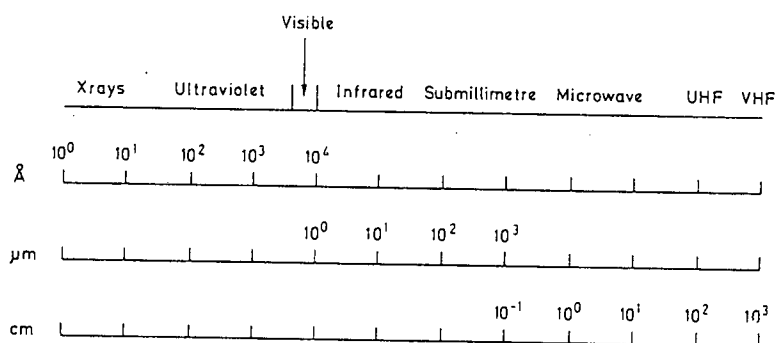


Figure 2.1: Location of Infrared in the Electro-Magnetic Spectrum [39]

This infrared spectrum has been further divided into three sub-regions. These comprise of the the near infrared ( $0.75 - 3\mu\text{m}$ ), middle infrared ( $3 - 12\mu\text{m}$ ) and the far infrared ( $12 - 1000\mu\text{m}$ ).

Due to ongoing advances in the fields of optics and electronics, infrared detection, measurement and imaging continue to find increasingly numerous and varied uses in industry, the military and medicine. The exploration of the infrared spectrum has rapidly advanced in the twentieth century as new applications have presented themselves and new materials have been developed to meet these challenges. The science of infrared detection has become a specialised art. Breakthrough concepts and techniques have also been discovered due the greater emphasis being placed on research and technological development.

## 2.1. A BRIEF HISTORICAL ACCOUNT OF THE DISCOVERY AND USE OF INFRARED RADIATION

---

Over the past half century infrared radiation has been exploited in primarily four areas [39]

1. Analysis and Characterisation of Materials
2. Thermal Imaging
3. Communication Techniques
4. Astronomy

Infrared spectroscopy and related techniques have been developed to analyse and characterise materials. It is found that certain organic molecules resonate at well defined frequencies. When under investigation, certain atomic groupings in solution manifest these resonances by the strong absorption of particular wavelengths of light. Various organic materials may be characterised by these absorption lines as they are precise and well documented. This has allowed infrared spectroscopy to become a powerful tool in organic analysis [32, 39].

Thermal imaging is governed by the established principle that any material or object at a non-zero temperature (in Kelvin) emits electro-magnetic radiation. The emitted electro-magnetic radiation has a wavelength distribution that is characteristic of the absolute temperature of the object as well as its surface emissivity. Terrestrial objects having temperatures in the neighbourhood of 300 K radiate most strongly at about  $10\mu\text{m}$  which lies in the infrared portion of the electro-magnetic spectrum. Variations in temperature over the surface of the object (or reflections of this electro-magnetic radiation from other objects) will, provided the emissivity is constant, form what is known as a thermal image (analogous to an optical image formed by reflected visible radiation). This information may then be used to produce an optical image which reproduces the temperature intensity pattern.

The importance of infrared as vehicle of information by 'invisible rays' was recognised in the earlier part of the twentieth century. Before the end of World War I, infrared signalling and detecting systems using newly discovered photo-conductive cells had been put into field service. During World War II the research effort was greater and substantial progress in infrared technology was made [32]. Fibre-optic communication systems, which form the backbone of latter twentieth century telecommunication and data networks, rely upon infrared photo-diodes and photo-detectors. In these fibre-optic networks infrared signalling has been selected due to several reasons. Some of these include the invisible nature of infrared light, leading to greater security, and enhanced materials constraints placed by the optical fibre waveguides in terms of the low attenuation of infrared signals during transmission.

The three spectral regions which have been used in the study of astronomy include the visible, infrared and radio frequency regions. Electro-magnetic radiation other than that falling

## 2.1. A BRIEF HISTORICAL ACCOUNT OF THE DISCOVERY AND USE OF INFRARED RADIATION

---

into one of these groups is usually strongly absorbed by the earth's atmosphere. Infrared astronomy is used for observation through interstellar dust where the extinction of light from the centre of galaxy is dimmed about one trillion times in the visible but only 16 times in the infrared. Infrared methods are also used for observations in certain absorption bands and, more recently, for dust and cold gas studies [15].

However, with the dawn of the new millennium rapidly advancing many new challenges requiring competent solutions are becoming known. Some of these include problems in diverse fields like environmental monitoring, medicine and extra-planetary or space sensing. Environmental monitoring is, at present, a growing market for infrared products. Infrared systems can be used to monitor gas effluents, smokestack emissions, and the thermal pollution of water and air resources [15]. Thermal imaging is used in medicine for the public screening of diseases like breast and testicular cancer. Thermal imaging has also been applied to monitor blood flow patterns in the cerebral cortex of infants [17]. Spectral studies of chemical and astrophysical processes, as well as studies of planetary atmospheres, are also areas where infrared detection is finding increasing use. Mass estimates of comets and asteroids are performed through thermal inertia calculations based on their change in temperature often requiring the use of complex infrared detection techniques[15].

Due to the success of infrared equipment in Operation Desert Storm during the Gulf War, military organisations worldwide are looking to the infrared to provide them with superior targeting and tracking capabilities during clandestine night operations. Night vision systems offer military personnel covert surveillance abilities. A primary military growth area for infrared utilisation is in radar stealth platforms. Infrared search and track systems (IR-ST) are finding increasing uses in the effective detection of stealth planes and ships. Stealth planes may also be equipped with IR-ST systems as general radar may give away the plane's position.

As a result of the rapid growth the electronics market has experienced over the last 25 years, future uses of infrared technology would be complemented by faster computing and better materials. Advanced systems requiring excessive space requirements would also become smaller and more robust as the physical size is leveraged with lightweight, user friendly components. In the case of thermal imaging, image processing will allow the user more processing power allowing infrared systems to become more user-orientated and friendly. Information would take precedence over raw imagery. The technology would become transparent to it's users, who will get the information they desire, instead of being left to interpret fuzzy images by themselves. Large scale distributed image processing and pattern recognition techniques will allow a system to identify and monitor the position of an enemy vehicle or the type of blight infecting a forest. Due to the ongoing research and development thermal imaging systems of today are no longer the simple infrared viewers of the past. They are quickly evolving, taking advantage of new technology, combining visible, radar and infrared images in manners

that offer the user the maximum information content in a single image. Infrared thermal imaging systems of the future will be more reliable and robust. They will also be tailored to specifically solve the needs of the problem at hand rather than suit the problem to an existing solution.

## 2.2 Sources of Infrared Radiation

Infrared radiation is essentially a form of electro-magnetic radiation with a spectrum that extends from  $0.75\mu\text{m}$ , which lies just after the deep red, to  $1000\mu\text{m}$ , which appears before the microwave band [35]. Electro-magnetic radiation is emitted by any object at any temperature above absolute zero (0 K), but the amount emitted and its distribution with wavelength depends on the temperature and emissivity of the body. While the unity of different kinds of radiation in the electro-magnetic spectrum is recognised, the basic laws of infrared radiation refer to its thermal origin. In particular, these laws are concerned with the thermal radiation emitted from various objects heated to a certain predefined temperature. Such radiation covers a broad continuum of wavelengths. Various objects emit or absorb, more or less, depending on how 'bright' or 'dark' their surface colouration appears to be [35].

In order to eliminate this source of arbitrariness from theoretical considerations, physicists after Kirchoff postulated a *blackbody* as the most effective radiator and complete absorber at all wavelengths. Although no single known substance exhibits this ideal property when examined over a wide spectral range, it is found that radiative characteristics of an aperture in an isothermal cavity made of an opaque, absorbing material represents almost exactly the property of a blackbody. The process of producing the blackbody effect is the multiple traversal of the rays emitted by the walls and reflected from them in a diffuse manner before they reach the aperture and escape into the outer world [32].

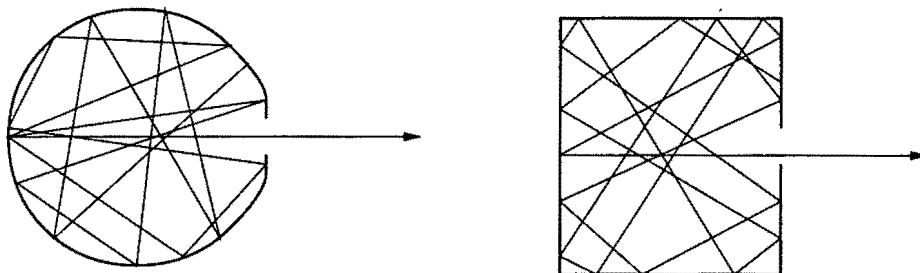


Figure 2.2: Typical Blackbody Cavity Radiators

By this process of multiple emission, absorption, reflection and re-emission, the radiation present in the cavity comes into thermal equilibrium with the walls. The radiation inside the

cavity has the same intensity everywhere, with traversal in all possible directions in equal strengths. It is thus homogeneous and isotropic. The intensity of the blackbody radiation is a function of temperature only, no matter the kind of material of which the cavity is made. It is also found that the blackbody radiation emerging from the aperture obeys *Lambert's Law*, that is, its intensity is greatest in a direction perpendicular to the plane of the aperture and decreases with the cosine of the angle between the normal and the direction of observation [35]. Radiation from real bodies seldom approach this simple law.

Radiant emittance is defined as the radiant energy emitted per second per  $m^2$  of surface area. Energy per second is power; hence emittance may be measured in units of watts per  $m^2$ . Temperature  $T$  is measured in degrees Kelvin. The variation of emitted energy with direction is defined as radiance, and is the power emitted per  $m^2$  per unit solid angle (steradian).

The emittance  $W$  of any real object is less than that of the emittance of a blackbody  $W_b$ . The ratio  $W/W_b$  is called the *emissivity*,  $\epsilon$ . It follows then by definition, that for a blackbody,  $\epsilon = 1$ . We may also define the ratio of radiant power absorbed by an object to the incident power as *absorptance*  $\alpha$ . For a blackbody,  $\alpha = 1$ , and hence  $\alpha_b = \epsilon_b$ . It can be shown that, even in non-blackbodies, as long as they are opaque,  $\alpha = \epsilon$  [13]. This leads to *Kirchoff's Law* which states

$$W = \epsilon W_b = \alpha W_b \tag{2.1}$$

As all radiometric quantities depend on wavelength, *spectral emittance*  $W_\lambda$  is defined as the amount of radiant power emitted by a unit area in a wavelength interval from  $\lambda$  to  $d\lambda$ . It is found that *Kirchoff's Law* also applies to the spectral emittances of opaque objects.

$$W = \epsilon_\lambda W_{\lambda b} = \alpha_\lambda W_{\lambda b} \tag{2.2}$$

or

$$\frac{\alpha_\lambda}{\epsilon_\lambda} = 1 \tag{2.3}$$

In this form *Kirchoff's Law* may be said to state that at any given temperature a body absorbs most strongly radiation of that wavelength which it emits [32].

The properties of a blackbody radiator may be calculated theoretically [13]. Three points about it are of primary importance.

1. For the blackbody the total emissive power or radiant emittance is exactly proportional to the fourth power of its absolute temperature. This follows the *Stefan-Boltzmann Law* given by

$$W_{total} = \sigma T^4 \quad (2.4)$$

where  $\sigma$  is Stefan's constant, and is approximately equal to  $= 5.67 \times 10^{-8} \text{W.m}^{-2}\text{K}^{-4}$ . The word total in this context refers to the to the entire wavelength spectrum from  $\lambda = 0$  to infinity.

2. The curve of the variation of radiant emittance per interval of wavelength is always the same shape. This characteristic follows *Planck's Law*, which describes the spectral dependence of the radiative properties of a blackbody on temperature. The amount of radiant energy per unit volume of blackbody cavity per unit frequency interval is designated as the spectral energy density  $u_\nu$ . This law in its simplest form expresses the spectral energy density  $u_\nu$  as a function of temperature  $T$  and frequency  $\nu$  by the following formula (valid for unpolarised radiation)

$$u_\nu = \frac{8\pi h\nu^3}{c^3(E^{h\nu/kT} - 1)} \quad (2.5)$$

Planck's formula may also be expressed in a form that applies to the more practical situation when the blackbody radiation is allowed to escape from the isothermal cavity through a small aperture. The rate of flow of radiant energy per unit area of the aperture in wavelength interval  $d\lambda$ , or spectral emittance, is then

$$W_{\lambda b}d\lambda = \frac{2\pi hc^2 d\lambda}{\lambda^5(E^{hc/\lambda kT} - 1)} \quad (2.6)$$

Equation 2.6 is obtained from Eq. 2.5 due to  $\nu = c/\lambda, u_\nu d\nu = u_\lambda d\lambda$  and knowing that  $W_\lambda = 1/4cu_\lambda$ . The latter relationship is obtained by integrating the energy flux in the forward direction over the hemispherical solid angle.

3. When *Planck's Law* is plotted graphically for various temperatures, one obtains a family of curves shown in Fig. 2.3. If a particular curve (isotherm) is followed, it is seen that the spectral emittance is zero at  $\lambda = 0$ , proceeding through a maximum at a particular wavelength  $\lambda_{max}$  and, after passing this maximum, approaches zero at very long wavelengths. The higher the temperature the shorter the wavelength at which the maximum occurs. This temperature-wavelength relationship is given by *Wien's Displacement Law* and it is obtained by taking the derivative of *Planck's Law* with respect to  $\lambda$  and finding the maximum [32]. *Wiens Displacement Law*, given by

$$\lambda_{max} = \frac{2.898 \times 10^{-3} \text{m.K}}{T} \quad (2.7)$$

where  $\lambda_{max}$  is in meters and  $T$  is in Kelvin, expresses mathematically the common observation that thermal radiators glow at a dull red colour when heated to relatively low temperatures (approximately 1000 K), but then appear more orange or yellow as their temperatures are raised. Very hot stars (e.g. Sirius, 11 000 K) emit bluish-white light. At lower earth-based temperatures, the peak of Planck's curve is in the infrared. At ambient temperature (about 300 K),  $\lambda_{max} = 9.7\mu\text{m}$ . Terrestrial objects at or slightly above room temperature (295 to 360 K) radiate most strongly in the 8 – 10 $\mu\text{m}$  band.

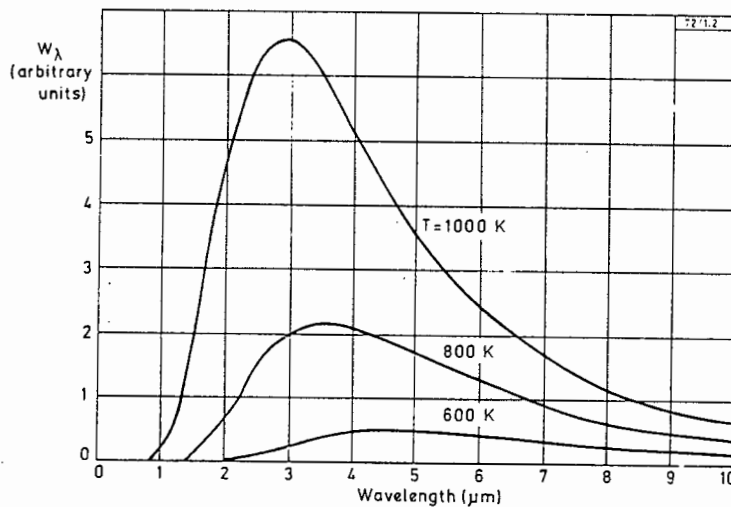


Figure 2.3: Variation of Energy per Interval of Wavelength with Wavelength [39]

The total emittance may be obtained by integrating the spectral emittance from  $\lambda = 0$  to infinity. This is given by

$$W_b = \int_0^{\infty} W_{\lambda b} d\lambda = \sigma T^4 \quad (2.8)$$

which is the *Stefan-Boltzmann Law* mentioned above.

Real objects and materials almost never comply with these laws over an extended wavelength interval, although they may approach the blackbody behaviour in certain spectral regions. There are two principal reasons for this. Firstly, real bodies transmit some of the radiation and secondly, they reflect some of it. Transmission, the first effect, occurs only in bodies

that have a finite thickness, in particular if their intrinsic absorption is slight. The second effect, reflection, is most conspicuous with metals, but it is also present to some extent in all materials as long as they possess well defined surface boundaries [32].

## 2.3 Transmission of Infrared Radiation

Despite the similarities between infrared and visible light, it is important to realise that, because an object may be transparent or opaque in the visible region of the spectrum, it is not necessarily so in the infrared. Thus, as an example, ordinary clear glass (crown glass) is transparent to only about  $2.5\mu\text{m}$  and flint (lead) glass may transmit to as far as  $4.5\mu\text{m}$  [32]. On the other hand, semiconductor materials such as germanium and silicon, opaque in the visible region, are transparent in the infrared region of the spectrum beyond  $1.8$  and  $1.0\mu\text{m}$  respectively [36].

An important factor in the transmission of infrared over long distances is the set of restrictions that the atmosphere presents. The atmosphere is far from being a pure substance; it is a mixture of nitrogen, oxygen and the rare gases. It also contains variable amounts of water (in gaseous, liquid and solid form), carbon dioxide and suspended particles (smog, dust). Radiation passing through such a turbid medium is partly absorbed and scattered. Solar radiation illuminating this medium is scattered and some of it reaches an infrared detector together with the source radiation and thermally excited atmospheric radiation. Thus the radiation from a source is attenuated with unwanted 'background' radiation superimposed on it. A typical atmospheric transmission curve as the wavelength is varied is shown in Fig. 2.4 [39].

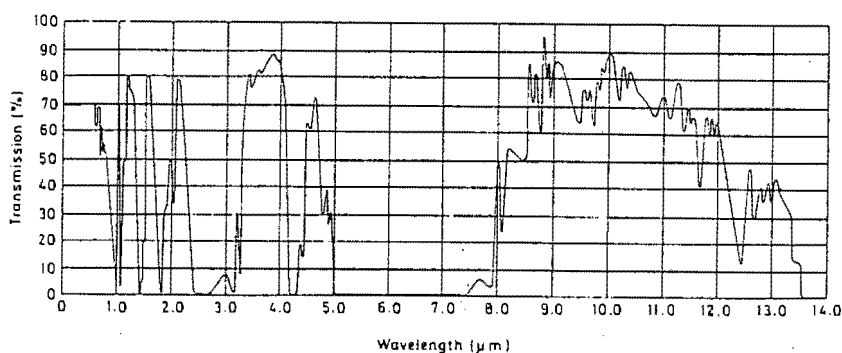


Figure 2.4: Atmospheric Transmission of Infrared Radiation over 1 mile [39]

There are six regions wherein the transmission is almost completely blocked by the  $H_2O$  and  $CO_2$  bands, and eight 'windows' in which the absorption is very slight. Figure 2.5 highlights these blocked regions and transmission windows [32]. In a camera system the choice of a particular window is determined by the temperature of the source (which determines  $\lambda_{max}$  of its emission curve) and by the spectral sensitivity of the detector. The two windows extending from 2.9 to 4.3  $\mu m$  and 7.5 to 14  $\mu m$  are particularly useful.

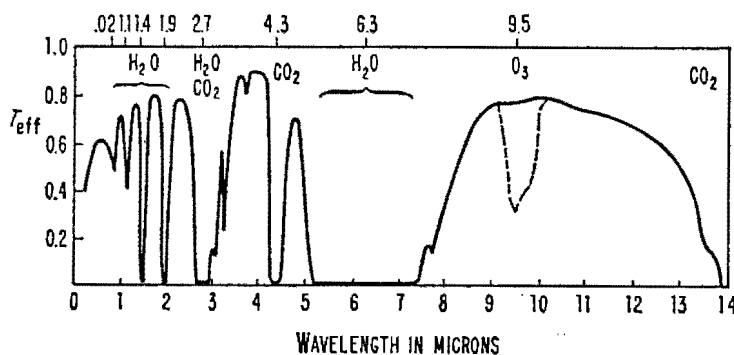


Figure 2.5: Atmospheric Transmission of Infrared Radiation over 2 km at Sea Level [32]

The actual transmittance in any of the windows depends primarily on the amount of water in the optical path [32, 39]. For any given concentration of water vapour, the dependence of transmittance on path length  $x$  obeys very nearly the exponential law

$$T_t = e^{-\alpha x} \quad (2.9)$$

The attenuation resulting from scattering by particles suspended in the atmosphere may be similarly expressed by the exponential law

$$T_s = e^{-\beta x} \quad (2.10)$$

wherein the exponent  $\beta$  is a function of wavelength ( $\lambda$ ), the concentration of particles and their diameter ( $a$ ), as well as the refractive index and absorption coefficient  $\alpha$  of the atmosphere. As far as wavelength dependence is concerned, three cases can be distinguished:

1.  $a \ll \lambda$  (Rayleigh Scattering),  $\beta \propto \lambda^{-4}$
2.  $a \simeq \lambda$  (Mie Scattering),  $\beta$  is a complex function of  $\lambda$

3.  $a \gg \lambda$  (Non-selective Scattering),  $\beta$  is independent of  $\lambda$

*Rayleigh scattering* is characterised by the inverse-fourth-power dependence on wavelength [32]. For a given particle size, transmittance is much greater for longer wavelengths than for short ones. *Mie scattering* varies greatly with wavelength as the wavelength becomes comparable to the particle size [39]. In the cases of *non-selective scattering*, the exponent  $\beta$  turns out to be nearly independent of wavelength. This is practically the most important case because water droplets in clouds and fog have sizes in the range between 5 to 100 $\mu\text{m}$ , and are thus much greater than waves in the near infrared. The fact that  $\beta$  is independent of  $\lambda$  means that scattering in fog is just as bad in the infrared as it is in the visible [15]. When attenuation is due to both absorption and scattering, the effective transmittance may be expressed by the product

$$T_{eff} = T_t \cdot T_s = e^{-(\alpha+\beta)x} \quad (2.11)$$

In haze or fog, attenuation by scattering is the dominant factor. Slant paths and vertical paths offer a better transmission than straight or horizontal paths. The conditions also improve rapidly with altitude as the humidity and haziness of the atmosphere disappear [15].

## 2.4 Detection of Infrared Radiation

Detection of infrared radiation has been achieved by both thermal and non-thermal (photon) detectors. When the radiation incident upon a thermal receiver is absorbed, its temperature rises. These heating effects of radiation have led to the inventions of thermal detectors and thermocouples. The discovery of the photo-electric effect in the earlier part of the twentieth century has ushered in a variety of semi-conductive detectors that depend upon the quantum nature of electro-magnetic energy. These detectors no longer depend on the natural heating effects of the incident radiation but rather upon the frequencies contained therein.

### 2.4.1 Thermal Detectors

In thermal detectors, temperature changes and fluctuations are measured by material properties which depend on temperature. There are four primary types of thermal detectors in use: pneumatic cells, thermocouples, bolometers and pyroelectric detectors.

**Pneumatic Detectors:** Pneumatic detectors make use of the large thermal expansivity of gas as the temperature-selective material property. In a Golay cell, the heating of a film

incident to the radiation results in an expansion of the gas in the cell. This expansion in the gas is transmitted to a flexible membrane at the rear of the device. The flexible membrane, maintained taut under tension, is reflective due to a metallic coating. The movement of the membrane caused by the expansion of the gas leads to the change in illumination of a subsidiary photo-cell. An optical assembly is used whereby the curvature of this membrane is detected by means of an interferometric method [see pages 30-31 of [32] for more information].

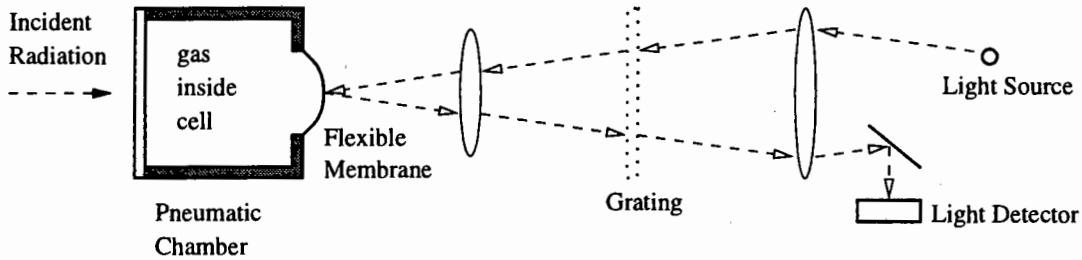


Figure 2.6: Schematic Diagram of a Golay Cell Detector

**Thermocouples:** Thermocouples use the temperature difference between the junctions of two different metals as the detection mechanism [32, 38]. This difference in the junction temperature gives rise to a small voltage which is proportional to the incident temperature. For small temperature differences  $\Delta T$  between the hot and cold junction, the thermoelectric voltage is found to be proportional to  $\Delta T$ ,

$$V = s\Delta T \tag{2.12}$$

where  $s$  bears the historical but somewhat misleading name of *thermoelectric power*.

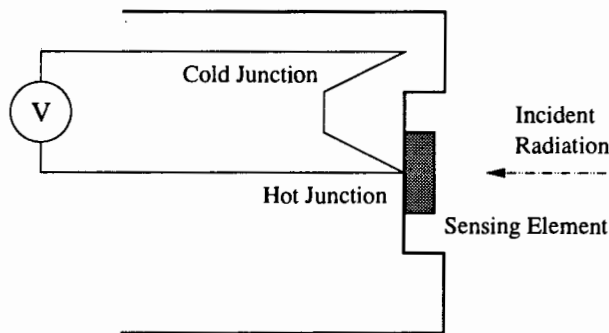


Figure 2.7: A Thermocouple Detector

**Bolometers:** The temperature-dependent property utilised in a bolometer (invented by Langley in 1880) is the electrical resistivity of a metal or semiconductor. A bolometer element can be a thin blackened strip of metal, semiconductor, or super-conductor material. The

change in resistance caused by the heating of the bolometer element is converted into a voltage by connecting the element to a Wheatstone bridge circuit [32, 38]. Two identical elements are used, one being exposed to the radiation whilst the other, shielded from radiation, serves to compensate for slow changes (drifts) in the ambient temperature. The bridge which was initially balanced becomes unbalanced when the bolometer element is irradiated. The resistance varies with temperature as given by

$$R = R_0(1 + \alpha\Delta T) \quad (2.13)$$

where  $R_0$  is the strip resistance when  $\Delta T = 0$  and  $\alpha$  is the temperature coefficient of resistance [36]. In metals  $\alpha$  is positive, while in semiconductors it is negative.

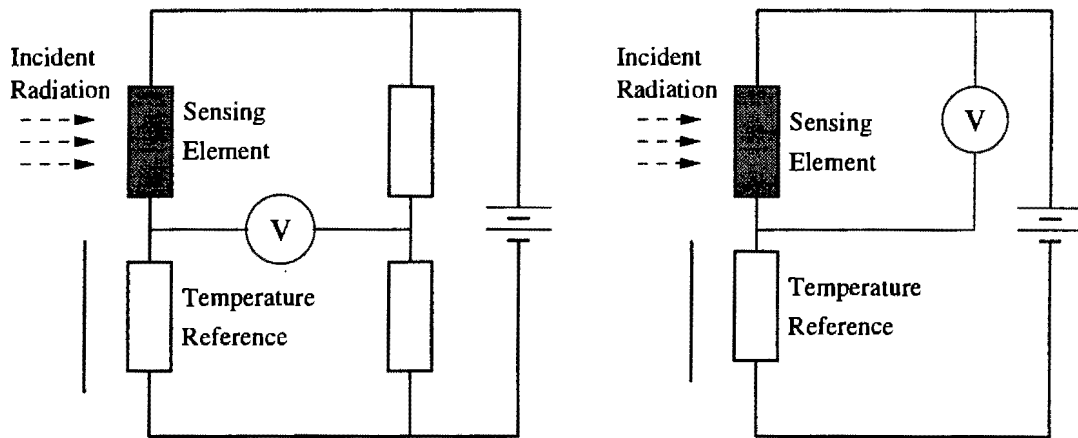


Figure 2.8: Bolometers in Bridged and Unbridged Configurations

The first successful semi-conducting bolometer, or thermistor, was developed by W. H. Brattain and J. A. Becket at Bell Telephone Laboratories in 1964 [32]. The active element is a thin flake of semi-conducting material consisting of a mixture of metal oxides (Mn, Co, Ni). Thermistor bolometers are commercially fabricated in a compact form of small cells provided with an infrared transmitting window or with a focusing hemispherical lens to which they are attached [32]. Germanium bolometers are useful over the 5 to  $100\mu\text{m}$  wavelength region and are usually operated at temperatures below 4.2 K. These low temperature bolometers are housed in a dual cryogenic dewar which can be maintained at liquid helium (4.2 K) or pumped liquid helium (less than 4.2 K) temperatures. Metal bolometers typically have a low resistance ( $10\Omega - 100\Omega$ ) whereas thermistor bolometers have a high resistance (in the order of a few megaohms). Bolometers are particularly useful beyond  $15\mu\text{m}$ , where there are few alternatives except pyroelectric detectors.

**Pyroelectric Detectors:** Pyroelectric detectors are used in many infrared applications, of-

ten replacing more sensitive, but difficult-to-use cooled detectors [38, 36]. Because of their relative lack of detectivity, when compared to semi-conductive devices, they require considerable energy for use. The speed of response of pyroelectric detectors is potentially sub-picosecond, and is currently limited by available electronics [36]. Pyroelectric materials are those wherein the molecule exhibits a net dipole moment. This net dipole moment is temperature sensitive. Energy absorbed by the outer electron cloud, results in a shift, or change, in this dipole moment. In order to return to its original state, the material emits phonons. If the molecules in a pyroelectric material are aligned, the phonons are absorbed by neighbouring molecules. An increase in temperature of the bulk material interferes with this effect because it changes the spacing between molecules. The incident radiation is absorbed in a ferroelectric material that has molecules with a permanent electrical dipole moment. Below a critical temperature (the *Curie temperature*  $T_c$ ) the dipoles are partially aligned along a particular crystallographic axis giving rise to a net electrical polarisation of the crystal as a whole. When the material is heated, the increased thermal agitation of the dipoles decreases the net polarisation, which becomes zero at  $T_c$ .

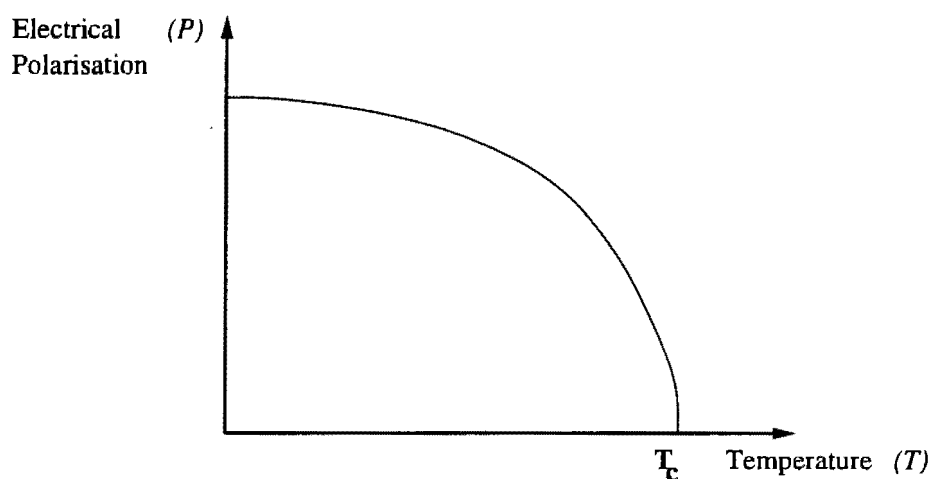


Figure 2.9: Spontaneous Electrical Polarisation versus Temperature for a Ferroelectric Material

The characteristics of pyroelectric devices which make them so desirable in the infrared include stability, ruggedness, speed, economy, broadband response, room temperature operation and large area [36].

Figure 2.10 shows a typical pyroelectric detector [38]. Here, a slab of ferroelectric material is sandwiched between two electrodes (one being transparent). The electrodes are connected by a load resistor  $R_L$ . Radiation absorbed within the ferroelectric material causes it to change its polarisation. The induced charge on the electrodes changes and current flows through  $R_L$ , causing a voltage signal to appear across  $R_L$ .

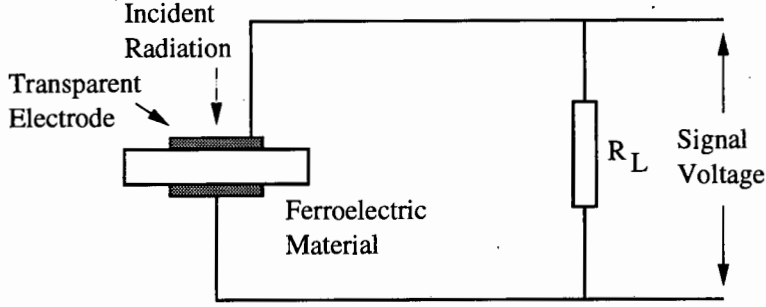


Figure 2.10: A Pyroelectric Detector

Most thermal detectors exhibit a nearly flat spectral response. Their responsivity remains nearly constant over a very wide range of wavelengths in the infrared spectrum. The other class of radiation detectors, the non-thermal (photon) and quantum detectors, show distinctly different spectral responses, characterised by a sharp cutoff in the long-wavelength end.

#### 2.4.2 Non-Thermal Detectors

In non-thermal detectors radiation is converted into electrical signals directly rather than via some temperature dependent process. Non-thermal detectors include quantum detectors and photo-detectors and are usually of the photo-conductive or photo-voltaic type. In quantum detectors the release or transfer of charge carriers (electrons or holes) can be directly associated with the absorption of quanta of incident radiation. This becomes apparent from the fact that their spectral response curve drops sharply to zero at the long wavelength side at some well-defined wavelength. From the point of view of quantum mechanics, the energy of a quantum of radiation of frequency  $\nu$  is

$$\epsilon = h\nu \quad (2.14)$$

where  $h = 6.626 \times 10^{-34}$  J.s is *Planck's constant*. Using the relationship

$$\lambda = \frac{c}{\nu} \quad (2.15)$$

where  $c = 2.9979 \times 10^8$  m.s<sup>-1</sup> is the speed of light in a vacuum, the wavelength associated with a quantum of energy  $\epsilon$  is accordingly

$$\lambda = \frac{hc}{\epsilon}. \quad (2.16)$$

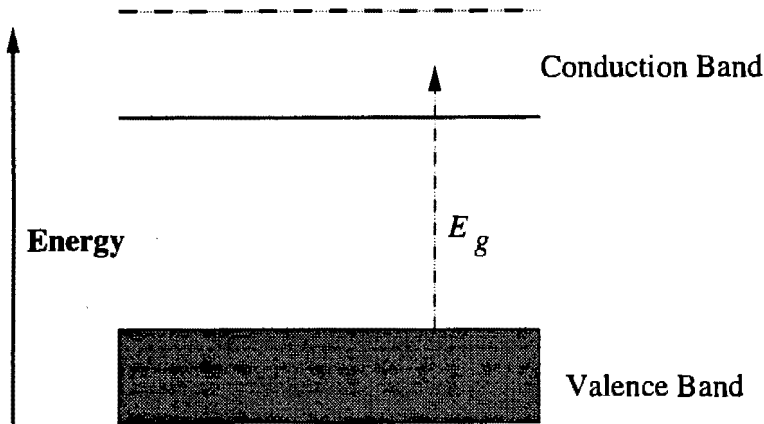


Figure 2.11: Energy Diagram indicating Energy required by an Electron to move from Valence Band to Conduction Band

Since the energy of the radiation quantum is inversely proportional to the wavelength associated with it, it may be concluded that the disappearance of photo-electric activity at some long wavelength indicates the energy of the quanta to be insufficient to set the electrons free. In photo-conductive solids the electron becomes 'free' for conduction only when the energy it gained from the absorbed quantum exceeds the energy gap ( $E_g$ ), which is familiar from the band theory of semiconductors. Thus, the frequency of incident radiation must exceed a predefined threshold for the material before the energy gap is overcome. Hence, the photo-electric effect can only occur at wavelengths shorter than a limit  $\lambda_c$  given by

$$\lambda_c = \frac{hc}{E_g} \quad (2.17)$$

Solid state physicists measure  $E_g$  in electron volts. An electron volt is defined as the energy which a particle carrying one unit of elementary charge ( $1.62 \times 10^{-19}$  coulombs) acquires over a potential difference of one volt. The energy of one electron volt corresponds to that of radiation of  $1.24\mu\text{m}$  wavelength. The detector most suitable for any given wavelength is usually one with its peak sensitivity at or slightly greater than the wavelength in question. There are two reasons for this. Firstly, detectors that are sensitive to wavelengths that are much longer than necessary require more cooling to reduce internal thermal noise [15, 36]. Secondly, there is a theoretical limit to the detectivity set by the amount of radiation the detector receives in its sensitive band from the thermal background radiation, usually at 300 K. This radiation is noisy in nature and gives rise to a limiting noise in the detector. This limits the attainable detectivity to what is called the background limited, or BLIP, value [15].

**Photo-conductors:** When a semiconductor is illuminated with radiation of quantum energy greater than  $E_g$ , some electrons are excited to the conduction band whilst corresponding

numbers of holes are left behind and made mobile in the valence band. Thus, the number of available charge carriers increases, and the conductivity of the material becomes temporarily greater. The responsivity of a photo-conducting detector is then proportional to the excess charge carrier concentration  $\Delta n$ . The steady state concentration is reached when the generation of electrons by absorbed photons equals the rates at which they are removed from the conduction process by recombination with holes and other mechanisms (trapping). If  $Q$  is the number of photons arriving per unit area per second,  $\alpha$  is the optical absorption coefficient, and  $\eta$  the probability of electron excitation resulting from the absorption of a photon (quantum efficiency), then the rate at which electrons are generated per unit volume is  $\alpha\eta Q$ . The recombination rate is directly proportional to the excess concentration  $\Delta n$  and inversely proportional to the average electron lifetime  $t$  in the conduction band. Thus, in steady state

$$\frac{\Delta n}{t} = \alpha\eta Q \tag{2.18}$$

and the (dc) responsivity  $r_0$  is proportional to  $\Delta n/Q$ ,

$$r_0 \propto \frac{\Delta n}{Q} = \alpha\eta t. \tag{2.19}$$

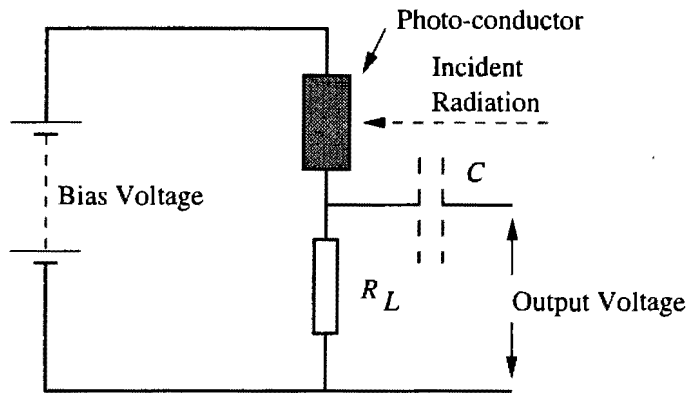


Figure 2.12: Photo-conductor Bias Circuit

Under certain circumstances radiation absorbed in semiconductors can generate a dc voltage rather than a mere change in resistance. Photo-voltaic devices exhibit these characteristics. Essential for their operation is the existence of a barrier layer similar to that existing in semi-conducting rectification diodes. The function of this barrier layer is to separate the oppositely charged carriers and to maintain a potential difference generated under illumination. When the rectifying junction is biased so as to block the current flow, the radiation-generated charge carriers can produce secondary carriers within the collector region, thus multiplying the photo-current. Photo-transistors are based on similar effects.

**Photo-diodes:** Photo-diodes are formed by diffusing a thin layer of  $p$ -type acceptor impurity onto the surface of an  $n$ -type doped semiconductor so that the number of acceptors exceeds that of donors. The  $p - n$  junction is where the  $p$ -type layer joins the  $n$ -type bulk. The layer is thin so that photons can reach the depletion region. Conversely an  $n - p$  junction is formed by diffusing a donor impurity layer onto bulk  $p$ -type material. Near the junction, a depleted region exists which separates the photo-generated electron hole pairs. Most photo-diodes exhibit a fairly abrupt cutoff ( $\lambda_{max}$ ) in response due to a rapid increase in the photon penetration depth near the bandgap. Silicon (and to some extent germanium) declines more gradually in response. Silicon photo-diodes, operated at room temperature, are commonly used for applications between 0.7 to 1.1 $\mu\text{m}$ . Silicon's responsivity increases between 0.7 $\mu\text{m}$  and approximately 0.9 $\mu\text{m}$ . Beyond 1.0 $\mu\text{m}$ , its sensitivity decreases as its absorption coefficient falls. Light penetrates farther into the material and charge collection becomes less efficient. In the near infrared, photons become more deeply penetrating as the wavelength is increased. Thus, light absorbed outside the diffused area may contribute to the optical current.

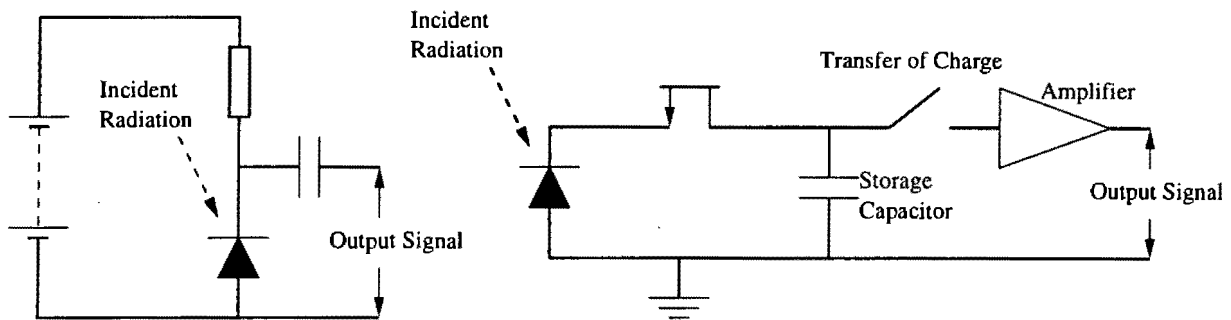


Figure 2.13: Photo-diodes operated in Photo-conductive and Photo-voltaic modes

Photo-diodes are operated in either photo-voltaic or photo-conductive mode. In photo-voltaic mode, the external current flow is very small and the generated external voltage is almost a logarithmic function of the incident light irradiance. In photo-conductive mode, a relatively large reverse bias ( $\approx 10$  V or more) is applied across the diode. In this mode, the external current flowing is directly proportional to the light irradiance [38]. In addition to this inherently linear response, the photo-conductive mode in photo-detectors offers the advantages of faster response, better stability and greater dynamic range.

**Photo-emissive detectors:** Photo-emissive detectors have a spectral response that is limited to the very near infrared. The photo-emission of electrons from metals into a vacuum is governed by the same basic law (Eq. 2.17) as the photo-electric excitation of electrons into the conduction band in semiconductors. The energy barrier that an electron has to cross when ejected from a metal into a vacuum is called the photo-electric *work function* (also measured in electron volts).

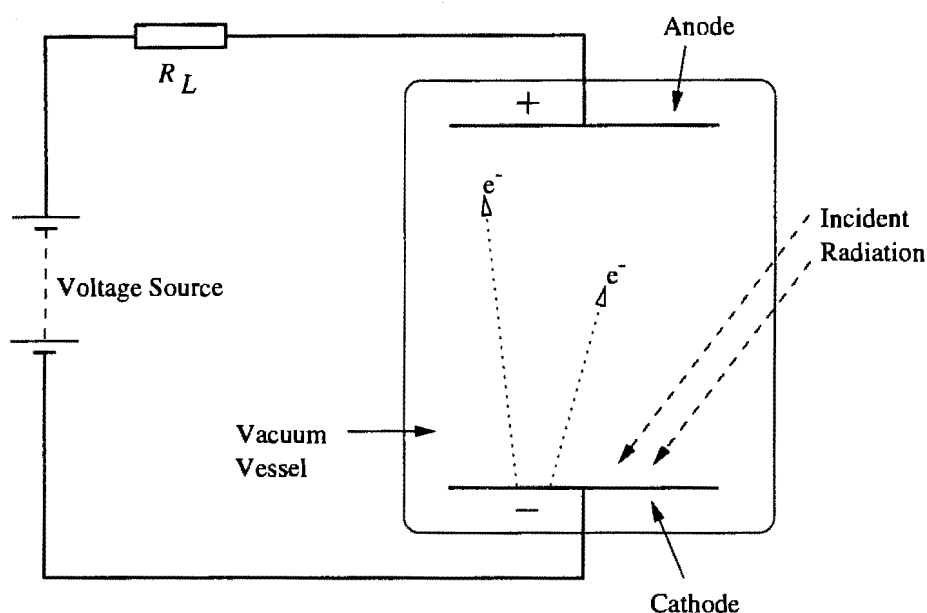


Figure 2.14: Schematic Diagram of Photo-electric Cell

Among the elements, alkali metals have the lowest work functions. The lowest of them corresponds to metallic cesium (about 1.9 eV) [38]. This value relates to a long wavelength of  $0.63\mu\text{m}$ , not good enough for use in even the nearest infrared. In semiconductors and composite surfaces, lower values of work function can be obtained because electrons may be obtained from intermediate impurity levels. One of the most successful of these composite materials is the silver-oxygen-cesium (AgOCs) photo-cathode discovered by L. R. Kroller in 1929 [32]. The spectral response of this material extends from  $0.7\mu\text{m}$  to  $1.0\mu\text{m}$ . The reason that the long-wavelength limit extends so far into the infrared is not entirely clear, but it is believed that photo-emission actually takes place in a layer of cesium oxide, which is an  $n$ -type semiconductor with silver acting as a donor impurity.

A threefold benefit is obtained from operating photo-conductive and photo-voltaic detectors at low temperatures. These include higher responsivity, longer wavelength cutoff, and decreased thermal noise. Non-thermal detectors are also more efficient than thermal detectors as incident radiation is converted to electrical signals via a physical process rather than a strictly thermal process. Large arrays are usually fabricated from photo-voltaic semiconductors due to their lower thermal power dissipation. Photo-voltaic operation also provides a square root of two improvement in noise performance over photo-conductive operation, simpler biasing, and a more accurately predictable responsivity. On the other hand, photo-conductive semiconductors offer high gain, high impedance, and the easier manufacture of single elements [15].

A large plethora of materials is available to match the increasing number of applications, requirements and desires. These different materials respond to different wavelengths and require different operating temperatures. Some practical non-thermal infrared detectors include detectors made from materials like silicon and germanium, lead sulphide and lead selenide, indium antimonide and mercury cadmium telluride. The detection mechanisms present in mercury cadmium telluride will be discussed in detail.

*Silicon and Germanium Photo-Detectors:* Silicon and germanium, sensitive up to  $1\mu\text{m}$  and  $1.8\mu\text{m}$  respectively, are used in applications that usually require a tungsten light source. As a tungsten source emits in the visible region, these detectors are not often thought of as infrared detectors. Approximately 90 percent of the radiation from a typical tungsten lamp is in the infrared region, much of it lying within the spectral bands covered by silicon and germanium. Many specialised forms of silicon and germanium transmitter/receiver component sets exist and these are available as photo-diodes or photo-transistors [33, 39].

*Lead Sulphide and Lead Selenide Detectors:* Ordinarily lead sulphide (PbS) and lead selenide (PbSe) materials are intrinsic photo-conductive thin films with a wavelength response from 1 to  $3.4\mu\text{m}$ . The basic detection mechanism is the photo-conductive effect. These detectors are unresponsive until energised by the application of an electrical bias [15]. Lead sulphide detectors have a peak detectivity at  $2.2\mu\text{m}$  and are characterised by a high input impedance (of the order of a few megaohms) and rather long time constants (typically 100 to  $400\mu\text{s}$ ). Under normal circumstances, PbS detectors provide adequate sensitivity at room temperature. Their performance may be enhanced by cooling to an optimum temperature of approximately 243 K. A peak detectivity of  $4\mu\text{m}$  is obtained at this temperature [33]. These lead salts have been used in thermal imagers and space applications.

*Indium Antimonide Detectors:* Indium antimonide (InSb) can operate in either the photo-conductive semiconductor process, where the conductivity is varied with illumination intensity, or the photo-voltaic mode, where the voltage across the detector is generated from incident light. Detectors from this material are usually formed from single crystal and tend to have low impedances ( $\simeq 50\Omega$ ). Consequently their output voltages tend to be small. At room temperature InSb has a peak detectivity of  $7\mu\text{m}$  [38]. Generally, InSb arrays must be cooled to around 80 K. InSb can also be cooled to liquid helium temperatures to produce the high sensitivity required in astronomy. This detector material is well suited for medium wave infrared (MWIR) thermal imaging, seekers and narrow-band applications in spectroscopy as its detectivity, when cooled, lies in the range from  $2\mu\text{m}$  to  $5.5\mu\text{m}$ , with a peak at  $5\mu\text{m}$  [38].

*Mercury Cadmium Telluride Detectors:* Mercury cadmium telluride (HgCdTe) is the quintessential infrared detector material whose advantages include high sensitivity, cutoff tunability at time of manufacture, and high operating temperatures [15]. Because of these, HgCdTe of-

ten seems to be the material of choice. HgCdTe may be thought of as an alloy composed of semi-metal HgTe and the semiconductor CdTe. Semi-metals have overlapping valence and conduction bands and may be regarded as having a negative bandgap (for HgCdTe the bandgap is  $-0.3$  eV). Consequently, depending on the composition of the alloy, a semiconductor can be formed with a bandgap varying between zero and  $1.6$  eV (the bandgap of pure CdTe) [38]. This material can provide detection from  $2$  to  $26\mu\text{m}$ , but large arrays have been built to a cutoff of only  $10$  or  $11\mu\text{m}$ . Operating HgCdTe at warmer temperatures naturally increases the thermally generated noise. This increase in the noise leads to a decrease in the dynamic range. The biggest drawback with HgCdTe is that it is difficult to manufacture which, in turn, leads to high costs, nonuniformities and unfulfilled performance promises [26]. Aside from the health hazards involved, it has problems associated with compositional control as it is a ternary alloy and thus suffers from poor repeatability in the growth of bulk crystals and alloys. These problems also increase as the cutoff wavelength becomes greater.

HgCdTe can be configured as either a photo-conductive or a photo-voltaic device. The photo-conductive process operates by a photon transferring an electron from the valence band to the conduction band to cause a change in measured conductance. The photo-voltaic process employs electronic circuitry that senses both the electron and the resulting hole. Thus, a photo-voltaic device offers a  $1.414$  (square root of two) increase in the sensitivity for detector noise limited conditions. However, this advantage is offset by the more experienced manufacturing processes of single element photo-conductive HgCdTe. The photo-conductive mechanism dissipates substantially more heat than the photo-voltaic detection mechanism when implemented in HgCdTe: several milliwatts compared to micro-watts or less in the latter [15].

One of the superior properties of HgCdTe, a direct gap semiconductor, is the wide spectral range of detectors that can be made from it. They can work as long-wavelength infrared ( $8 - 12\mu\text{m}$ , LWIR) and medium-wavelength infrared ( $3 - 5\mu\text{m}$ , MWIR) devices because its direct bandgap changes with composition [15]. This property of the alloy allows the bandgap to be tuned during the manufacturing process enabling detector optimisation for the desired optical pass band. The adjustment of the bandpass cutoff results from the relative concentration of mercury to cadmium and the operating temperature. The concentration of cadmium is defined as ' $x$ ', and ' $1 - x$ ' represents the mercury concentration.

Hansen *et al* have reported [10] that the energy gap (cutoff wavelength) can be estimated from the temperature  $T$  and cadmium concentration  $x$  by

$$E_g = -0.302 + 1.93x + (5.35 \times 10^{-4})T(1 - 2x) - 0.81x^2 + 0.832x^3 \quad (2.20)$$

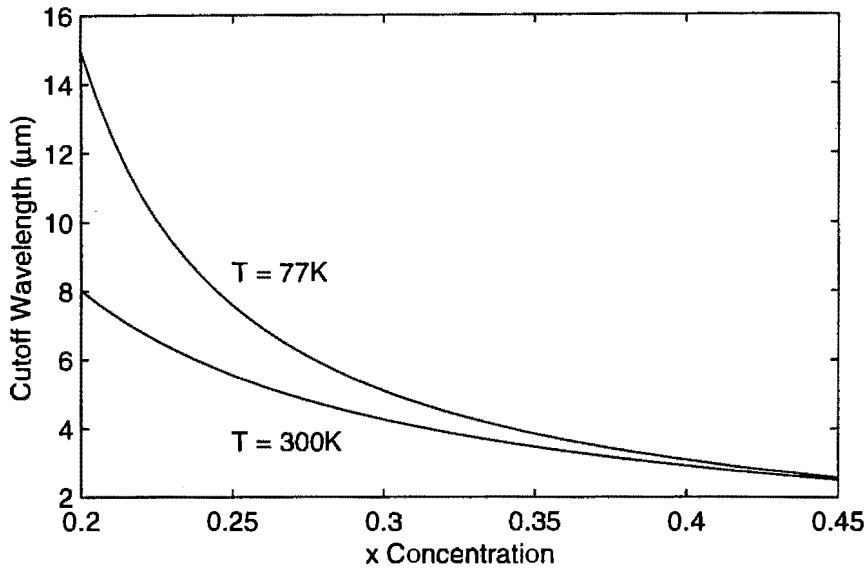


Figure 2.15: Cutoff Wavelength as a Function of  $x$  Concentration for HgCdTe

where  $E_g$  is the bandgap energy in electron-volts,  $T$  is the temperature in Kelvins and  $x$  is the relative decimal concentration between Hg and Cd in the alloy. This equation is plotted for the temperatures of 77 K and 300 K in Fig. 2.15. One notes that the cutoff wavelength is lower for the higher temperature. This curious feature indicates that the wavelength response of a HgCdTe detector can be extended by reducing temperature.

Because of HgCdTe's high sensitivity at higher temperatures and its spectral tunability, it has found a myriad of applications. It is the common material in producing military forward-looking infrared (FLIR) systems, and has also been used in commercial cameras and space instruments [15]. Particular interest has been shown in this material for detectors matching the 3 to 5  $\mu\text{m}$  and 8 to 12  $\mu\text{m}$  atmospheric windows. The former wavelength range incorporates 'hot' military targets (i.e. targets generating much heat) including the engines of tanks, aircraft, ships and land based manufacturing premises. The latter wavelength range includes the peaks of radiation sources at temperatures of 300 K at 10  $\mu\text{m}$  and also the  $\text{CO}_2$  laser radiation at 10.6  $\mu\text{m}$ . HgCdTe is useful for short-wavelength infrared (SWIR) and medium-wavelength infrared (MWIR) detection at temperatures high enough to use thermoelectric or radiative cooling. If high sensitivity is needed with low background radiation, then HgCdTe in the MWIR and SWIR is usually the detector material of choice. In the MWIR, 80 Kelvin HgCdTe can outperform 20 Kelvin doped silicon. HgCdTe is also likely to be the material of choice in high background radiation applications of 14  $\mu\text{m}$  or less when cooling to (or below) 80 K can be guaranteed [15].

### 2.4.3 Some Important Focal Plane Array Detector Properties

Sensitivity is a function of how efficiently an element transduces electrons compared to how much noise it generates in doing so. The issue of sensitivity in infrared focal planes is constantly revisited in sensor design and production as FPA performance frequently drives sensor design. As different materials and applications have different appropriate measures, a great need to standardise the characterisation methods and figures of merit among manufacturers and users has arisen. This increased degree of standardisation has allowed for commercialisation, competition and user friendliness. The figures of merit presented are only applicable to focal plane arrays and not total sensor sensitivities. These figures of merit in and of themselves are independent of the optics but not the bandpass or sampling rate.

**Responsivity:** The purpose of a detector is to convert infrared radiation into an electrical signal - thus the basic property defining the performance is the ratio of electrical output (volts or amperes) to the incident power (watts) on the sensitive area of the detector [15, 32]. This quantity is called the *responsivity* and is simply the output of the detector in volts or amperes normalised to an input power of 1 W. It is important to note the type of radiation specified in connection with the responsivity. It may be radiation at one specific wavelength (monochromatic radiation), which is often chosen to be the wavelength of the peak sensitivity (to give peak responsivity), or it may be blackbody radiation from a source at a specified temperature, usually 500 K (to give blackbody responsivity) [33]. In this case, some of the incident radiation is in wavelength regions where the detector is not sensitive, but all of the radiation is counted in calculating this responsivity. Thus, the blackbody responsivity should be less than the peak responsivity.

**Noise Equivalent Power (NEP):** The importance of cooling the detector to reduce thermally generated noise has been highlighted previously. Such electrical noise sets a limit to the smallest radiation level that can be detected. The noise in a detector is usually quoted as the root mean square value of the electrical output measured in a bandwidth of 1 Hz at some specified centre frequency, under the typical operating condition of the detector [32]. This quantity may be independent of frequency over some range, when it is said to show white noise in that range, or it may vary with frequency. For white noise, the magnitude measured is proportional to the square root of the bandwidth, so that performance is often quoted as volts per unit bandwidth ( $\text{VHz}^{-1}$ )

Noise equivalent power is the incident power on the focal plane that produces a signal exactly equal to the average noise value ( $\text{SNR} = 1$ ) [15]. It is measured in watts. Therefore, if a detector has an NEP of  $10^{-14}$  W, a total power (not flux) of  $10^{-14}$  must be concentrated on the detector by the optics to produce a Signal-to-Noise ratio (SNR) of 1, and  $10^{-13}$  to produce a Signal-to-Noise ratio of 10. The lower the NEP, the higher the sensitivity of the

detector array.

Although low noise enables smaller energies to be detected, it may make the design of suitable amplifiers difficult. For best performance, the amplifier noise needs to be low. It is often of importance to know the ratio of detector noise to the value of Johnson noise in a detector element at room temperature. This value, normalised to the magnitude of the detector noise, may be quoted as a noise factor.

**Area Normalised Detectivity ( $D^*$ ):** All of the above measures vary with the size and shape of the sensitive area of detectors. However, it has been found that for similarly made detector arrays, the NEP is often proportional to the square root of the area of the array [15]. This quantity is called the area normalised detectivity with symbol  $D^*$ . The  $D^*$  figure of merit has several subtleties associated with it. When  $D^*$  is quoted, one does not know if background noise effects,  $1/f$  noise effects and readout noise effects were included. The  $D^*$  value is usually quoted at the peak spectral response, which is usually at a wavelength  $1/2$  or  $1\mu\text{m}$  shorter than the quoted cutoff value. From there it almost falls linearly with bandwidth. Although  $D^*$  may be normalised for sampling rate, it does not provide any analytical representation of  $1/f$  noise. Sometimes  $D^*$  is quoted at a given blackbody temperature, such as 500 K. At other instances it may be quoted using a specific bandpass or just by considering a narrow bandpass of laser light. The detector limited value of  $D^*$ , used for low background radiation and noisy detectors, is given by

$$D^* = \frac{(A_d \times \Delta F)^{1/2}}{NEP} \quad (2.21)$$

where  $D^*$  is the specific detectivity in  $\text{cm}\cdot\text{Hz}^{1/2}/\text{W}$ ,  $A_d$  is the area of the detector in  $\text{cm}^2$ ,  $\Delta F$  is the noise bandwidth and  $NEP$  is the noise equivalent power in W.

## Chapter 3

# Infrared Camera System Overview

### 3.1 Infrared Camera System Constituents

There are many cameras that have the form, feel, and function of a conventional video camera except that they sense the infrared portion of the electro-magnetic spectrum. Infrared systems supplying quantitative temperature data are called *thermographic imagers*, while those that provide qualitative images are called *thermal viewers*. Historically, an electro-optical 'camera' includes neither the storage medium nor the display whereas a 'camera system' comprises of the complete package [15]. In the case of an infrared camera system, the system normally comprises of a camera head, an off-board auxiliary electronics box for sensor control, signal processing and storage, and the display device. If the camera system is aided by a cryo-cooling device, this cryo-cooling device may also be included with the overall system. Figure 3.1 is a typical system diagram of an infrared camera assembly.

#### 3.1.1 The Camera Head

The camera head contains the thermal or thermographic infrared focal plane array (IRFPA), an optical assembly, and a thermal or heat exchange interface for the cryo-cooling mechanism. The optical assembly includes the optics used for image focusing, zooming and spectral filtering. Electronics and motors to control and drive moving parts are also usually included. Some form of thermal reference may be added for self calibration or nonuniformity correction. The control electronics for the focal plane are located in the camera head and consists of communication circuits, bias generators and clock timers. If the focal plane requires cooling, some form of cooling device may be included along with its closed loop cooling electronics. A focal plane's output is of a low voltage and amperage, making it a delicate signal. Therefore, it

### 3.1. INFRARED CAMERA SYSTEM CONSTITUENTS

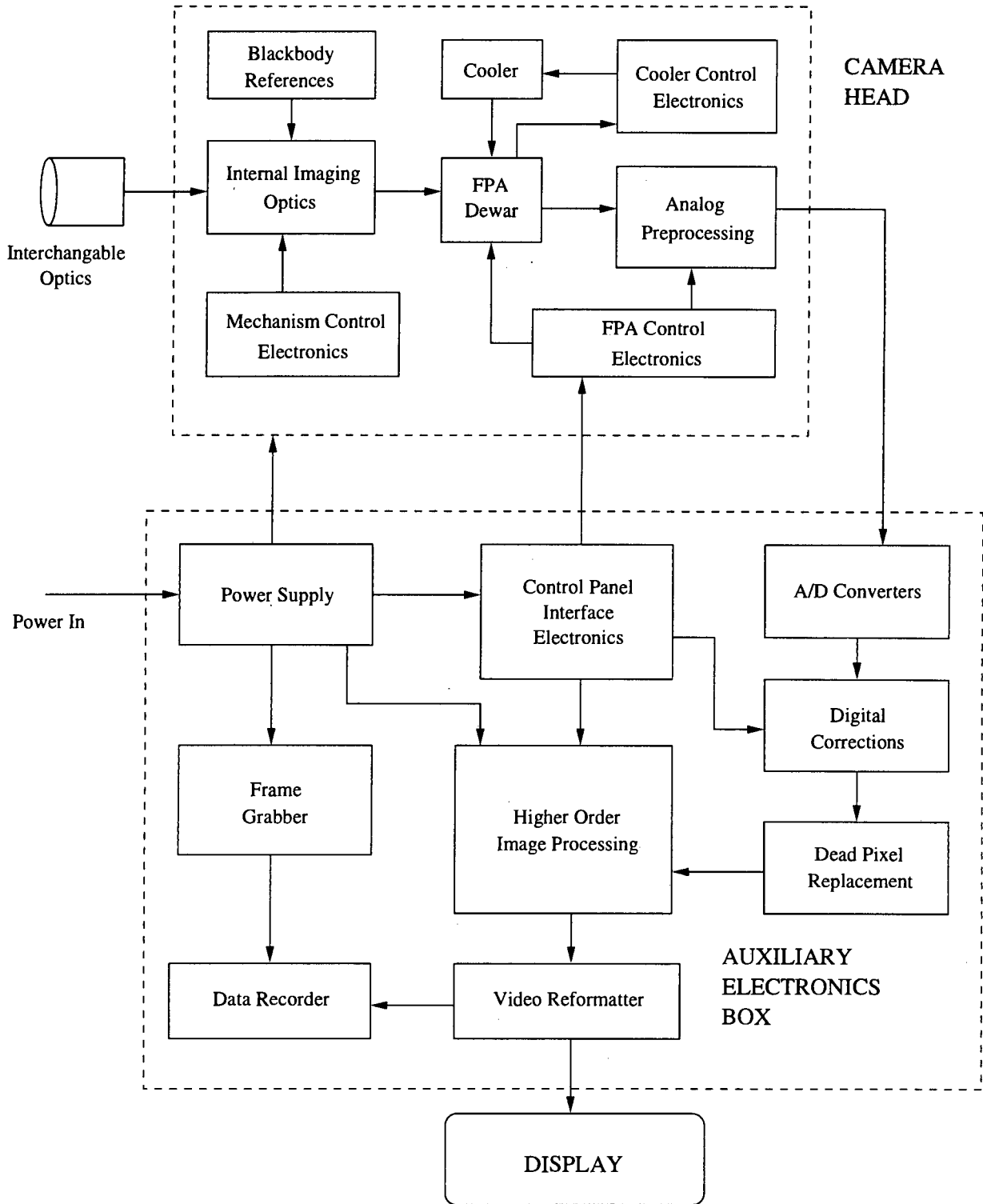


Figure 3.1: Infrared Camera System Assembly

usually requires analog pre-processing, including amplification, control and correction, before it can be sent through a transmission line. The basic analog electronics must be physically near the IRFPA and are included in the camera head. Often, the analog-to-digital converter (ADC) is also included here.

#### 3.1.2 The Auxiliary Electronics Box

The output from a camera head is usually a digital signal or an analog video signal running to an off-board auxiliary electronics box. This support box performs control, image and signal processing, power conversion and video formatting. As image processing is becoming increasingly sophisticated, the hardware utilised for this purpose requires more volume and controls than is often convenient for the camera head. Image processing techniques to process the IRFPA image and apply corrections to eliminate nonuniformities are normally contained in this box. These nonuniformities are present in the input IRFPA image and are the result of detector responsivity variations and fixed pattern noise. Some camera systems use higher-order image processing to provide emissivity subtraction, false colour coding, target identification, tracking and temperature determination. Storage devices for the infrared scenes under view as well as computer interfaces are also included in this off-board electronics box.

#### 3.1.3 Display Devices

Common display devices include cathode ray tubes, and derivatives thereof, used as video monitors. Images and data are usually presented in black and white in real time on these monitors. Older systems included LED arrays for increased portability during field use. Due to large scale computer integration, more recent systems are equipped with the ability to display digitised images on computer terminals along with the search, track and targeting features that the computer provides. Images are also being displayed increasingly in pseudo-colour with computer generated overlays for the purposes of target identification (via template matching) and the locking of weapons onto targets (line of sight criteria, determination of impact points).

#### 3.1.4 Cryo-Cooling Devices

Cryogenic cooling devices form an integral part of infrared sensor architecture as focal plane arrays (FPAs) frequently require some type of cryogenic cooling. Such cooling is inherent to an infrared sensor and is essential for two reasons. Firstly, the detectors may require cooling

just to function, or for increased sensitivity. Secondly, cryogenic cooling reduces thermal noise from filters, baffles and system optics. The extent to which refrigeration is applied depends on the system design, the type of detector material used, bandpass requirements, desired sensitivity, and the expected background.

Usually a detailed sensor system analysis is performed to establish the optimal level of cooling for optical components. It is an accepted rule that the optics will not need to be cooled if the bandpass cutoff is  $11\mu\text{m}$  or less and if the baffle field of view of the FPA is properly designed. However, even with cutoffs of less than  $11\mu\text{m}$ , it is likely that one will still need to cool the closest baffle (the *cold shield*) to the FPA, and probably the spectral filter [15].

For all, but space sensors, such cryogenic components must be isolated from the environment to prevent frosting, reduce the background signal and heat load. A vacuum insulating vessel, called a *dewar*, traditionally contains the FPA, a cold shield and perhaps a filter. The FPA views through a warm window, and cooling is supplied via a thermal attachment to a cryocooler. Newer dewar designs also include the cooler (or part of it) and additional temperature control electronics [15].

Five distinct alternative methods are currently used to provide cryogenic cooling for sensors. These include thermo-electrics, Joule-Thomson blow-downs, closed cycle refrigerators, radiators, and cryogen filled dewar vessels [15, 36].

Thermo-electrics utilise the Peltier effect to cool a small area heat load via a semiconductor process. They are solid state refrigerators with low efficiencies. They are most applicable to spot cooling low loads where the temperature difference between the hot end and FPA are less than 100 K [15].

Open cycle blow-down systems use an expanding gas from a precharged reservoir to cool a small area via the Joule-Thomson effect. Rapid spot cooling can be accomplished. The main drawback is that the gas is a consumable and that the gas contained in the vessel will eventually run out. This type of cooler is useful for systems that have short life and operate only once or a few times [15].

Closed-cycle refrigerators provide cooling via a mechanically driven thermodynamic process, as in a home refrigerator. Cryo-refrigerators are applicable to sensors that require many on/off cycles. Cool-down is not as rapid as with blow-down systems: it can take four to twenty minutes to reach operational temperatures. Traditional drawbacks have include short life, low reliability, large weight and high vibrations. Recent advances have mitigated some of these drawbacks [15].

Radiative coolers consist of orientating a large highly emissive surface to a colder environment

(such as deep space). Usually a small focal plane assembly is attached to a large radiator that radiates the heat away. Radiative coolers are eminently dependable and have provided cooling down to 100 K in space with little or no vibration over years. The main drawbacks are their weight and applicability. There must be a suitable position for the radiator and a proper environment to radiate to. They are most applicable in large, long life space assets and have been used previously on meteorological, deep space and earth resources technology satellites [15].

The vacuum insulating vessels that house the cryogenic portions of infrared sensors are frequently called dewars. In this sense, they are merely the cryogenic insulating assembly, and provide no cooling. The containers of liquid or solid stored cryogenic material (e.g., liquid nitrogen, helium, neon, solid nitrogen, or methane) that provide cooling are also called dewars. Liquid cryogen containment vessels, apart from being heavy and rapidly consumed, are used because they have proven to be reliable, quick to cool, and can accommodate large heat loads.

#### 3.1.5 Temperature Measurements and Correction Criteria

No infrared detector (and therefore no camera) can directly measure temperature [15]. A detector normally senses some version of radiant excitation. An object's temperature is the result of random motion of its constituent molecules. If a sensor directly measured temperature it would not work through insulating media such as the vacuum of space. Clearly, all earth-based temperature measurement (thermographic) infrared cameras do not work through a vacuum. These cameras detect the electro-magnetic radiation emitted as a result of molecular translation, vibration and rotation, and random Brownian motion. The amount of radiation from an object is a function of its surface temperature, emissivity, projected area, reflective characteristics and molecular resonance. The amount of radiation received by a camera from an object and its surroundings is affected by environmental constraints through range, projected areas, reflection, absorption and scatter from any medium between the camera and the object. Finally, the amount of radiance that a camera identifies from the object is also a function of the camera hardware including the optics, spectral bandpass, integration (or exposure) time, and focal plane sensitivity [15].

To produce a temperature measurement from a radiance measurement, processing and calibration must be employed. A temperature can be interpreted only after corrections are made for emissivity, reflection and selective emission/reflection factors. Most cameras ignore selective features by assuming every object is a grey or blackbody of emissivity less than one. Since cameras usually operate in a wide spectral bandpass and these features are often spectrally narrow, this is not a bad assumption. Reflection is much more difficult to compensate for as it

radiation from another hot object some distance away. An example is the phenomenon of the road underneath the engine of a car appearing hot in an infrared image. The road is not actually hot; it is merely reflecting electro-magnetic radiation from the hot car engine.

The emissivity component of a scene can cause a great amount of radiance variation - approximately an order of magnitude in an otherwise low contrast scene [15]. For some applications, such as thermography, emissivity variations must be subtracted out. For other applications, such variations produce an excellent clutter rejection methodology. The temperature component of most terrestrial scenes is the dominant clutter component, and an emissivity map usually is of lower clutter, allowing man made objects to stand out better. Emissivity correction is accomplished by viewing in multiple spectral bandpasses as this provides a large increase in temperature accuracy and measurement reliability. Subtracting out the emissivity can be accomplished with as few as two bands by assuming that everything in the scene is a greybody with constant emissivity over the two bands. Emissivity may then be processed out.

Some military infrared camera systems or thermal viewers are referred to as forward-looking infrared (FLIR) systems. The major distinction between normal infrared cameras and FLIR systems is that normal infrared cameras are designed for generic purposes, without much consideration for form or fit, whereas FLIR systems are designed for specific applications and specific platforms. Cameras are used by computers and machines (not just people) but FLIR systems are used primarily by people (although some weapon systems are controlled by FLIRs) [15]. Cameras can also be used with many different optical configurations whereas FLIR systems are normally custom designed with all optics integrated into the package. The result of current thermography is a highly processed image with the display in false colour, while FLIR images are still displayed in black and white.

## 3.2 The Mercury Cadmium Telluride Infrared Camera

Footage used for the duration of this project was obtained from an infrared camera with a resolution of  $128 \times 128$  pixels. The camera was a thermal viewer and comprised of a medium wave infrared CMOS detector dewar assembly with the detector array fabricated from the ternary alloy, mercury cadmium telluride. The infrared CMOS detection array was integrated into a vacuum dewar. This dewar was equipped with an interface to allow the assembly to be connected to a Stirling cooling machine. An electronics card was used to drive and readout the detector assembly. A cold shield was utilised to limit the incident photon flux and define the field of view of the detector. Thus, the configuration of the detection block is

- 128 × 128 IRCMOS focal plane array
- Dewar assembly
- Cold shield assembly

The electrical, optical and thermal interfaces are described in detail below.

### 3.2.1 Electrical Interface

The electrical interface comprises of the HgCdTe IRCMOS focal plane array, an input stage and an output stage. The sensor array is a readout circuit that comprises of 16384 photo-voltaic diodes multiplexed in 128 lines by 128 columns. This arrangement yields a resolution of 128 × 128 pixels.

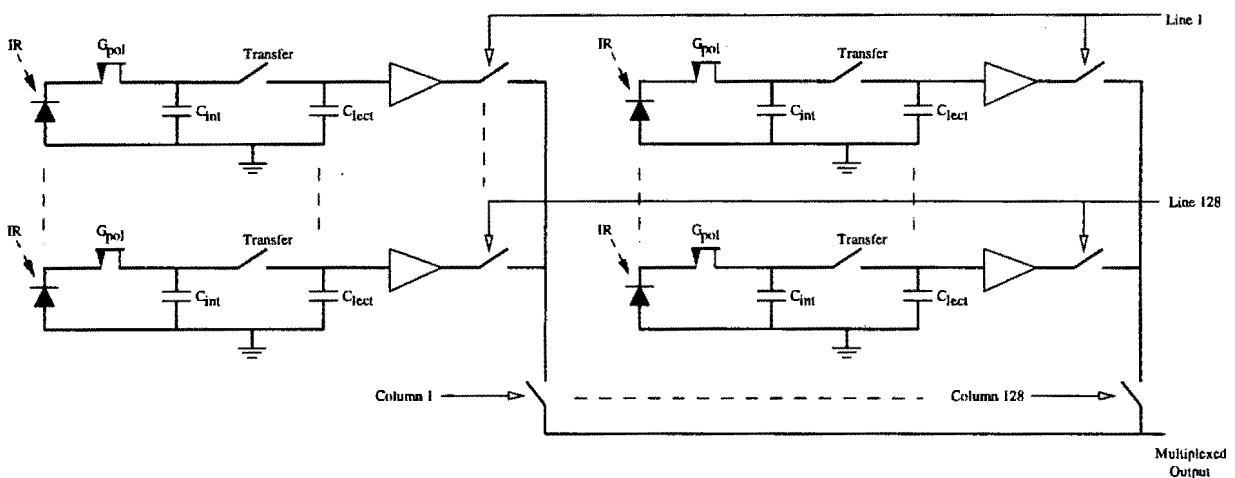


Figure 3.2: Electronic Circuit Diagram of the Input Stage

**The Input Stage:** The input stage, indicated in Fig. 3.2, comprises of a single photo-diode detector element together with a storage capacitor  $C_{int}$  and bias gate  $G_{pol}$ . This bias gate is responsible for setting the bias point for all the photo-diode detector elements. Each photo-diode detector element covers a pixel of the scene within the sensors field of view. When exposed to an infrared scene, a photo-diode detector element develops a voltage across its terminals. All the charges from this photo-diode detector element are collected into the capacitance  $C_{int}$  via the bias gate  $G_{pol}$ .

Each input stage is then addressed one after the other via MOS by multiplexing every line and column into one output channel. An anti-blooming MOS is included to avoid excess of charges in  $C_{int}$  in cases of over-lighting.

**The Output Stage:** As the follower of each elementary input stage is made of small geometry MOS to fit in the detectors pitch, it is not able to directly drive the output charge. In order to compensate for this difficulty an output stage is introduced. The output stage is made of a *P*-type follower so that it is able to adapt to the input stage level. This *P*-type follower is designed to have a gain of approximately unity and, therefore, not decrease the output dynamic. A saturated signal level corresponds to 2 V whereas no signal corresponds to 4 V. Thus, the maximum signal level is approximately 2 V.

**Camera Frame Rates and Data Storage:** The frame rate of the camera is proportional to the master clock frequency. The maximum master clock frequency specified by the manufacturer is 5 MHz. This allows a single field to be obtained in 3.3 ms. There is also a facility to achieve windows of a lower resolution,  $32 \times 32$  and  $64 \times 64$ . This option allows for a control field reduction in order to increase bandwidth. The field rate, with a 5 MHz maximum frequency, is  $820 \mu\text{s}$  for the  $64 \times 64$  window mode and  $204 \mu\text{s}$  for the  $32 \times 32$  window mode. Hence, the faster field rate translates to an obtained image of lower resolution.

For the standard CCIR video rate of 50 fields a second (20 ms), the master clock frequency would have to be 819.2 kHz. As the output from the camera is analog, raw footage from the camera was saved in CCIR format on VHS video cassette. In order to address the problems associated with interlacing, it was decided that each pixel would be represented twice horizontally. This allows for an overall interlaced picture of resolution  $256 \times 256$ .

#### 3.2.2 Optical Interface

Optical interfaces are used to provide a well defined focus location for all incident infrared radiation as well as provide a certain field of view for any position within the focal plane array. As the sensor array is mounted inside a dewar vessel, all incident infrared radiation has to pass through the dewar window, which has to be taken into account in respect of the focal plane's position. Thus, for proper operation of the dewar detector assembly, the detector area has to interface precisely with the actual focal plane array. Optimisation of the detector performance requires an additional cold shield for background radiation reduction. The optical interface therefore consists of:

- Anti-reflection coated infrared window (medium wave bandpass filter)
- A cold radiation shield
- infrared detector location (focal plane)

More detailed information on these constituent parts of the optical interface follows below.

**Anti-reflection Coated Window (Filter):** The function of the infrared window is to allow infrared radiation of the specified optical bandwidth to enter the dewar assembly and focal plane array. As infrared radiation out of the required bandwidth has to be rejected while infrared radiation within the specified bandwidth should have maximum transmission, this window is made of germanium with a high efficiency anti-reflection coating. The spectral transmission range of the window lies between  $3.5\mu\text{m}$  and  $5.0\mu\text{m}$ . The window is also 2.5 mm thick and has a planeity of 10 fringes and parallelism of 1 minute.

**Cold Radiation Shield:** In order to optimise detector performance, all infrared radiation incident from outside the specified detector has to be minimised. This is accomplished by using a cold radiation shield placed on top of the dewar cold finger. The cold shield has an additional selected black coating at the inner surface for infrared reflection reduction. The optical diaphragm of the cold shield is precisely aligned to the infrared detector focal plane array.

**Infrared Detector Location:** The central component of the detector dewar assembly is the infrared detector array. Besides control logic circuits it consists of several infrared sensitive detector elements arranged within a rectangular plane. This active detector plane has to coincide with the actual focal plane position of the incident infrared radiation to provide proper detector performance.

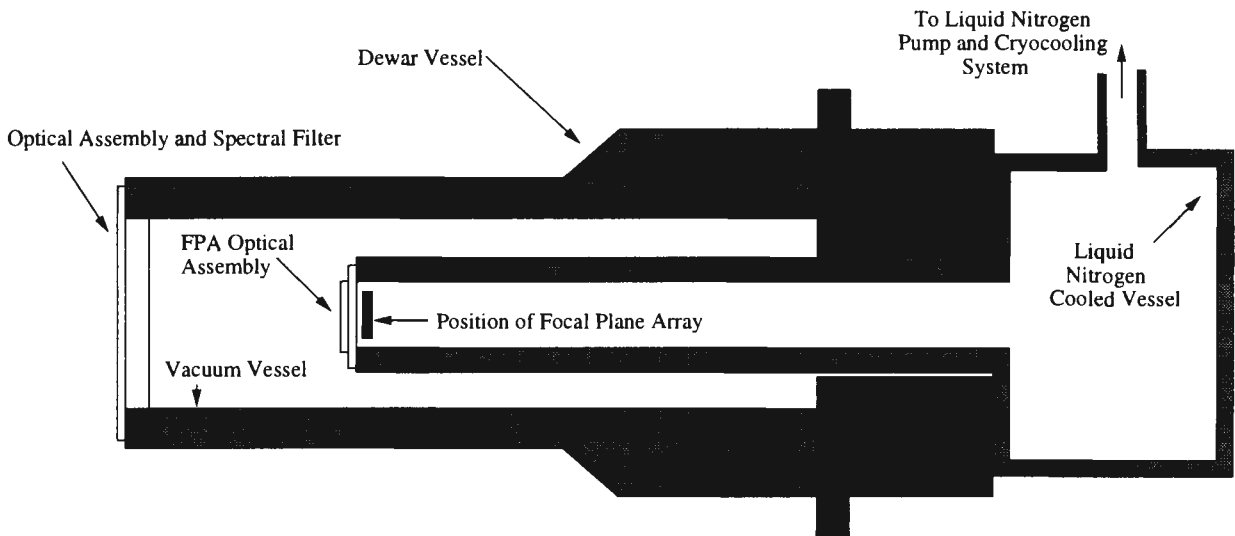


Figure 3.3: Schematic Diagram illustrating the Dewar Vessel housing the Focal Plane Array

### 3.2.3 Thermal Interface

The thermal interface comprises primarily of the cryo-cooler interface, temperature control and vacuum control mechanisms.

**Cryocooler Interfaces:** This camera assembly has been designed to be compatible with a Joule-Thomson cooler or a closed cycle Stirling cooling engine with a 5 mm diameter cold finger. At present a Stirling engine is used and the detector is cooled with liquid nitrogen.

**Temperature Control:** The detector array also contains a temperature sensor diode. However, as this sensor diode cannot be directly calibrated, a representative equivalent set of biased diodes are calibrated. The voltage of the biased diode is representative of the actual temperature being measured.

The base-emitter junction of a 2N2222 transistor is glued near the detector and is used as a temperature sensor. A constant current is injected in the direct path of the diode. For a  $25\mu\text{A}$  current, the bias voltage is 1030 mV at 77 K with a slope of 0.6 K/mV at about 80 K.

**Vacuum Control:** Two reusable electrically activated getters form an integral part of the detection block to ensure the maintenance of a good vacuum in the dewar. This vacuum quality is evaluated by the heat load test which consists of the measurement of the evaporation rate of liquid nitrogen. When the heat load test indicates higher values than normal, getter activation commences as the vacuum inside the dewar is degraded.

## Chapter 4

# Noise Mechanisms in the Detection Process

### 4.1 Temporal and Spatial Noise

The detection of weak infrared signals is limited by the presence of background noise. Noise comprises of spurious signal fluctuations that are undesirable. Low noise performance is important for photo-receivers where low power levels need to be detected. These minimum detectable signals are determined by the photo-detector quantum efficiency and noise sources present in the receiver.

Infrared detectors and focal plane arrays are troubled by two primary types of noise, temporal and spatial noise. These types of noise lead to an overall degraded performance of the detector array in identifying radiation sources accurately and without difficulty. Temporal noise in photo-detectors may be attributed to the random fluctuations of the incident photons that generate electric current [40]. This leads to random fluctuations in the amplitude of the signal. Temporal noise in an imaging system thus appears like a salt and pepper pattern on a display device, which changes with each new frame. The presence of spatial noise in an infrared imaging system can be identified by panning the sensor across a low contrast scene. Spatial noise appears as a pattern that remains fixed on the monitor or display device as the scene passes by. Although the pattern appears fixed, it is typically changing, but at a slower rate than the scene itself changes. This observation leads to the definition of spatial noise as the pixel-to-pixel variations which are correlated from frame to frame when the imaging system is observing a uniform scene. Temporal noise, on the other hand, may be defined as pixel-to-pixel variations which are uncorrelated from frame to frame [18].

$1/f$  noise may be included, to varying extents, as a source of both low frequency spatial and temporal noise and will be discussed in the section on temporal noise.

#### 4.1.1 Temporal Noise

The inherent temporal noise of photo-detectors is of five types: generation-recombination noise, quantum noise, background noise, shot current noise and Johnson noise. If the detector is connected to a receiver, various components in the detector electrical array may contribute to the noise as seen by the receiver.

**Generation-Recombination Noise:** The main source of temporal noise in photo-conductive detectors arise from fluctuations in the rates of the generation and recombination of electron-hole pairs. Generation-recombination noise is also known as *dark current noise* and results from random electron-hole pairs generated due to thermal excitation or by tunnelling mechanisms. The relative importance of thermal processes is strongly dependent on the size of the bandgap since the probability of thermal excitation of a carrier across the gap is approximately proportional to the factor  $e^{E_g/kT}$ . Thus, for detectors capable of operating out to relatively long wavelengths, which consequently have small energy gaps, thermal generation noise is likely to be large unless the temperature is reduced. The operating temperature is usually specified to be  $T < E_g/25k$  [38]. Provided that the thermally generated noise has been reduced to negligible proportions of the rms noise current, fluctuations  $\Delta i_f$  within the frequency range from  $f$  to  $f + \Delta F$  resulting from generation-recombination is given by

$$\Delta i_f = \left( \frac{4ieG\Delta f}{1 + 4\pi^2 f^2 \tau_c^2} \right)^{\frac{1}{2}} \quad (4.1)$$

In this equation  $G$  is the photo-conductive gain,  $\tau_c$  is the minority carrier lifetime and  $i$  is the total current flowing. The noise current given in Eq. 4.1 is almost independent of frequency when  $f \ll 1/(2\pi\tau_c)$ , whilst for  $f > 1/(2\pi\tau_c)$  the noise current declines with increasing frequency. At sufficiently high frequencies the dominant noise mechanism will be Johnson noise [38].

**Quantum Noise:** Quantum noise, closely related to generation-recombination noise, is prevalent when optical processes significantly contribute to generation noise in photo-detectors. When an optical signal enters the detector, the photo-generated electrons carry a quantum noise component. This arises from the intrinsic fluctuation of the photon excitation of carriers. It is fundamental in nature and sets the ultimate limit for detector sensitivity. Both the number of electron-hole pairs generated and the generation rate are statistical random quantities that satisfy Poisson statistics [40].

**Background Noise:** Background noise is the photon noise associated with light reaching the detector from extraneous sources other than the signal of interest, such as sunlight and starlight [40]. This type of noise is particularly detrimental in middle and far infrared detection systems as objects at room temperature emit large amounts of conspicuous thermal radiation in these regions.

**Shot Current Noise:** Defects on the surface of a semiconductor may lead to a surface leakage current and cause surface leakage noise. In a carefully prepared semiconductor detector, this noise is usually negligible. Shot current noise arises from the fact that electric charge is transported by particles of a discrete charge  $q$ . The noise contribution caused by photon current  $I_p$  and dark current  $I_d$ , neglecting background and leakage current, can be treated as shot current noise whose mean square value is given by

$$i_{shot}^2 = 2q[I_p + I_d]B \quad (4.2)$$

where  $B$  is the bandwidth and  $q = 1.60 \times 10^{-19}$  coulombs. Shot noise is a signal dependent noise and has a white spectrum like Johnson noise [32, 40].

**Johnson Noise:** Johnson noise (also known as *Thermal Noise*) results from the statistical thermal fluctuations of electron density in a conductor. Thermal noise is generated in any physical resistor that shows dissipation when a current is passed through it. In a conductor of resistance  $R$  at absolute temperature  $T$  the rms value of voltage fluctuations, observable by a detector that responds to only a narrow frequency bandwidth  $\Delta f$ , is given by

$$\Delta V_j = (4kTR\Delta f)^{\frac{1}{2}} \quad (4.3)$$

where  $R$  is the load resistance of the detector or resistance of the amplifier,  $k$  is *Boltzmann's constant*, and  $T$  is the temperature in degrees Kelvin [32]. Thermal noise may be reduced by increasing  $R$  at the expense of reducing the maximum available bandwidth  $B$ , where  $B = 1/(2\pi RC_d)$  and  $C_d$  is the detector capacitance [40]. The rms value of Johnson noise does not depend on the frequency at which it is measured and is signal independent. It is thus a type of white noise. This type of noise is common to all types of radiation detectors having resistive elements [35, 38].

**1/f Noise:** Any low frequency drift in the operating points of the camera system as a whole that causes the response of individual detector elements to change with respect to each other will introduce spatial noise in the resulting imagery. There are three manifestations of excess low frequency noise in infrared cameras. The first is a drift in the image as a whole. The

second is a drift in the output of the photo-detectors on the focal plane array. In this case the drift of each detector is independent of its neighbours, so a completely random nonuniformity pattern which changes in time will be seen. The third is due to the drift in clocks and biases used to drive the focal plane array. If the individual detectors on the array are not identical, then a nonuniformity pattern that reflects the as manufactured nonuniformities of the array and changes in time will result.

Typically excess low frequency noise is characterised by a  $1/f$  power spectral density. If it is assumed that this is the case for an infrared focal plane array, then the spatial variance will increase as  $\ln(t_c)$ , where  $\ln$  is the natural logarithm and  $t_c$  is the elapsed time since the last calibration for the nonuniformity removal. Hence, if  $1/f$  noise is present in the sensor, the spatial noise will monotonically increase in time, resulting in a continuous degradation in sensor performance [19, 27]. Unlike the sources of temporal noise discussed above, which are well understood, the origin of  $1/f$  noise is still under investigation [11].

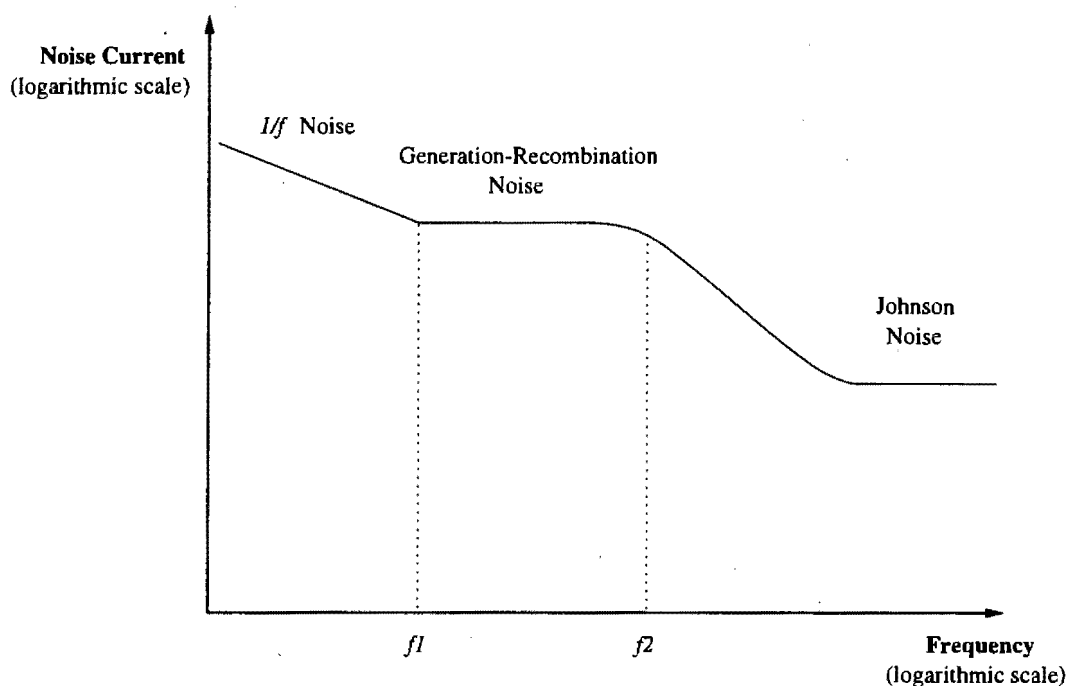


Figure 4.1: Schematic Diagram of the Noise Spectrum for a Photo-conductive Detector

In Fig. 4.1 [38], the frequency  $f_1$  below which  $1/f$  noise becomes dominant is approximately about 1 kHz. Generation-recombination noise has a flat spectrum at frequencies below  $1/2\pi\tau_c = f_2$  where  $\tau_c$  is the minority carrier lifetime. Above  $f_2$ , generation-recombination noise falls with increasing frequency as  $1/f$ . At the highest frequencies Johnson noise will eventually become predominant.

### 4.1.2 Spatial Noise

Perhaps the most difficult problem associated with the use of infrared focal plane arrays is spatial photo-response nonuniformity. As manufactured, HgCdTe focal plane arrays (FPA's) exhibit spatial variations in both dark signal and photo-response. These variations lead to a nonuniform detector response. A further complication is that the individual detectors within the array exhibit differences in spectral response. As a direct result of these variations, the uncompensated imagery of staring infrared cameras usually exhibits an embedded pattern. This pattern is a 'noise fingerprint' of the focal plane response as modified by the camera optical system. Low contrast detail in uncompensated infrared imagery is obscured by the presence of fixed pattern noise. Fixed pattern noise also limits camera sensitivity [19]. Nonuniform detector responsivity and dark current variations can completely mask the useful thermal signatures and pertinent detail in the infrared scene [21]. Thus, valuable scene information is buried in pattern noise.

There are four known sources of spatial noise: nonuniform individual detector element nonlinearities, individual element  $1/f$  noise, array  $1/f$  noise and spectral nonuniformities.

**Nonuniform Individual Detector Nonlinearities:** Nonuniformity in individual detector element responsivity arises from a number of physical processes. Principal sources of nonuniformity in the response of the elements of the detector are due to variations in the following [23, 2]:

- detector element area
- coupling to, and gain of, interfacing electronics
- detector saturation current
- detector quantum efficiency
- detector element cutoff wavelength and spectral response
- focal plane array temperature from point to point

The response nonuniformities in HgCdTe detectors are primarily due to the developmental nature of the materials processing techniques and manufacturing processes [3]. They are also the result of tolerances in lithographic dimensioning and other process control factors [16]. There are also problems associated with the compositional control of HgCdTe as it is a ternary alloy and thus suffers from poor repeatability in the growth of bulk crystals and alloys [15].

Trap assisted tunnelling and internal field emission are mechanisms that usually dominate and contribute to detector dark current in HgCdTe photo-diodes below 77 K [26]. Much of the tunnelling which contributes to dark currents seem to occur due to band bending at the surface (especially due to the small band gap). Unlike silicon, HgCdTe does not form a convenient well-behaved oxide at the surface. Currently, many surface passivation techniques are being investigated. The passivation of HgCdTe is difficult, in part due its complex chemical nature. Additionally, the volatility of the mercury component makes the bare HgCdTe surface extremely temperature sensitive [5]. Thus, passivation and deposition processes are limited to relatively low temperatures. Two popular passivation substrates have been CdTe and CdZnTe. These two substrates are good when the optical signal passes through the substrate and are metallurgically compatible with HgCdTe, but they have several disadvantages, namely fragility, difficulty in single crystal growth, and a poor thermal conductivity at cryogenic temperatures. They also have a large thermal mismatch with silicon as epitaxial layers, which makes it difficult to integrate them with processing circuitry [5].

Inter-detector variations may also result from nonuniform cooling of the detector array as well as varying operating and environmental conditions. The stability of operating temperature of the diode array has been found to affect the response of individual photo-detectors in HgCdTe focal plane arrays [23]. As the array temperature varies, the bandgap of HgCdTe varies, thus shifting the spectral cutoff and changing the apparent responsivity.

**Individual Detector Element and Array  $1/f$  Noise:** Individual detector element  $1/f$  noise is the non-stationary noise that causes each detector element in the array to drift with respect to the other pixels in the array in a spatially uncorrelated fashion. Array  $1/f$  noise is similar to the individual detector element  $1/f$  noise except that some factor external to all of the detector elements is unstable; and the effect of the instability is similar for each individual detector element. Factors like variations in bias voltages and array temperature may cause the entire array to drift. These factors cause individual detector elements to drift coherently, provided the effects are relatively small. The effect of array  $1/f$  noise on imagery is to introduce a pattern onto the infrared image being viewed where the pattern itself changes very little in time, but the magnitude of the pattern is variable [18].

**Spectral Nonuniformities:** Spectral nonuniformities are due to the variations in the spectral response of individual detectors in the focal plane array [18, 19]. With infrared systems, it is often assumed that over a limited range of source temperature, the detector signal can be approximated by a linear function of source temperature. This assumption is based on the approximation of the binomial expansion of the source emittance expressed as  $(T + \delta T)^4$ , which for small  $\delta T$  can be approximated by  $T + 4\delta T$  (assuming that the blackbody flux contributes to the detector signal) [23]. Nonuniformity compensation is achieved by obtaining a normalising function for the detector output voltage as a function of the photon flux. This

approach works well if the major contributions to the detector array nonuniformities are factors such as variations in individual detector area. The detector signals are treated as linear functions of the incident photon flux and are corrected for by adjusting the detector offset and gain accordingly.

For a limited spectral bandpass signal, the detector response will vary as a function of the source temperature in a relationship more complicated than  $T^4$ . The effect of this nonlinear dependence of source flux on source temperature is that the 'shape' of photon flux dependency on temperature changes from element to element within the array. It is this variation of the form of the photon flux dependency on source temperature that limits the effectiveness of all linear compensation methods [23]. Therefore, if the spectral pass band of the elements of an array varies (as in the case of HgCdTe detectors), the temperature response function changes shape from element to element. Since the variations in spectral response between individual detector elements may be large, linear compensation methods can provide only limited correction for scenes composed of different temperatures [19, 23].

## Chapter 5

# Techniques of Nonuniformity Compensation

The presence of spatial noise mechanisms and artifacts of array nonuniformity in detector arrays have emphasised the need for nonuniformity compensation techniques. Infrared scene information, when viewed through an infrared camera using a focal plane array (FPA), normally comprises of contributions from both 'targets' and the 'background'. As background radiation in the infrared scene may be large compared to radiation emitted from source targets, the inherent scene contrast may be low, easily masking pertinent detail. Nonuniformity compensation algorithms have been developed and used to correct for the effects of array nonuniformity and noise mechanisms, leading to enhanced scene contrast. However, the overall performances of some of the older traditional nonuniformity compensation algorithms are often limited by variations in the responsivities of individual photo-detectors within the FPA due to varying field operating and environmental conditions (Background Limited Performance due to background temperature).

In order to perform the required compensation, it is necessary to characterise array elements individually in terms of their responsivity and dark current offset. However, as the variations in the responsivity and offset of individual detector elements are due to a number of independent factors, methods of compensation cannot be optimised to correct for only a particular cause of nonuniformity. Hence, these methods are necessarily only approximate.

Previous methods of nonuniformity correction in infrared detector arrays have involved schemes where the sensor is calibrated by presenting uniform temperature sources of constant intensity over the sensor's field of view. These methods are known as *Single-Point*, *Two-Point* and *Multi-Point* compensation schemes. The concept of using temperature references is based on the premise that by exposing the detector array to known input signal flux levels  $\phi(T)$ ,

individual detector variations can be computed and removed. If two sources of different temperature  $T$  are used (resulting in two different flux levels), as in the case of Two-Point compensation, then a gain  $A_i$  and offset  $B_i$  coefficient for each detector element  $i$  can be determined. Multi-Point compensation, which uses of more than two temperature sources, presents a more complex calibration technique that leads to a greater piece-wise linear approximation of the input/output response curve.

$$Y_i(T) = A_i\phi(T) + B_i \quad (5.1)$$

If the individual detector elements are perfectly linear (within the calibration range) and stable in time, then Eq. 5.1 allows for the correction of pixel nonuniformities. However,  $1/f$  noise [18, 19, 23, 27, 34], nonuniform cooling of the sensor array within the dewar housing, and system instabilities (due to varying operating conditions) increase the overall system noise and create the need for continuing recalibration. This is normally achieved by periodically inserting uniform temperature references into the optical field of view, allowing for the re-calculation of compensation coefficients. An elegant, yet efficient, approach is to perform the calibration of the focal plane detector array in real time based on the statistics of the radiant photon flux from the scene being viewed. Both the *Reference-Free Compensation Scheme* and the *Constant Statistics Algorithm* do not require any temperature references for calibration. These methods dispense with traditional temperature references as they operate by using the statistics of movement in the infrared scene as well as the motion of the detector assembly for the continuous calculation of compensation coefficients. By applying these re-calculated coefficients on a per frame basis, continuous recalibration of the sensor array is achieved.

Some older imaging systems are calibrated with temperature references at startup only. Hence, drifts in the responsivity of photo-detector array elements and operating parameters, that arise from low frequency noise artifacts and varying environmental conditions (temperature and atmospheric pressure), are unaccounted for. In systems where continuing recalibration is needed, traditional methods of incorporating temperature references in the optical field of view involve the use of complex optical assemblies that include electro-mechanical/electro-optical shutters and synchronised spinning mirrors/beam interrupters. These systems are complex, with numerous components decreasing the overall system robustness often needed in tactical military systems for purposes of quick field deployment. Reference free correction techniques, using time averages of the data and scene intensity statistics, continuously calculate correction coefficients. Compared to temperature reference methods, these methods also ensure that the calculated coefficients continually track variations in the dark currents of individual array elements as well temperature changes within the dewar sensor cooling vessel. Reference free methods do, however, suffer from the disadvantage of being motion

dependent. Motion within the infrared scene under view, or camera panning is required to obtain the scene statistics needed for the compensation algorithms. If there is no motion, then the compensation process will essentially fade out the stationary image. In practice, this is not a serious problem as the amount of motion required is relatively small and may be obtained by slowly panning the detector array.

The implementation of reference free correction techniques lead to a much lower system overhead in terms of overall weight, complexity and difficulty in the calibration process. In camera systems using these methods, less power would also be consumed as none is needed for the temperature references and drive motors that form part of the optical assembly. The above factors contribute to increased robustness and portability of such systems for field use.

## 5.1 Correction Schemes Using Temperature References

### 5.1.1 Single-Point Compensation

A simple method for reducing the spatial noise at the output of an imaging sensor is to use a single temperature reference, hence single calibration flux level [18, 24]. In this scheme, each detector element  $i$  is offset adjusted by its own particular constant, so as to render the image free of spatial noise at one (uniform) source temperature. If this calibration temperature is denoted as  $T_{cal}$  and the Single-Point corrected output is denoted as  $Y_i$ , then the algorithm may be described mathematically as

$$Y_i(T_s) = N_i\phi(T_s) - N_i\phi(T_{cal}) + \overline{N_i\phi(T_{cal})} \quad (5.2)$$

where  $N_i\phi(T_s)$  is the output voltage of detector element  $i$  at temperature  $T_s$  and  $N_i\phi(T_{cal})$  is the stored compensation constant obtained at the calibration temperature.  $\overline{N_i\phi(T_{cal})}$  represents the array-wide average output voltage at the calibration temperature. Clearly, the Single-Point corrected output is perfectly uniform when the source temperature,  $T_s$ , equals the calibration temperature,  $T_{cal}$ . Under this condition

$$Y_i(T_s) = Y_i(T_{cal}) = \overline{N_i\phi(T_{cal})} \quad (5.3)$$

This scheme allows for the removal of fixed pattern noise due to dark current offsets. However, variations in the responsivity of individual detector elements are not corrected. The scheme works well in the case where detector elements have similar responsivities but significant variations in dark current offset.

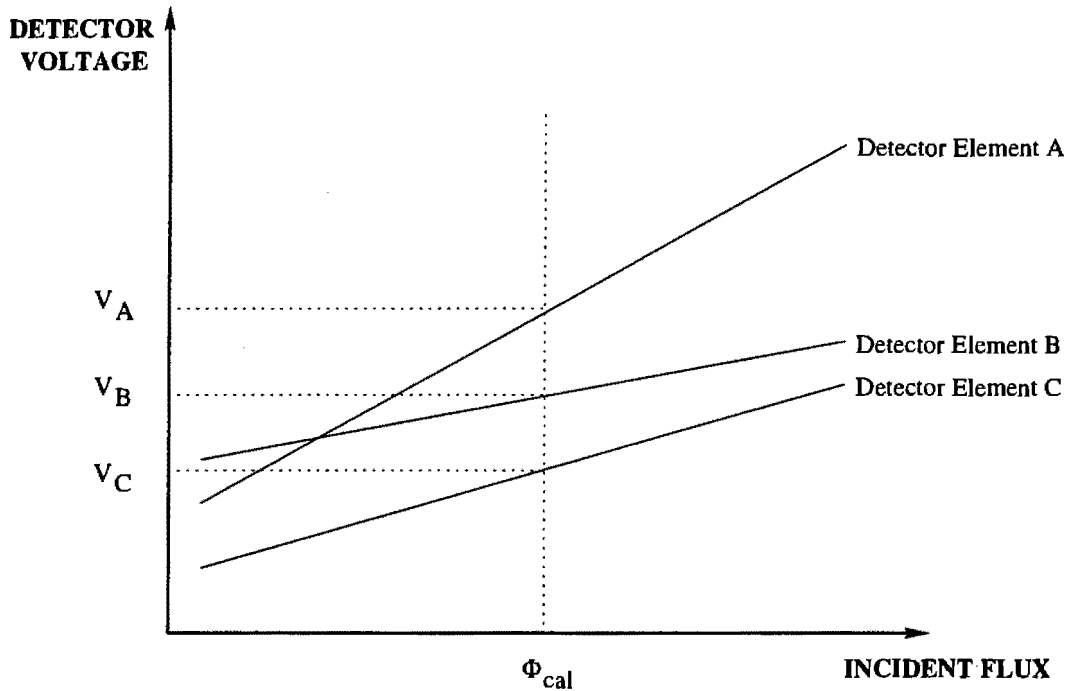


Figure 5.1: Output Voltages of Individual Detector Elements when a Single Flux Source is used

### 5.1.2 Two-Point Compensation

Many infrared detector and visible charge-coupled-device (CCD) focal plane models linearise the response of an individual detector element  $i$  in the focal plane array to the incident flux  $\phi(T)$  by

$$Y_i(T) = R_i\phi(T) + O_i \quad (5.4)$$

where  $R_i$  is the 'responsivity' or gain term and  $O_i$  is a constant offset representing background and dark currents. If the individual detector responsivities are linear, it is possible to correct for nonuniformities using a simple algorithm that corrects each detector for both offset and responsivity variations. This approach to nonuniformity correction measures the response of each individual detector element at a high and low flux value and uses the calibration data to calculate corrected responses at intermediate flux values. Figure 5.2 establishes hypothetically the differences in output voltages obtained by individual detector elements when different sources of incident flux are viewed.

In traditional Two-Point compensation schemes, two uniform temperature sources at  $T_1$  and  $T_2$  are presented to the detector array [3, 14, 16, 23, 24, 27, 28, 31].

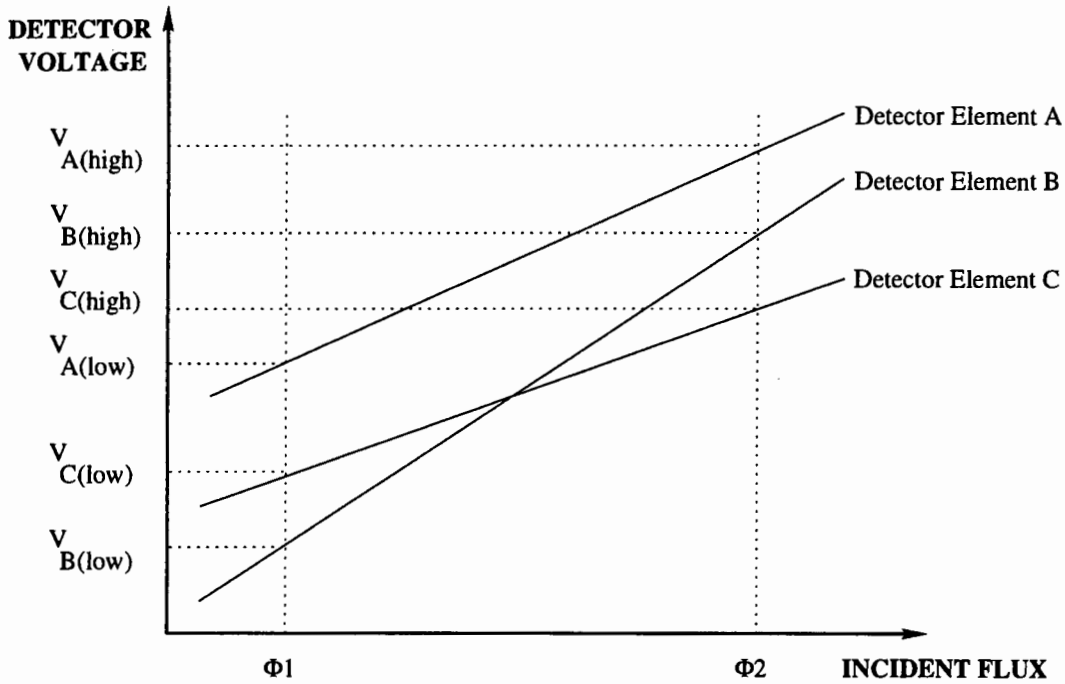


Figure 5.2: Output Voltages of Individual Detector Elements when Two Different Sources of Incident Flux are used

$T_1$  is usually a cold temperature reference and  $T_2$  a hot temperature reference. The detector array is first 'cold shuttered' (exposed to the cold reference) and then 'hot shuttered' (exposed to the hot reference) and the array's response to each one of them is measured. The values of  $R_i$  and  $O_i$  are calculated by the equations

$$R_i = \frac{Y_i(T_1) - Y_i(T_2)}{\phi(T_1) - \phi(T_2)} \quad (5.5)$$

and

$$O_i = Y_i(T_1) - R_i\phi(T_1) \quad (5.6)$$

or

$$O_i = Y_i(T_2) - R_i\phi(T_2) \quad (5.7)$$

These coefficients are stored for each detector element and used to compensate subsequent detector outputs. Staring arrays and FLIR systems employing Two-Point correction tech-

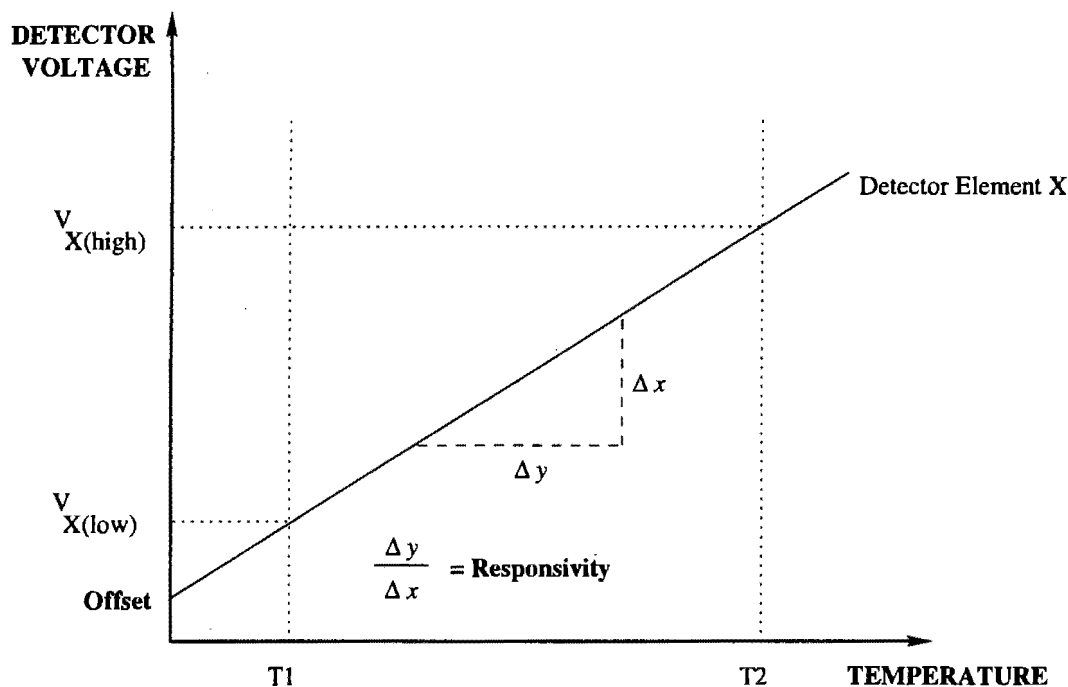


Figure 5.3: Individual Detector Element Offset and Responsivity

niques normally require mechanical or electro-optical shutters which completely interrupt the field of view of the sensor during the calibration process. This arrangement leads to a greater mechanical complexity of the overall system if regular calibration is required.

### 5.1.3 Multi-Point Compensation

Multi-Point compensation schemes comprise of both linear and quadratic/cubic methods. Both linear methods and quadratic/cubic methods involve the use of more than two uniform temperature sources. A Four-Point linear scheme would use four different uniform temperature sources to obtain piecewise linear portions within an individual detector's response curve [3]. Linear interpolation is used between the calibration points. The error incurred in this case is generally smaller than the Two-Point correction scheme due to the more accurate piecewise linear model. A technique using linear interpolation with three sources of incident flux is shown in Fig. 5.4.

Quadratic and cubic methods involve the fitting of mathematical functions to the response characteristics of individual detectors within the array. Though computation intensive, the implementation of such nonlinear compensation schemes results in a much improved correction to the estimate of source temperature compared to the estimates made by using linear compensation schemes [23]. These methods do however present the drawback of needing cal-

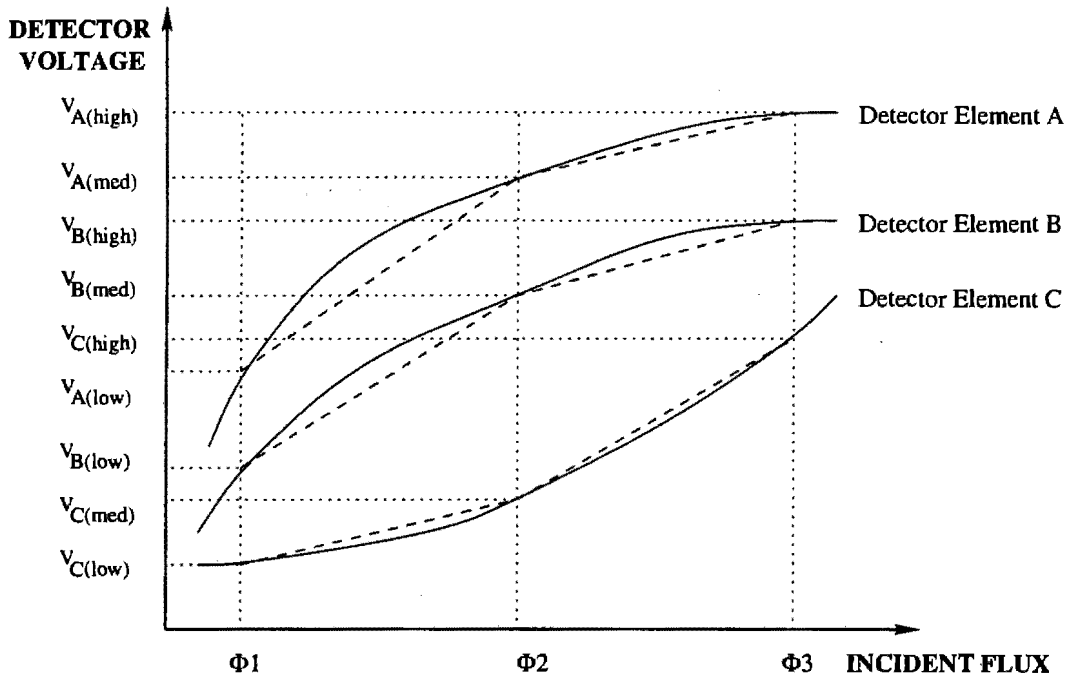


Figure 5.4: 3-Point Linear Interpolation Technique using 3 Different Flux Sources

ibration of the array at a number of temperatures that is at least one greater than the degree of the polynomial. They also require an evaluation of the roots of the polynomial to obtain an estimate of source temperature. The effectiveness of compensation improves with the degree of the polynomial [23].

The variation of total blackbody photon flux with the third power of the source temperature implies a compensation scheme based on modelling the detector signal as a power of the source temperature [23]. This nonlinear method requires the fitting of a power law of the form

$$V = aT^b \tag{5.8}$$

to individual array element signals obtained during the calibration using sources at a number of temperatures. The inverse of this equation is then used to estimate source temperature from the detector output. To implement the correction scheme presented by Paropat [23], the focal plane array is exposed to a blackbody source at three known temperatures, which are chosen to lie in the range of temperatures expected in the image field. The outputs of the array elements are observed at each of these temperatures, and the power law curve is fitted to the element responses using a least squares estimation of parameters  $a$  and  $b$ .

The compensation of the detector response is complicated by the fact that there are usually components of flux incident on the detector that do not originate from the scene being imaged. These components are due to dark current and residual offsets. The power law correction curve may then be modified to include a constant to help minimise these effects and provide better compensation. This modification of the power law curve may be expressed as

$$V = aT^b + c \quad (5.9)$$

The constant  $c$  is estimated initially, with  $a$  and  $b$  evaluated as described previously. An iterative procedure is then used with varying values of the constant  $c$  to obtain the best fit to the data.

## 5.2 Reference Free Correction Schemes

### 5.2.1 The Reference-Free Compensation Scheme

The Reference-Free Compensation scheme, proposed by Narendra [21], uses the assumption that due to motion in an infrared scene (or camera panning) over a period of time, all the detectors in the array will be exposed to similar scene intensity statistics. Put simply, the mean flux over a period of time incident on the detector array, as well as the standard deviation of the flux, should be the same for every detector element in the array.

The responsivity and offset components ( $R_i$  and  $O_i$ ) of each detector element are computed as a function of the first and second order statistics of the detector array output over a period of time. The mean and variance of the measured output  $Y_i(t)$  may be written as

$$\begin{aligned} \bar{Y}_i &= E[R_i\phi(T) + O_i] \\ &= R_iE[\phi(T)] + E[O_i] \\ &= R_iE[\phi(T)] + O_i \\ &= R_i\overline{\phi(T)} + O_i \end{aligned} \quad (5.10)$$

$$\begin{aligned} \sigma_{Y_i}^2 &= \text{var}[Y_i] \\ &= \text{var}[R_i\phi(T)] + O_i \end{aligned} \quad (5.11)$$

$$= R_i^2 \sigma_{\phi(T)}^2$$

Without loss in generality it can be assumed that  $\phi(T)$  is zero mean (i.e.  $E[\phi(T)] = 0$ ). Hence, the unknown variables  $R_i$  and  $O_i$  can be recovered by using the following relationships:

$$\begin{aligned} O_i &= E[Y_i] \\ &= \bar{Y}_i \end{aligned} \tag{5.12}$$

and

$$R_i = \frac{\sigma_{Y_i}}{\sigma_{\phi(T)}} \tag{5.13}$$

For discrete-time signal processing, the following estimates of mean and standard deviation are used:

$$\bar{Y}_i(n) = \frac{1}{n} \sum_{k=1}^n Y_i(k) \tag{5.14}$$

$$\sigma_{Y_i}(n) = \sqrt{\frac{1}{n-1} \sum_{k=1}^n [Y_i(k) - \bar{Y}_i(k)]^2} \tag{5.15}$$

Examining Eq. 5.13 it can be seen that  $\sigma_{Y_i}$  is equal to  $\sigma_{\phi(T)}$  multiplied by the scaling factor  $R_i$ . Thus, a zero mean unity variance signal  $X_i$  can be generated with the following shift-normalisation formula:

$$\begin{aligned} X_i &= \frac{Y_i - \bar{Y}_i}{\sigma_{\phi(T)}} \\ &= \frac{Y_i - \bar{Y}_i}{\frac{\sigma_{Y_i}}{R_i}} \end{aligned} \tag{5.16}$$

### 5.2.2 The Constant-Statistics Algorithm

In order to simplify computation, Chiang proposed using the  $L_1$  norm definition of the standard deviation in Eq. 5.15 instead of the usual  $L_2$  norm definition in the Reference-Free Compensation scheme. He also went on to state that using the  $L_1$  norm gives similar performance compared to using the  $L_2$  norm [6]. The definition of the  $L_1$  norm is given by

$$\sigma_{Y_i}(n) = \frac{1}{n-1} \sum_{k=1}^n |Y_i(k) - \bar{Y}_i(k)| \quad (5.17)$$

Equations 5.14 and 5.17 may be simplified to recursive versions which further reduce the amount of computation performed at each iteration. By using these recursive equations, presented below, only four multiplications/divisions and four additions/subtractions are required per detector element per step.

$$\bar{Y}_i = \frac{Y_i(n) + (n-1)\bar{Y}_i(n-1)}{n} \quad (5.18)$$

$$\sigma_Y = \frac{[Y_i(n) - \bar{Y}_i(n)] + (n-1)\sigma_{Y_i}(n-1)}{n} \quad (5.19)$$

### 5.2.3 The Fading-Memory Polynomial Filter

In order to better estimate low frequency changes of gain and offset and compensate for  $1/f$  noise in the detector array, a Fading-Memory Polynomial filter may be used. As seen above in both the Reference-Free Compensation scheme and Constant-Statistics algorithm, each value in the averaging filter has equal weighting which causes the filter to lag. The Fading-Memory Polynomial filter, proposed by Morrison in [20] and used by Scribner in [30], has a window of length  $M$  that is weighted exponentially so that the most recent value in the window will be weighted the most, whilst the oldest value in the window is weighted the least. This ensures that the filter output will be able to compensate for low frequency changes in the spatial noise of the input image more quickly but still be able to obtain an overall noise fingerprint due to the fixed pattern noise in the input images.

The implementation of the Fading-Memory Polynomial filter, as indicated in Eq. 5.20, approximates a recursive temporal high pass filter. It does not need all the values in the window to be stored but only the previous value. Hence, the previous output value contains all the information about the exponentially weighted values in the window. The present value may then be calculated from the previous value by the means of the recursive algorithm given

below

$$X_i(n) = \frac{Y_i(n) - f_i(n)}{\frac{\sigma_{Y_i}}{R_i}} \quad (5.20)$$

where

$$f_i(n) = f_i(n-1) + (1-\theta)\epsilon(n) \quad (5.21)$$

and

$$\epsilon(n) = Y_i(n) - f_i(n-1). \quad (5.22)$$

$X_i(n)$  is the filter output,  $Y_i(n)$  is the filter input and  $\theta$  is the exponential weighting value, where  $0 < \theta < 1$ . The prediction error  $\epsilon(n)$  is the difference between what is actually observed at time  $(n)$  (namely  $f_i(n)$ ), and what is predicted for time  $(n)$  based on observations up to time  $(n-1)$  (namely  $f_i(n-1)$ ). Simplifying Eq. 5.21 yields

$$f_i(n) = \theta f_i(n-1) + (1-\theta)Y_i(n) \quad (5.23)$$

The scaling factor  $\theta$  forms the exponential weighting factor. The filter can be shown to be stable for values between 0 and 1, 1 making the window infinitely long and 0 making the window zero. Thus, expressing Eq. 5.23 in terms of a window of length  $M$ , one obtains

$$f_i(n) = \frac{1}{M}Y_i(n) + \left(1 - \frac{1}{M}\right) f_i(n-1) \quad (5.24)$$

In order for the filter to be stable,  $f_i(n-1)$  needs to be initialised with the correct value. The correct initial value for  $f_i(n-1)$  can be found by finding the average of a number of input images, in an equally weighted window of length  $M$ . This value of  $f_i(n-1)$  is found by calculating the average value of input images in the equally weighted window as shown below

$$f_i(n-1) = \frac{1}{M} \sum_{k=1}^M Y_i(k) \quad (5.25)$$

Because this filter has an exponentially weighted window, the most recent value would have the most weighting. It would thus be able to respond to low frequency noise artifacts and

compensate for  $1/f$  noise.

### Magnitude and Phase Response of the Fading-Memory Polynomial Filter

The  $z$ -transform system function of the temporal high pass filter,  $H(z) = X(z)/Y(z)$  can be shown to be

$$H(z) = \frac{(M-1)(z-1)}{Mz - (M-1)} \quad (5.26)$$

Substituting,  $z = e^{j\omega\tau}$ , where  $\tau$  is the sample time, gives the simulated analog frequency response of the system

$$A(\omega\tau) = H(e^{j\omega\tau}) \quad (5.27)$$

Therefore

$$A(\omega\tau) = \left( \frac{(2M^2 - 4M + 2) \cos(\omega\tau) - 2M^2 + 4M - 2}{(M^2 - 2M) \cos(\omega\tau) - 2M^2 + 2M - 1} \right)^{\frac{1}{2}} \quad (5.28)$$

A parametric magnitude plot of this function for windows of length  $M = 20, 50$  and  $100$  is illustrated in Fig. 5.5, where the Nyquist frequency is  $f_{nyquist}\tau = 0.5$  (which is equivalent to  $\omega_{nyquist}\tau = \pi$ ). The standard deviation used in the Fading-Memory Polynomial filter is calculated using the  $L_1$  norm to allow for computational saving.

The filter can be seen to have an initial gain of zero which increases with frequency, tending to 1 at a frequency of  $\pi$ . The roll off at lower frequencies can be seen to be  $-20$  dB per decade because this filter is a first order filter.

The analog phase response of this filter can be found by the argument of  $H(\omega\tau)$ . This analog phase response of this filter (after much simplification of the original equation) may be given by

$$P(\omega\tau) = \arctan \left( \frac{\sin(\omega\tau)}{(2M-1)(1-\cos(\omega\tau))} \right) \quad (5.29)$$

The normalised phase plot of this filter for a normal frequency scale (between  $0 < \omega < 2\pi$ ) as well as a log frequency scale are indicated in Fig. 5.6 and Fig. 5.7. This filter introduces a zero phase shift as long as  $\omega$  is less than  $2\pi$ . The phase of the filter is also seen to repeat at multiples of  $2\pi$ .

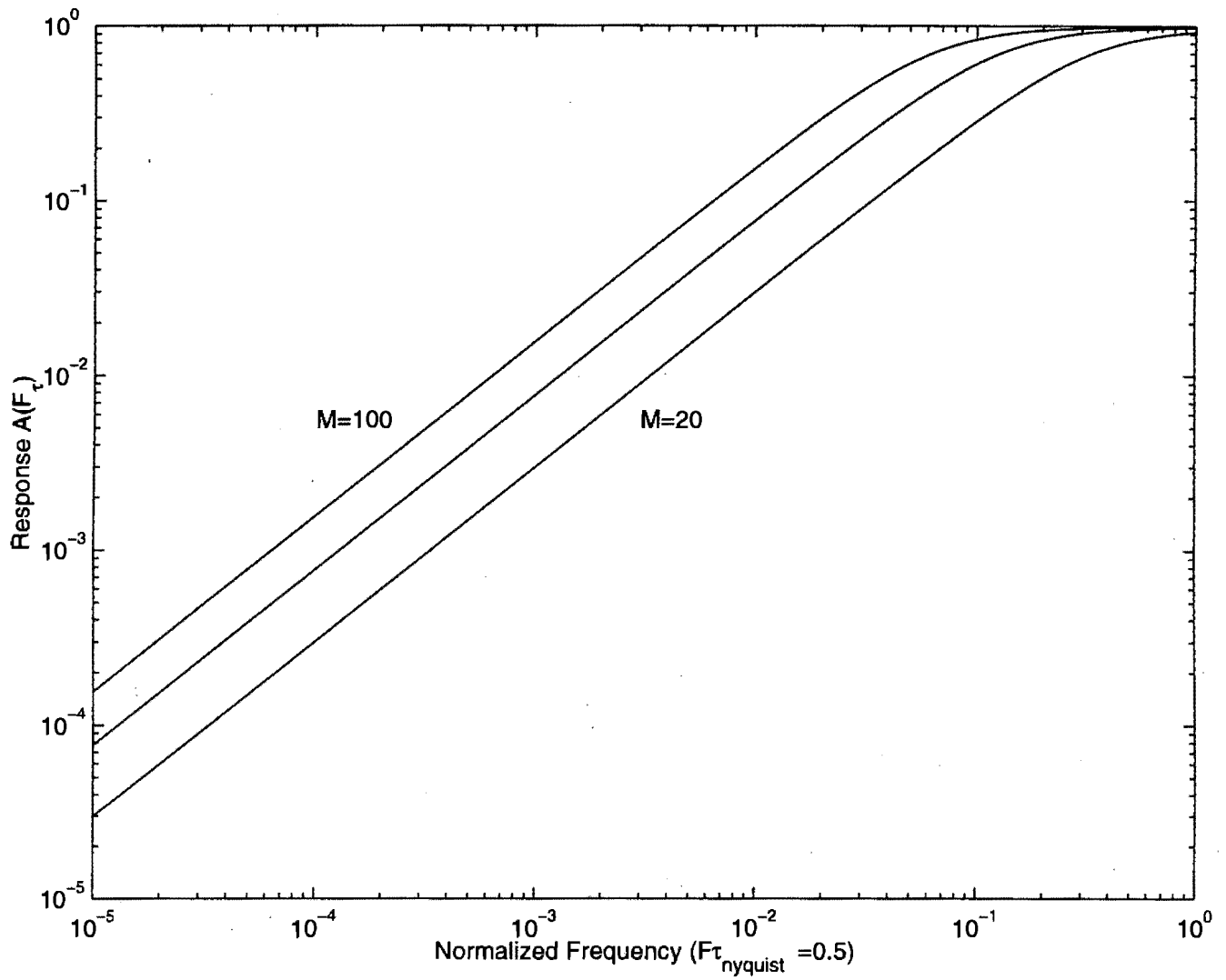


Figure 5.5: Simulated Analog Magnitude Response of the Fading-Memory Polynomial Filter

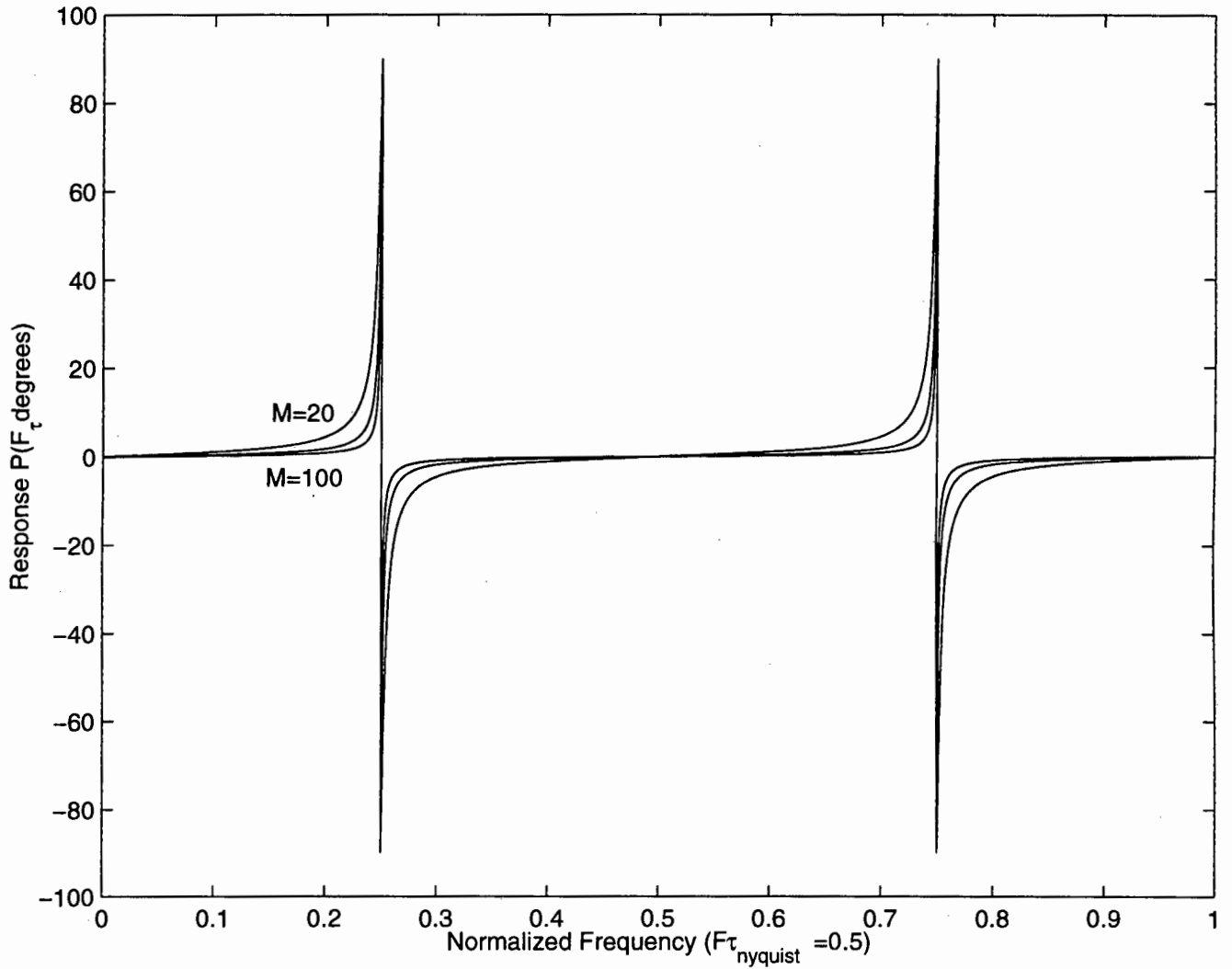


Figure 5.6: Simulated Analog Phase Response of the Fading-Memory Polynomial Filter (Normal Frequency)

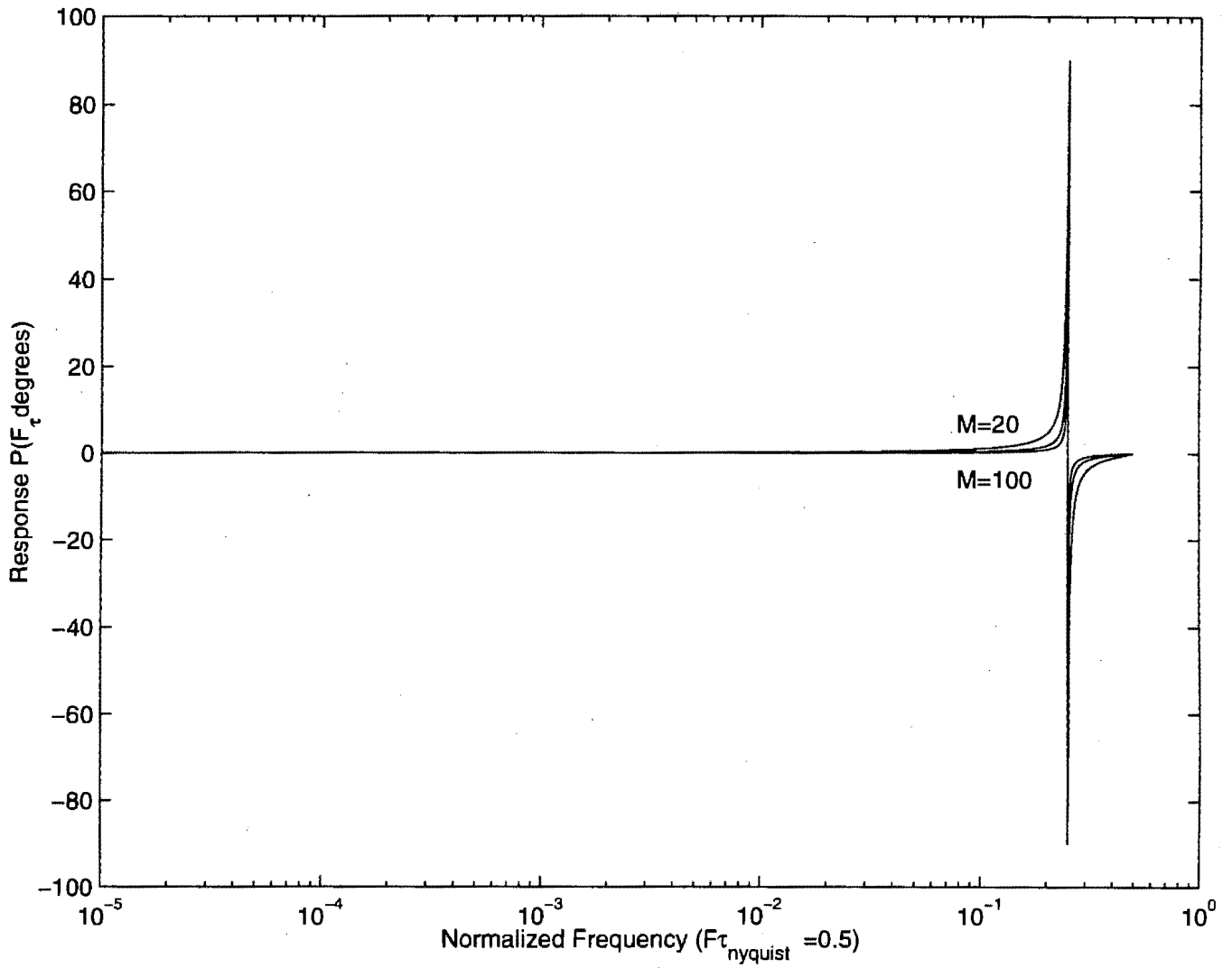


Figure 5.7: Simulated Analogue Phase Response of the Fading-Memory Polynomial Filter (Log Frequency)

## Chapter 6

# Implementation of Reference Free Correction Schemes

The infrared image footage analysed for the duration of this project was obtained by using the  $128 \times 128$  HgCdTe infrared camera system described in Section 3.2. The focal plane detector array of the camera system was cooled with liquid nitrogen in a dewar cooling housing. The camera was also fitted with a bandpass optical filter with a pass band in the  $3 - 5\mu\text{m}$  spectral region. The camera system was not fitted with any temperature references for nonuniformity compensation purposes. The uncompensated raw output imagery from the camera did exhibit spatial noise in the form of fixed pattern noise. The noise fingerprint appears as a form of haziness or cloudiness in the infrared scene. Pixels in the central regions of the image seem to have higher values compared to neighbouring pixels at the edges. It was also noticed that certain pixels do not vary in intensity as the scene changes due to camera panning. These pixels, whose values remained fixed, were treated as 'dead' pixels (i.e. their output response remains fixed even though the incident flux falling upon them changes).

### 6.1 Infrared Camera Data Storage on Video Cassette

The camera was operated during the day and at night with panning in horizontal and vertical directions. Footage, characterising the performance and response of the camera during both day and night operation, was obtained. This raw footage from the camera was recorded on VHS video cassette in CCIR format. The HgCdTe infrared camera did not support an interlaced analog output. In order to deal with the problems associated with interlacing, every two sequential frames from the camera were used. The first frame comprised of the odd field and the second frame comprised of the even field. Thus, line 1 from the first frame

became line 1 of the overall interlaced frame and line 1 from the second frame became line 2 of the interlaced frame. This arrangement allows for two subsequent infrared frames from the camera to be interlaced sequentially into the odd field and the even field respectively. However, this arrangement yields an overall image frame resolution of  $128 \times 256$ . In order to deal with this problem, each pixel in a horizontal line of the overall frame was repeated. Hence, the overall resolution of the final infrared image in a single video frame (made up of both odd and even fields) appears to be  $256 \times 256$ . As the overall resolution of the CCIR video format is  $768 \times 576$ , the infrared camera output occupies only a small portion of the entire video frame. Video footage from a normal Black and White optical camera was included in the unused portion of the video frame to help identify visually what the infrared camera was looking at. This Black and White optical camera was mounted on the same panning assembly and panned together with the infrared camera.

## 6.2 Convergence Criteria

As reference free correction schemes rely upon scene statistics for calibration, it was important to consider how many infrared image frames would be needed initially for adequate calibration of the detector array. This calibration would correct for response and offset nonuniformities as well as take care of fixed pattern and spatial noise. The number of frames needed for convergence in the calibration scheme may be determined by using a probabilistic convergence analysis where  $\bar{y}$  represents the estimates of a random variable  $y$ . In order to observe the distribution of estimations, let  $\bar{Y} = \bar{y}_1 + \bar{y}_2 + \dots + \bar{y}_n$ . According to the central limit theorem, the distribution of a random variable  $\bar{Y}$  can be approximated by a normal distribution if  $n$  is large enough. The estimates of the mean  $\mu_{\bar{y}}$  and variance  $\sigma_{\bar{y}}^2$  have the following relationships with the true mean  $\mu_y$  and variance  $\sigma_y^2$  [6].

$$\mu_{\bar{y}} = \mu_y \quad (6.1)$$

$$\sigma_{\bar{y}}^2 = \frac{\sigma_y^2}{n} \quad (6.2)$$

The variance in the mean and variance in the standard deviation are given by

$$\text{var}(\mu_{\bar{y}}) = \frac{\sigma_y^2}{n} \quad (6.3)$$

$$\text{var}(\sigma_y^2) = \frac{2\sigma_y^4}{n} \quad (6.4)$$

If 90 percent of estimations are to have an error within  $\pm\epsilon$ , then the relationship between  $\epsilon$  and the number of frames required  $n$  is found by using

$$\epsilon = \frac{1.64\sigma_y}{\sqrt{n}} \quad (6.5)$$

where  $\sigma_y$  may be assumed to be unity. Thus, 250 frames will be needed so that the error  $\epsilon$  may fall within 10 percent. As more frames are used in the continual re-calibration of the detector array, as presented in the Reference-Free Compensation scheme and Constant-Statistics algorithm, this error falls to lower values. After 500 frames, this error would be 7 percent, and after 750 frames, this error is 6 percent.

### 6.3 Obtaining the Infrared Sequences

It was important to use sequences that comprised of the different operating conditions of the camera, as well as panning of the camera in the horizontal and vertical directions. This helps illustrate variations in the performance of the camera with regard to fixed pattern spatial noise. Motion of the detector array, or camera panning is a key requirement in the implementation of reference free nonuniformity correction techniques. The use of different sequences allow for a comparison of the performance of reference free nonuniformity correction techniques for different input scenes under view. They also allow the user to obtain an estimate of the overall improvement in image quality that the correction technique presents over the uncompensated raw imagery. Hence, both day and night camera operating conditions were selected for this purpose. This was performed in order to see if there are any significant changes in the spatial noise of the detector array due to variations in background illuminosity, the panning motion of the camera, and environmental conditions.

Nonuniform cooling of the detector array, due to the uneven flow of liquid nitrogen over the array, may occur when the camera is suddenly jerked into a panning motion. This may give rise to spatial noise as individual detector spectral sensitivity is greatly dependent on operating temperature. Environmental conditions, including fluctuations in pressure and temperature, may result in inconsistent operating points in the detector cooling assembly. This, in turn, may result in changes in the temperature of the dewar cooling system leading to overall changes in of the spectral response of the detector array.

Five short video sequences, comprising of 500 frames each, and three longer ones, comprising of 900 frames each, were then digitally captured using a Matrox frame-grabber at the standard video rate in the AVI format. Only the infrared portion of the video data was captured. No compression of the video data was performed during the capturing process. The response from individual detector elements from the infrared detector array are displayed as pixels in a grabbed scene. Four of the shorter sequences and two of the longer ones comprised of the camera's performance during the day. One short sequence and one long sequence were of the camera's performance during the night.

### 6.4 Implementation of the Nonuniformity Correction Algorithms

These video sequences were analysed by algorithms implemented in Matlab. As Matlab is not able to read the AVI format, the video sequences were further converted to image sequences in the TIFF format, a format that Matlab is able to use. No compression was used during this conversion process. The algorithms in Matlab also accounted for the interlacing problem explained above. As the single infrared images in the sequences have a resolution of  $256 \times 256$ , this resolution was decreased to that of  $128 \times 128$  by a method of sub-sampling. In this method, each repeated pixel in the horizontal direction was removed and every alternate row was eliminated. Thus, only all of the odd fields were used. This allowed for an obtained infrared frame rate of 25 frames a second.

Three different algorithms were used including Narendra's original Reference-Free Compensation algorithm (Averaging) [21], Chiang's Constant-Statistics Algorithm (CS Averaging) [6], and the Fading-Memory Polynomial filter (Exp Window) with different exponential windows ( $M = 20, 50$  and  $100$ ). Both the Reference-Free Compensation and Constant-Statistics algorithms were developed to primarily remove fixed pattern and spatial noise as well as provide an overall uniform output picture with enhanced contrast by adjusting the responsivity of individual pixels in the grabbed sequences. The Fading-Memory Polynomial Filter was implemented to compensate for the effects of both fixed pattern and  $1/f$  noise. As all of these algorithms operate by processing individual image frames of a sequence in time, the word *iteration*, as used herein, is defined as the number of images of the sequence processed so far by the respective compensation algorithm. That is, the number of images used thus far out of the total number of images in the sequence. In the case of the Reference-Free compensation algorithm and the Constant-Statistics algorithm, the iteration number indicates the number of images out of the total number in the sequence that have been used to obtain the spatial noise statistics.

### 6.4.1 Reference-Free Nonuniformity Compensation Algorithm

As indicated in Section 5.2.1 the Reference-Free Compensation algorithm operates by evaluating the average value of an individual pixel's response as well as the pixel's standard deviation in time. An accurate representation of the fixed pattern noise, or noise fingerprint, may be obtained by averaging the input images over an adequate period of time as the camera is panned in the horizontal and vertical directions. As the initial assumption is that all of the individual detectors in the array are exposed to similar scene intensity statistics, the mean flux over a period of time incident on the array, as well as the standard deviation of the flux, should be the same for each pixel in the array. The Reference-Free Compensation scheme relates a single pixel's time averaged value to its dark current offset and the standard deviation of the pixel (over time) to the pixel's responsivity. These relations, in turn, correspond to the offset and responsivity of individual detector elements in the detector array. Thus, the response nonuniformities of individual detector elements in the array may be compensated for by obtaining the dark current offset and responsivity of individual detector elements through pixel statistics in the captured sequences. A linearised model may then be computed whereby the incident flux is directly proportional to pixel value in the captured infrared image.

If all individual detector elements were able to differentiate between 0–255 grey-scale intensity values, one would expect the mean value of flux intensity seen by each detector element after a period of time, if the camera is panned in the horizontal and vertical directions, to be about 128. Thus, any differences between the averaged pixel values (in time) obtained from a captured sequence and a uniform grey background (of value 128) is evidence of a noise fingerprint. One would expect the scene of time averaged pixel values to closely resemble to a uniform grey background. However, due to individual detector element dark current offset, differences in these time averaged pixel values exhibit the spatial noise fingerprint. This noise fingerprint or fixed pattern noise is extremely pronounced when the time average of the panned infrared scene is presented. Having obtained the spatial noise fingerprint  $\bar{Y}_i$ , individual detector element dark current offset  $O_i$  may be calculated by subtracting the time averaged image  $Y_i$  from a uniform grey background of value 128, as indicated below

$$O_i = \bar{Y}_i - 128 \quad (6.6)$$

This equation allows the pixels offsets to be centred about a mean of zero instead of 128 and is used to represent individual pixel offsets as the  $y$ -intercepts  $c$  in the straight line equation  $y = mx + c$ , where the desired pixel value  $x$  is related to the actual pixel value  $y$ . The gain coefficients  $m$  of the straight line equation are a result of the individual detector element responsivities. If the compensated output image is to have 256 grey levels, then it follows

#### 6.4. IMPLEMENTATION OF THE NONUNIFORMITY CORRECTION ALGORITHMS

that, in the ideal case,  $m$  should be approximately unity.

Having seen similar scenes, one would expect that the standard deviations of individual detector elements, about their average values (in time), to be almost equal. However, variations in the responsivities of individual detector elements lead to great differences in the standard deviations of these detector elements. Detector elements with low responsivities tend to have low standard deviations whereas detector elements with higher responsivities have higher standard deviations. By calculating the standard deviations of individual pixels (in time) in the captured sequences, these nonuniformities in the response of individual detector elements may be corrected for. This allows for a certain degree of contrast enhancement in the compensated image over the original raw image.

As implemented, the standard deviations of individual pixels in a grabbed sequence are evaluated in time. As the calculation of a time based standard deviation requires knowledge of every value encountered thus far, a simplified version of the standard deviation equation (given below) was used to prevent excessive data storage. This equation requires only current frame and the cumulative total of all of the previous frame values to calculate the standard deviation.

$$\sigma_{Y_i}(n) = \sqrt{\frac{1}{n-1} \left( \sum_{k=1}^n Y_i^2(k) - \frac{[\sum_{k=1}^n Y_i]^2}{n} \right)} \quad (6.7)$$

Examining all of the pixels in the image, the pixel with the largest standard deviation  $P_{StdDevMax}$  is selected. Being the largest standard deviation, this value indicates that this pixel has the greatest responsivity. As the other neighbouring pixels in the array have lower standard deviations, their individual responsivities may all be normalised to that of pixel  $P_{StdDevMax}$ .

As each individual pixel's standard deviation is a fraction of the value of  $P_{StdDevMax}$ , the required pixel normalisation coefficient will be given by

$$R_i = \frac{\sigma_{Y_i}}{\sigma_{Y_i}^{max}} \quad (6.8)$$

The use of the normalisation coefficient allows for greater pixel responsivity leading to a uniform output infrared picture wherein the contrast between individual pixels is well defined.

The Reference-Free Nonuniformity Compensation scheme was implemented by the following equation

$$X_i = \frac{Y_i - O_i}{R_i} \quad (6.9)$$

where  $X_i$  is a pixel in the output compensated image and  $Y_i$  is a pixel in the input image, obtained from the captured sequence. As the resultant  $X_i$  is zero mean with a unity variance (due to responsivity normalisation),  $X_i$  has to be offset by 128 in order to be displayed as a 256 level grey-scale image. Thus, the directly implemented algorithm was of the form given below

$$X_i = \left( \frac{Y_i - \bar{Y}_i}{\frac{\sigma_{Y_i}}{\sigma_{Y_i}^{max}}} \right) + 128 \quad (6.10)$$

#### 6.4.2 Constant-Statistics Algorithm

The implementation of the Constant-Statistics algorithm was similar to that of the Reference-Free Compensation algorithm described above. The only difference between the two is the use of the  $L_1$  norm definition of standard deviation in the Constant-Statistics algorithm instead of the usual  $L_2$  norm definition used in the Reference-Free Compensation algorithm. Chiang did state that the  $L_1$  norm gives similar performance compared to  $L_2$  norm [6]. However, he did not test this algorithm with actual infrared footage. Instead, he used simulated fixed pattern and white Gaussian noise to characterise the performance of his modification to the Reference-Free Compensation algorithm.

The Constant-Statistics algorithm was also implemented using recursive equations allowing for computational saving. By using these recursive versions only four multiplications/divisions and four additions/subtractions are required per step. This prevents the need for excessive system memory. It is important to note that when no portion  $P$  of standard deviation is used the Constant-Statistics algorithm reduces to the Reference-Free Compensation scheme.

#### 6.4.3 Fading-Memory Polynomial Filters

Fading-Memory Polynomial filters were implemented with exponential windows of length  $M = 20, 50$  and  $100$ . These filters were initialised by calculating the average of a number input images in equally weighted windows of the respective lengths in a manner similar to that described in Section 5.2.3. Recursive algorithms were used in the implementation of these filters for purposes of computational saving. The standard deviation used in these filters uses the  $L_1$  norm and not the  $L_2$  norm.

## 6.5 Dead Pixel Correction

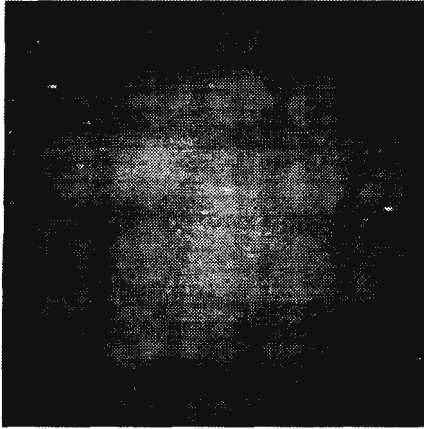
As mentioned earlier it was also noticed that certain pixels in the captured infrared sequences did not vary in intensity as the scene changes due to camera panning. These pixels are due to damaged individual detector elements whose output response remains the same even though the incident light falling upon them changes. As these pixel values remained fixed, they were treated as 'dead' pixels. Some of these pixels were fairly bright, having intensity values close to 255, whereas some of them appeared grey and were only noticed during the panning motion of the camera. The brighter white pixels are particularly problematic as they can be misinterpreted as infrared point source targets if the camera is not panned.

As these pixel values display a similar intensity value over time, the methods presented above in all three algorithms work well to remove them. These pixel values, despite remaining more or less fixed, do change slightly due to temporal noise mechanisms. By averaging in time, these pixel values form a part of the overall spatial noise fingerprint and are removed by the compensation algorithms above. However, these pixel values are replaced by a pixel intensity of 128 as a result of the offset correction indicated in Eq. 6.10. The overall output image  $X_i$  in all algorithms is zero mean and needs to be offset by 128 in order to be displayed as a 256 level grey-scale image.

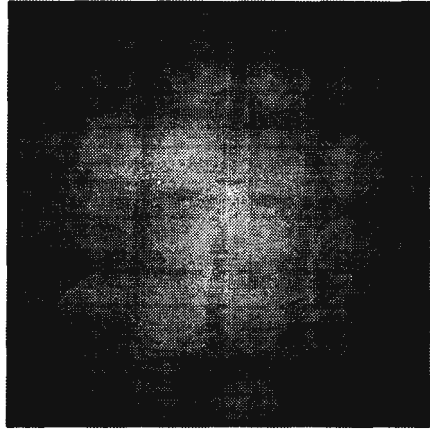
The replacement of dead pixels by pixels of value 128 is an unsatisfactory solution as these pixels have a constant intensity just like before. As these dead pixels have been observed to be single pixels with active neighbours around them, a more satisfactory solution would be to replace these pixels with average of all of its neighbours. As all pixels (except those at the edges) have eight direct neighbours, the average value of a pixels eight neighbours may be used to replace it. This method allows for a more continuous approximation of the pixel's value leading to an overall improved image free of dead pixel defects. For pixels at the edges, it was decided to fold the image over in the horizontal and vertical directions. This may be visualised as rolling a piece of paper so that the top meets the bottom, or the right meets the left. Hence, the bottom row of pixels in the image is mapped above the top row and vice versa. Similarly, the right column of pixels is mapped to the left of the left column and vice versa.

Initially, it was decided to investigate the standard deviations of these dead pixels in order to characterise them and obtain a constellation diagram (a diagram indicating the positions of dead pixels). As these pixels have fairly constant values over the entire sequence, their respective standard deviations in time were expected to be low. However, due to temporal noise mechanisms, some of these pixels did display greater standard deviations than expected. Some pixels with low responsivities in the middle of the image were also falsely classified as

dead pixels. Hence, this method of using the standard deviation was abandoned and an alternative sought.



(a) Time Averaged Image



(b) Low Passed Version of Time Averaged Image



(c) Constellation Diagram - Map of Dead Pixels

Figure 6.1: Constellation Diagram indicating the Location of Dead Pixels

Thereafter, a method using the averaged or low passed version of the spatial noise fingerprint (i.e. low passed version of time averaged input image) was implemented. In the spatial noise fingerprint, obtained from averaging the input images in time, the dead pixels appear as distinct points. By convolving this spatial noise fingerprint with a  $3 \times 3$  convolution mask a slightly blurred image may be obtained. In this resultant low passed image, the individual point positions of the dead pixel elements are not easily discernible. By subtracting the low passed image from the spatial noise fingerprint these pixel positions can be determined. Pixel difference thresholding can then be applied to this resultant image to obtain the positions to

a greater degree of certainty. This thresholding was performed with pixels of intensity greater than 6 or less than 6 selected as dead pixels. The constellation diagram, or map of these dead pixels, is shown in Fig. 6.1. In this figure the time averaged input image and a low passed version of this image are also indicated.

## 6.6 Varying the Portions of Standard Deviation Used

As shown above in Section 6.4.1, an indication of the responsivity of each detector element may be given by the standard deviation experienced by each pixel. In order to obtain an output wherein the pixel intensity values lie between the range 0 – 255, all of the algorithms were implemented using a normalisation factor  $R_i$ . This normalisation factor allows for the standard deviations of individual pixels to be normalised to the maximum standard deviation experienced by a pixel in the frame. However, as all of the tested sequences were of different scenes with different scene intensity statistics, it is possible that not all pixels were able to see the extremes of high and low levels of incident flux. By examining the standard deviations of five randomly selected pixels, it is noted that the standard deviation for each pixel changes as different sequences are used. Table 6.1 presents the pixel standard deviation at the end of the sequence as well as the maximum standard deviation obtained in the sequence. The five randomly selected pixels were at positions (25,79),(64,18),(36,94),(21,84) and (59,122) within the image frame. Both the short sequences (S. Seq) and long sequences (L. Seq) were used obtain the standard deviations.

Table 6.1: Standard Deviations of Pixels in Infrared Sequences

Sequence Used	Standard Deviation in Intensity of Pixels					
	Point 1	Point 2	Point 3	Point 4	Point 5	MaxStdDev
S. Seq 1 (Day)	10.5908	12.3367	13.2826	10.1447	4.5426	22.3686
S. Seq 2 (Day)	11.0814	11.1439	11.0331	10.4007	5.8599	17.5970
S. Seq 3 (Day)	8.0657	7.0228	10.2076	8.2061	20.0571	25.6797
S. Seq 4 (Day)	5.2480	4.9805	6.8721	5.7981	14.0848	33.5035
S. Seq 5 (Night)	17.7433	26.2046	24.3435	19.7059	24.1110	42.8612
L. Seq 1 (Day)	10.1098	10.9600	11.8331	10.1351	5.6391	19.0672
L. Seq 2 (Day)	6.6171	7.1879	8.8538	7.0792	17.6400	32.9547
L. Seq 3 (Night)	18.3788	21.3164	24.4528	19.5853	26.4023	37.6421

In order to deal with this problem, it was decided to vary the amounts of overall standard deviation used. Hence, all of the reference free nonuniformity compensation algorithms were altered to use only portions  $P$  of the total normalised standard deviation experienced by a pixel. As  $R_i$  was previously shown to be equal to  $\sigma_{Y_i}/\sigma_{Y_i}^{max}$ , the equation below was

substituted for  $R_i$ ,

$$R_i = (1 - P) + P \frac{\sigma_{Y_i}}{\sigma_{Y_i}^{max}} \quad (6.11)$$

where  $P$  was varied between 0 and 0.9 and  $\sigma_{Y_i}^{max}$  is the maximum standard deviation of any pixel in the image sequence in time. Variations in the value of  $P$  allow for controlled contrast enhancement. When  $P$  is increased, the gain or responsivity of each pixel increases. This allows pixels to have a greater output range of display leading to an image with much more contrast between individual pixels. Thus, a low value of  $P$  corresponds to little contrast enhancement whereas a higher value leads to much greater contrast between pixels in the infrared image.

## 6.7 Signal to Noise Ratio Determination

### 6.7.1 Signal to Noise Ratio Determination from Image Averaging

Fixed pattern noise and  $1/f$  noise are presented as types of spatial noise and, due to the low frequency components in  $1/f$  noise, may be slow varying. The algorithms presented above have been created to remove spatial noise. However, it is difficult to determine how well the algorithm performs as the primary noise mechanisms in the infrared sequences are of a spatial nature and not of a temporal nature. Although temporal noise may be accurately measured, and thus predicted, by examining the changes in individual pixels when the same scene is under view (no motion in the scene or due to the panning assembly), spatial noise is much more pronounced during the presence of scene movement or movement of the panning assembly. It is noticed that pixels in certain regions have higher or lower values (offsets) than neighbouring regions.

It is also inherently more difficult to measure and quantify spatial noise as a true or pure representation of the input signal or infrared scene is needed. Obtaining a proper input signal often requires a perfectly calibrated infrared camera. The output from a camera troubled by spatial noise may then be compared to a well calibrated camera and the the difference in the peak Signal-to-Noise ratio (PSNR) may be calculated. Unfortunately, no such camera was available for use and a pure reference image sequence was not obtained. Techniques to work around this setback were considered and are discussed below. These techniques were used to obtain a figure of merit in order to determine how well the various compensation algorithms performed overall.

As mentioned previously, in reference free nonuniform correction techniques, an accurate representation of the fixed pattern noise, or noise fingerprint, may be obtained by averaging the input images over an adequate period of time as the camera is panned in the horizontal and vertical directions. As the assumption is that all of the individual detectors in the array are exposed to the scene intensity statistics, the average flux over a period of time incident on the array, as well as the standard deviation of this flux, should be the same for each pixel in the array.

If individual detector elements were able to differentiate between 0 – 255 grey-scale intensity values, one would expect the mean value to be about 128. An ideal detector, free of spatial noise, would yield a uniform grey averaged output picture (of intensity approximately 128) if properly averaged over time. Thus, in the case of a non-ideal detector troubled by fixed pattern noise, the differences between the time averaged input image and a uniform grey background (of value 128) is evidence of a noise fingerprint. The mean value of the square of these differences  $N_{Input}$  may be used to compute the Input PSNR as given below

$$PSNR_{Input}(dB) = 20 \log \frac{256^2}{N_{Input}^2} \quad (6.12)$$

After the image is compensated using the correction algorithm, the output images may be averaged in time in a similar manner to that used for the input images. Thus, the time averaged output image may be calculated to see how closely it resembles a uniform grey background of intensity 128. The compensation algorithm, in removing fixed pattern noise, should allow the time averaged output image to approximate a uniform grey background. Any deviations from this uniform grey background indicates that the output image still has some noise associated with it. Once again the mean value of the square of the differences between the uniform grey background and individual pixel values may be computed, yielding the mean output noise  $N_{Output}$ . The Output PSNR may be computed by

$$PSNR_{Output}(dB) = 20 \log \frac{256^2}{N_{Output}^2} \quad (6.13)$$

The improvement in the image may be evaluated by establishing the differences in the peak Signal-to-Noise Ratios, as given below

$$PSNR_{Improvement}(dB) = PSNR_{Output}(dB) - PSNR_{Input}(dB) \quad (6.14)$$

However, the validity of using all of the time averaged output image frame was questioned as

most of the captured sequences displayed greater horizontal panning than vertical panning. It was also noticed that the time averaged output image exhibited slight streaking in the horizontal directions. Figure 6.2 illustrates these streaking artifacts.



Figure 6.2: Streaking Artifacts in Time Averaged Output Image

In order to investigate whether the direction of panning influences the output peak Signal-to-Noise ratios, it was decided to separately obtain the peak Signal-to-Noise ratios in a horizontal band across the middle of the time averaged output image as well as a vertical band running down the middle of the image. As the image resolution was  $128 \times 128$ , the dimensions of this band in the horizontal direction was  $128 \times 32$ . In the vertical direction it was  $32 \times 128$ . The output peak Signal-to-Noise ratios of the compensated images were obtained only within these bands. In keeping with the calculated convergence criterion, the peak Signal-to-Noise ratios were calculated when the frame number exceeded 250 in the sequences. The portion  $P$  of standard deviation used was 0.50.

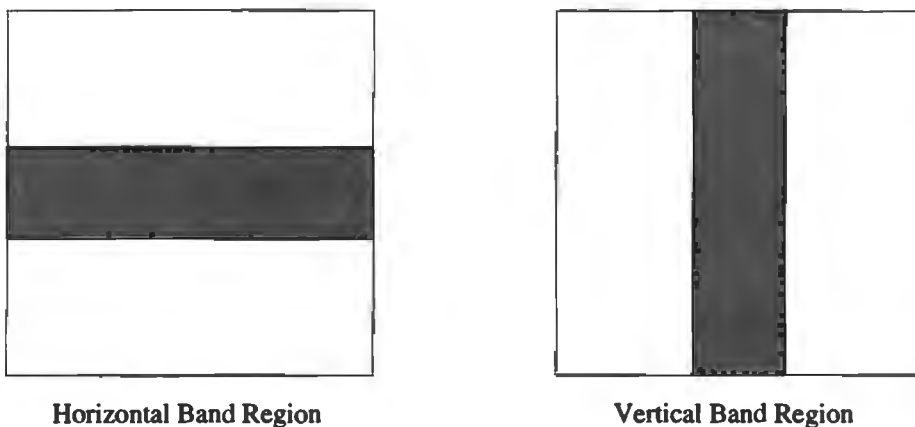


Figure 6.3: Horizontal and Vertical Band Regions

## 6.7. SIGNAL TO NOISE RATIO DETERMINATION

Graphs illustrating the peak Signal-to-Noise ratio in the output image using the total output image frame as well as horizontal and vertical band region characterisation for the different sequences are presented in Appendix F. The results of these peak Signal-to-Noise ratios (in *dB*) as well as the differences between using the total output image and respective band regions are presented in Table 6.2.

Table 6.2: Peak Signal to Noise Ratio of Output Image Sequences Using Total Output Image and Band Regions

Sequence Used	Signal to Noise Ratio of Output Image				
	Total Output	Band Regions		Differences	
		Vertical	Horizontal	Vert-Total	Horz-Total
S. Seq 1 (Day)	34.8682	34.3110	35.8342	-0.5571	0.9660
S. Seq 2 (Day)	30.6563	30.5365	32.5164	-0.1197	1.8601
S. Seq 3 (Day)	31.1630	30.7410	35.1308	-0.4220	3.9678
S. Seq 4 (Day)	34.8128	34.8137	35.6733	0.0009	0.8605
S. Seq 5 (Night)	26.1593	25.7308	24.8819	-0.4285	-1.2774
L. Seq 1 (Day)	35.0531	34.2875	38.7662	-0.7656	3.7131
L. Seq 2 (Day)	30.7164	30.3703	34.9459	-0.3460	4.2295
L. Seq 3 (Night)	30.7052	30.4646	32.8825	-0.2406	2.1773

It was discovered that the PSNR of the output image obtained using the horizontal band is not the same as that obtained using the vertical band. After approximately 250 frames, the PSNR for the output image calculated using the vertical band region is significantly lower than that using the horizontal band region. It is also noticed that the PSNR ratio obtained using the entire output frame closely follows that of using the vertical band region. Although the total output frame PSNR curve follows the vertical band PSNR curve in all of the graphs, the PSNR curve for the total output frame is slightly greater than the vertical band PSNR curve. This was observed in seven out of the eight sequences. The maximum average difference obtained between the both of them was only 0.77 decibels. As this difference is small, and both the peak Signal-to-Noise ratios obtained using total output image frame and vertical band region are greatly smaller than that using the horizontal band region, it was decided that it would be appropriate to use the entire output image frame for the characterisation of output image peak Signal-to-Noise ratio. This allows for the calculation of a worst case improvement in the output image compared to the input image in terms of overall peak Signal-to-Noise ratio. Therefore, the method of using the entire time averaged output image frame was selected for use in order to characterise the improvement in the output image in terms of peak Signal-to-Noise ratio.

### 6.7.2 Validity of Signal to Noise Ratio Evaluation Using Time Averaged Output and Input Images

As the method presented above is not a pure measure of the Peak Signal-to-Noise ratio, experimental verification concerning the validity of this averaging method was needed. In order to achieve this purpose, it was decided to impose a spatial fingerprint on a normal video sequence as it was not possible to obtain a perfectly calibrated infrared sequence. The compensation algorithm could then be applied to the video sequence to correct for spatial noise effects due to the imposed fingerprint. The true uncorrupted video sequence would thus allow for an overall evaluation of the compensation process in terms of true peak Signal-to-Noise ratio improvement. As the initial amount of added spatial noise is known, the level of spatial noise remaining in the output signal may be compared to this initial added amount of spatial noise to obtain the peak Signal-to-Noise ratio improvement.

Once again, the output peak Signal-to-Noise ratio is given by

$$PSNR_{Output}(dB) = 20 \log \frac{256^2}{N_{Output}^2} \quad (6.15)$$

and the input peak Signal-to-Noise ratio is given by

$$PSNR_{Input}(dB) = 20 \log \frac{256^2}{N_{Input}^2} \quad (6.16)$$

Hence, the overall improvement in the image due to the correction algorithm would be given by evaluating the differences in the Signal-to-Noise ratios

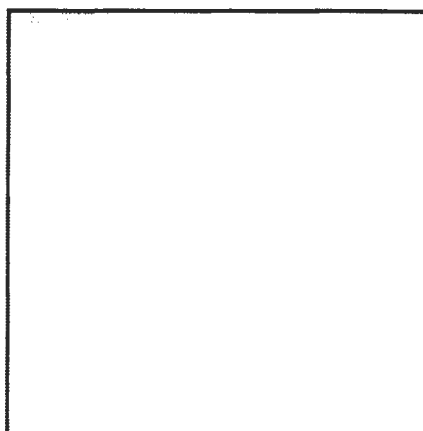
$$PSNR_{Improvement}(dB) = PSNR_{Output}(dB) - PSNR_{Input}(dB) \quad (6.17)$$

Using a normal video camera, a sequence of approximately 500 frames was captured. The camera was panned in both the horizontal and vertical directions during the capturing process. The time average of the captured video sequence, indicated in Fig. 6.4(a), was evaluated in order to see how well the panning process performed in illuminating neighbouring pixels in the video Charge-Coupled-Device (CCD) with similar incident flux levels. If the video camera had any fixed pattern noise associated with it, time averaging the images in the video sequence would also make this noise fingerprint more visible. The standard deviation of all the pixel elements in the video CCD, shown in Fig. 6.4(b), was also calculated to determine if all of them have similar responsivities. The mean value of the time averaged image was 139.24 with

a standard deviation about this mean of 0.6658 across the image. This mean value was higher than the expected 128, and is attributed to the camera aperture being opened to a slightly greater extent. The low standard deviation of the mean across the image (approximately about a single intensity level out of 256) indicates that all of the pixels in this video CCD have a fairly uniform offset.



(a) Time Averaged Video Image



(b) Scaled Standard Deviation of Pixels in Video Sequence

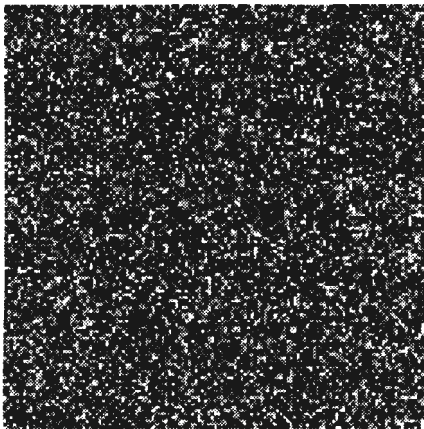
Figure 6.4: Time Average and Standard Deviation of Pixels in the Uncorrupted Video Sequence

The mean value of the standard deviation of all of the pixels in the video CCD images was 150.70 and the standard deviation about this mean standard deviation was 0.7168. The mean value of standard deviation was high indicating good responsivity. The standard deviation about the mean of the standard deviation image is also low. This indicates that the responsivities of all pixels in the CCD are fairly uniform.

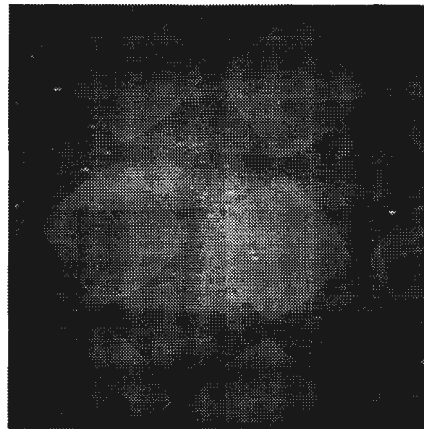
As both the responsivity and offsets for all elements in the detector are uniform, the video CCD detector does not appear to be troubled by spatial fixed pattern noise. This also indicates that the captured sequence was well panned in both the horizontal and vertical directions.

Two spatial noise fingerprints, shown in Fig. 6.5(a) and Fig. 6.5(b) were selected for use as the test pattern noise. The first one, *FP1*, was an image wherein the pixel intensities were selected at random. The second, *FP2*, was the time average of the images in Long Night infrared sequence (spatial noise fingerprint of the Long Night sequence).

Both these test fixed pattern noise images had a resolution of  $128 \times 128$  and were 256 grey-scale images. These spatial noise fingerprints *FP* were added to original images *V* of the normal video sequence in the following manner:



(a) Noise Fingerprint1



(b) Noise Fingerprint 2

Figure 6.5: Noise Fingerprints used as Fixed Pattern Noise

$$Y_i = V_i + 0.5(FP_i) \quad (6.18)$$

$Y_i$  in the above equation represents a single pixel in the spatial noise corrupted image. Only a half of the intensity of the noise fingerprint was added to reference video image (addition on a per pixel basis). With spatial added noise, the corrupted image was quantised to fit into the grey-scale range between 0 to 255 by setting values below 0 to 0 and above 255 to 255. As the responsivities of individual pixels in the original video CCD images were shown to be nearly uniform, no gain or standard deviation normalisation is needed to correct for detector responsivity variation. Only offset correction is required to compensate for the added fixed pattern noise.

The Reference-Free Compensation algorithm was then implemented on the spatial noise corrupted video sequence to correct for pixel offsets. The results of the correction algorithm are illustrated on the next page. Figure 6.6(a) is an original image frame from the video sequence. The image with added fixed pattern noise, corrupted by noise fingerprint  $FP1$ , is presented in Fig. 6.6(b). The noise compensated output image using the statistics of 500 previous images is presented in Fig. 6.6(c).

By averaging the input images of the video sequence in time, a time averaged input image (Fig. 6.6(e)) is obtained. This time averaged input image resembles the added fixed pattern noise fingerprint  $FP1$ , shown in Fig. 6.5(a). Similarly, the time averaged output image of the compensated sequence is also indicated in Fig. 6.6(f). This time averaged output image is much more uniform than the time averaged input sequence and may be compared to the

time averaged image of uncorrupted sequence that appears in Fig. 6.4(a).

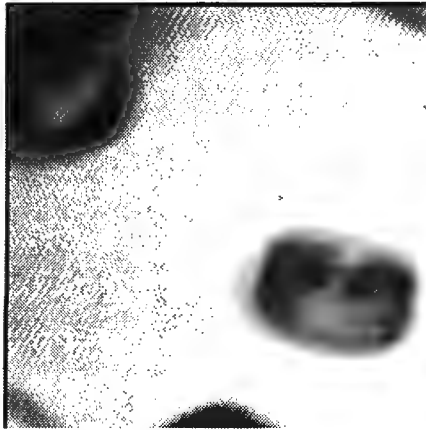
Table 6.3 indicates the performance in peak Signal-to-Noise ratio improvement (in *dB*) evaluated using the true signal reference (True) as well as using the time averaged input and output image method (Avg) presented above. Both the mean improvements in PSNR using the different fingerprints as well as the standard deviation about these mean improvements are tabulated.

Table 6.3: True PSNR Improvement compared to PSNR improvement obtained by Time Averaging Input and Output Images

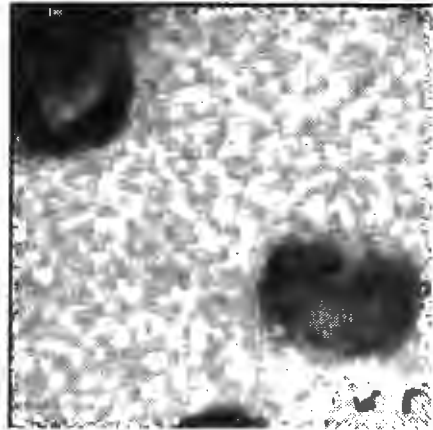
Fingerprint Used	True Mean Impr	Avg Mean Impr	True StdDev	Avg StdDev
Fingerprint 1	8.9112	4.9965	1.3166	1.6845
Fingerprint 2	7.8779	7.5655	1.3377	1.7041

Figure 6.7 shows the performance of the Reference-Free Compensation technique in compensating for Noise fingerprint 1. The True Output PSNR and True Input PSNR as well as the Output PSNR and Input PSNR obtained by time averaging input and output images are presented. Note, the mean True PSNR improvement in Table 6.3 above was evaluated by calculating the mean of the difference between True Output PSNR and True Input PSNR. The mean PSNR improvement using the time averaged output and input images was worked out using the mean of the difference between Output PSNR and Input PSNR.

As stated earlier, the main motivation for obtaining this comparison was to see how well the characterisation of PSNR improvement using the time averaged input and output images compares to the true PSNR improvement implemented by the Reference-Free Compensation process. In both cases, the true PSNR improvement was higher than that given by using the time averaged images. The standard deviation of these improvements is also lower for the true PSNR evaluation compared to the time averaged image PSNR evaluation. Thus, it may be said that the true PSNR improvement in the output image compared to the input image, is much better than the improvement predicted by the method of obtaining time averaged input and output images. The method of using time averaged images in the evaluation of peak Signal-to-Noise ratio improvement serves to indicate an overall worst case improvement in spatial fixed pattern noise compensation of the output image compared to the input image.



(a) Original Video Image



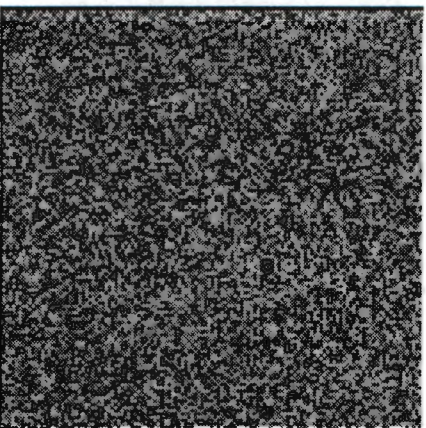
(b) Spatial Noise Corrupted Input Image



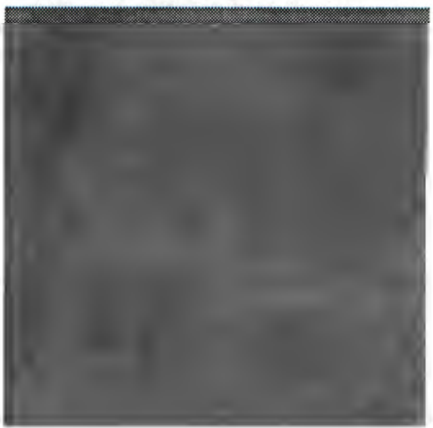
(c) Compensated Output Image



(d) Scaled Standard Deviation of Pixels in Corrupted Sequence



(e) Time Averaged Input Sequence



(f) Time Averaged Output Sequence

Figure 6.6: Performance of the Reference-Free Compensation Algorithm

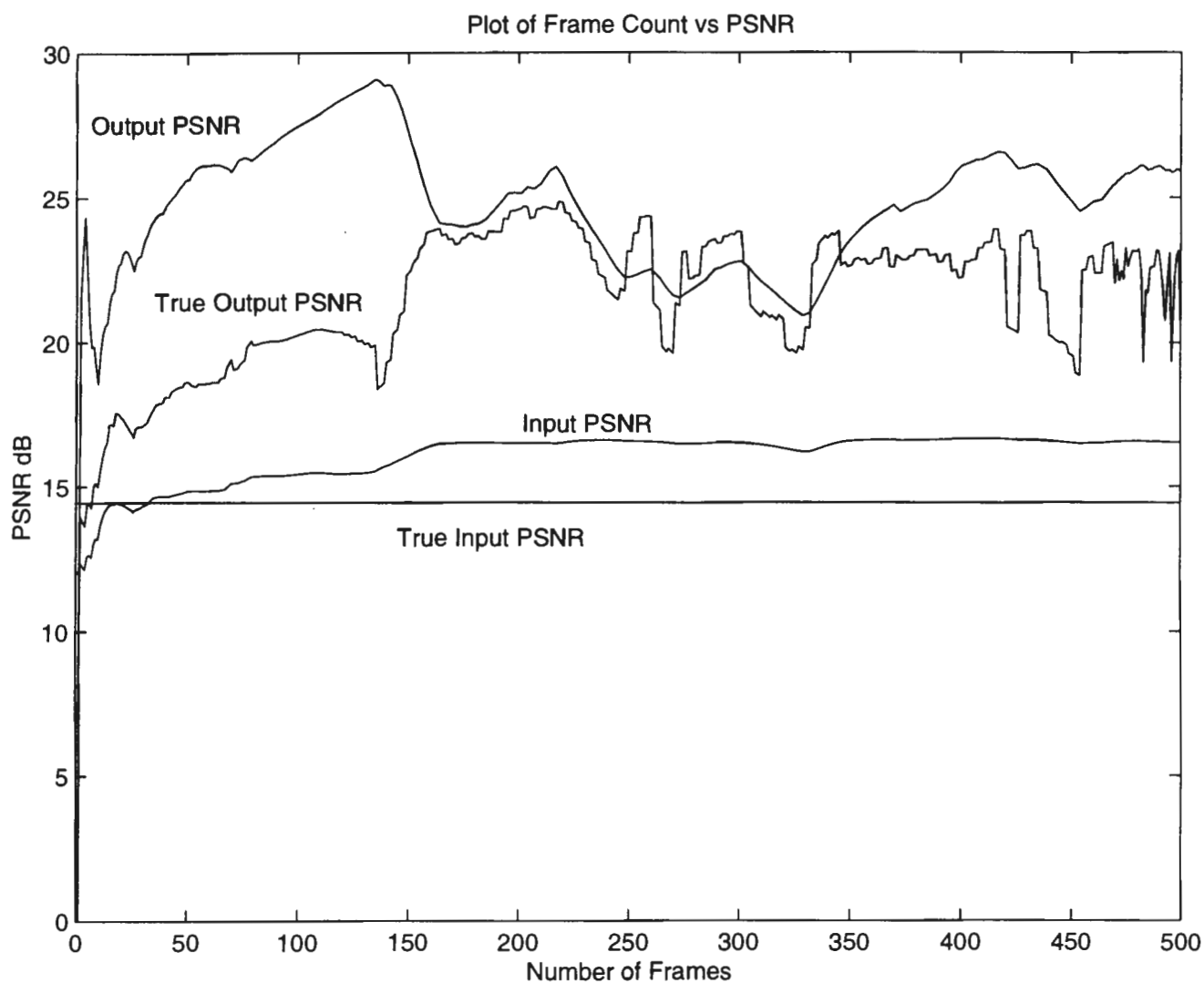


Figure 6.7: True Input and True Output Image PSNR compared to Time Averaged Input and Output PSNR when Noise Fingerprint 1 is used

# Chapter 7

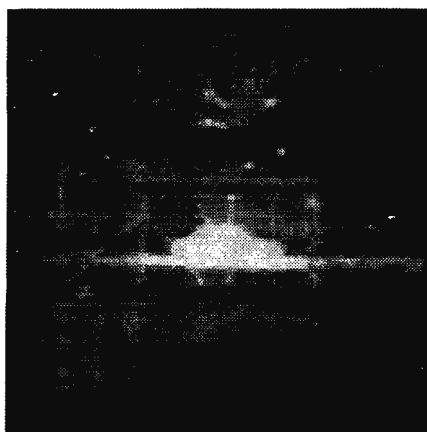
## Results

This chapter contains a summary of the results obtained using the reference free nonuniformity correction algorithms on the infrared image sequences. Five short image sequences, of 500 frames each, and three longer image sequences, of 900 frames each, were used as test data. Of the five short image sequences, four were day sequences and one was a night sequence. In the three long sequences, two were day sequences and one was a night sequence.

The performances of the Reference-Free Compensation scheme, the Constant-Statistics Algorithm and Fading-Memory Polynomial filters were evaluated with varying portions  $P$  of pixel standard deviation being used. These portions  $P$  included 0.00, 0.25, 0.50, 0.75 and 0.90. The mean improvements in the peak Signal-to-Noise ratio, as well as the standard deviation of these improvements were calculated for the eight sequences. In keeping with the calculated convergence criteria, the mean improvement was only evaluated once the frame number in the sequence under test exceeded 250. Thus, an allowance is made for convergence through proper averaging (in both the Reference-Free Compensation and Constant-Statistics algorithms) and exponential window operations (in the case of the Fading-Memory polynomial filters).

The visible performance of Reference-Free Correction scheme for the long night sequence is shown in Fig. 7.1(a) through Fig. 7.1(f). Here the same frame is repeated after 10, 50, 100, 500 and 900 iterations to illustrate the extent of the nonuniformity compensation process. The portion  $P$  of standard deviation used in the implementation of this algorithm for this particular sequence was 0.5. The time averaged input image (fixed pattern noise fingerprint) as well as a scaled standard deviation of the pixels obtained at the end of the sequence are also illustrated in Fig. 7.2(a) and Fig. 7.2(b).

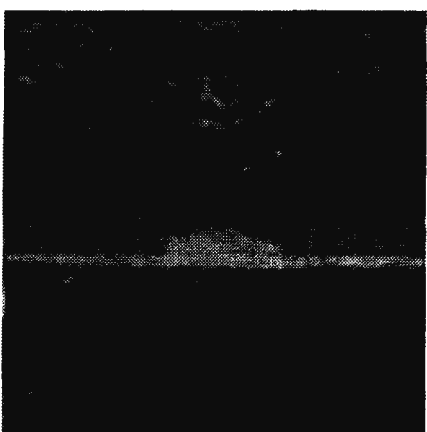
The variation in time of the output peak Signal-to-Noise ratio for the long night sequence is highlighted in Fig. 7.3. The peak Signal-to-Noise ratios for the different portions of standard



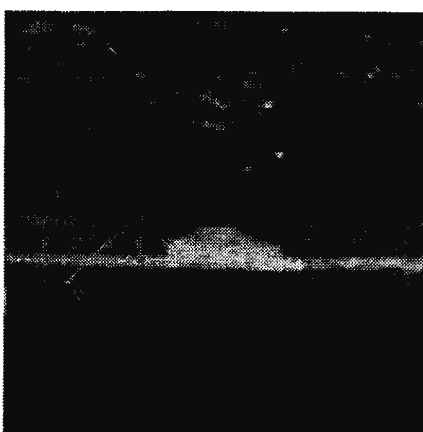
(a) Original Picture



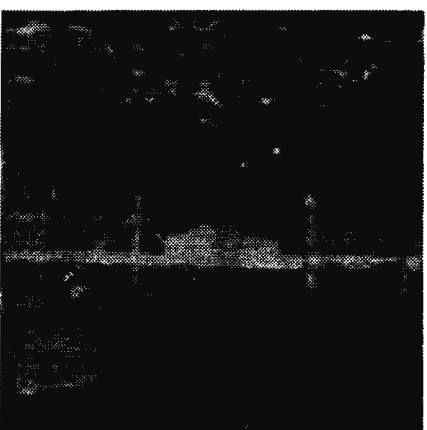
(b) Output Image after 10 iterations



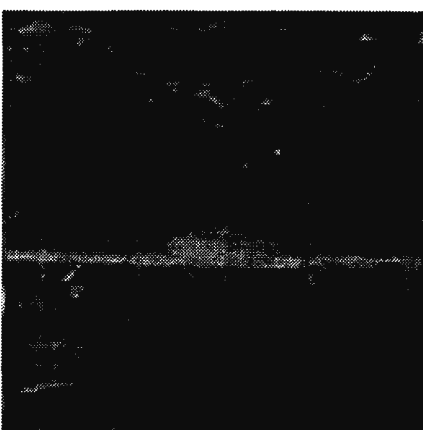
(c) Output Image after 50 Iterations



(d) Output Image after 100 Iterations



(e) Output Image after 500 Iterations



(f) Output Image after 900 Iterations

Figure 7.1: Performance of the Reference-Free Compensation Algorithm over time

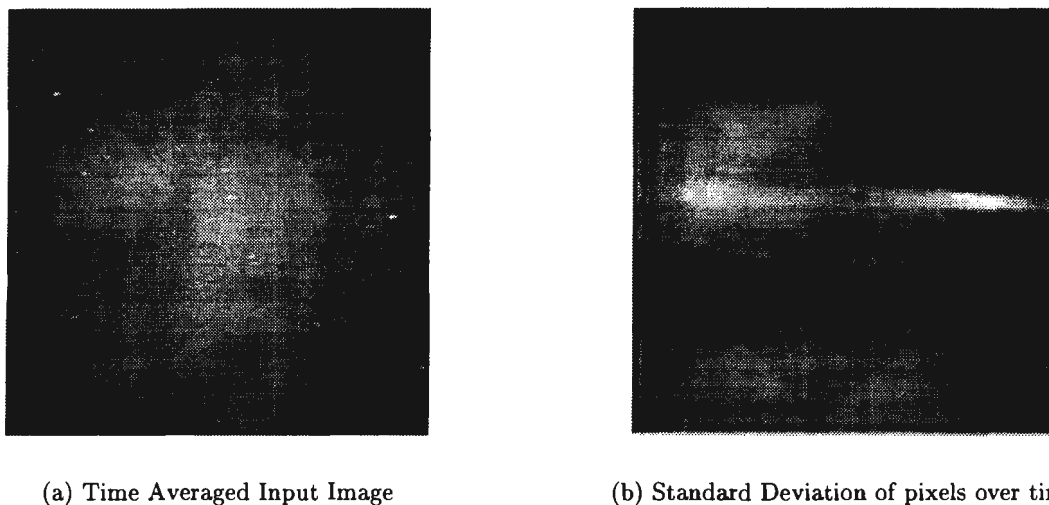


Figure 7.2: Image Statistics obtained during the use of the Reference-Free Compensation Algorithm

deviation used as well as the input image peak Signal-to-Noise ratio are plotted. The number of elapsed frames, corresponding to time, appears on the  $x$ -axis.

Further graphs indicating the performance of both short and long sequences in terms of input and output peak Signal-to-Noise ratio appear in Appendices A through to E.

## 7.1 Results of Short Sequence Analysis

The results obtained testing the five short sequences are presented here. The correction algorithms used were Reference-Free Compensation scheme, the Constant-Statistics algorithm and Fading-Memory Polynomial filters with exponential window sizes of 20, 50 and 100. The mean improvement for each individual sequence as well as the the standard deviation of this improvement are tabulated. The overall mean improvements ( $\overline{M}$ ) considering all sequences, as well as the standard deviation associated with this overall mean ( $\sigma_{\overline{M}}$ ) improvements, are also indicated.

The tables also contain the overall mean of individual sequence standard deviation ( $\overline{\sigma}$ ). The standard deviations of this overall mean of sequence standard deviation ( $\sigma_{\overline{\sigma}}$ ) are presented in the tables as well.

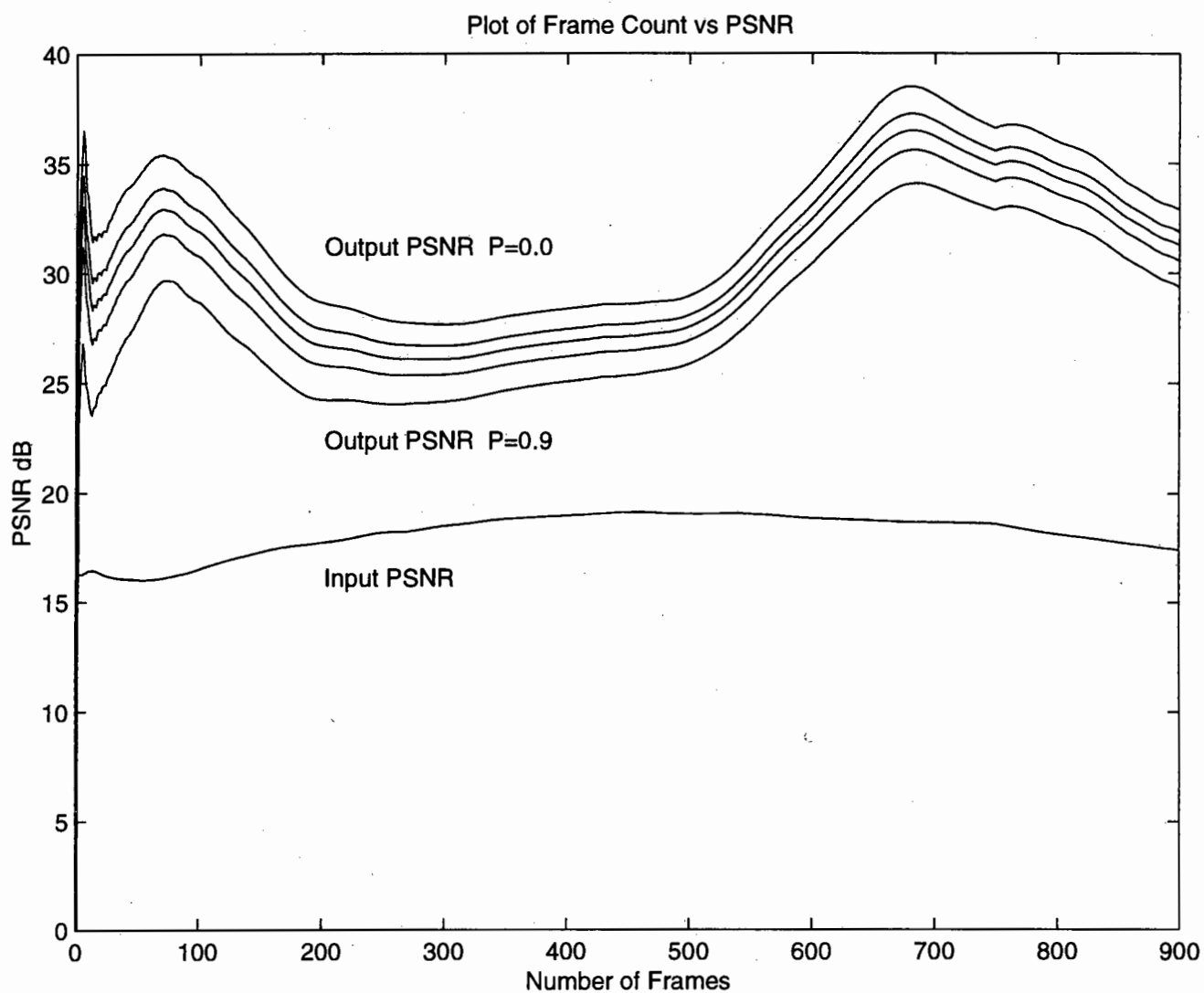


Figure 7.3: Input and Output Image PSNR for Long Night Sequence when the Reference-Free Compensation Algorithm is used.

### 7.1.1 Performance of the Reference-Free Compensation Algorithm

Table 7.1 indicates the mean improvements in peak Signal-to-Noise ratio (in  $dB$ ) of the output image compared to the input image for the short image sequences when the Reference-Free Compensation algorithm was used.

### 7.1.2 Performance of the Constant-Statistics Compensation Algorithm

The mean improvements in peak Signal-to-Noise ratio (in  $dB$ ) of the output image compared to the input image for the short image sequences when the Constant-Statistics Compensation algorithm was used is given in Table 7.2.

### 7.1.3 Performance of the Fading-Memory Polynomial Filters

Tables 7.3, 7.4 and 7.5 present the improvements in peak Signal-to-Noise ratio (in  $dB$ ) of the output image compared to the input image when Fading-Memory Polynomial filters were implemented on the short sequences. Exponential window sizes of 20, 50 and 100 were used.

## 7.2 Results of Long Sequence Analysis

Results gathered during the evaluation of the three long sequences appear here. The correction algorithms implemented were the Reference-Free Compensation scheme, the Constant-Statistics algorithm and Fading-Memory Polynomial filters with exponential window sizes of 20, 50 and 100. The mean improvement for each individual sequence as well as the standard deviation of this improvement are tabulated. The overall mean improvements ( $\overline{M}$ ) considering all sequences, as well as the standard deviation associated with this overall mean ( $\sigma_{\overline{M}}$ ) improvements, are also indicated.

The tables also contain the overall mean of individual sequence standard deviation ( $\overline{\sigma}$ ). The standard deviations of this overall mean of sequence standard deviation ( $\sigma_{\overline{\sigma}}$ ) are presented in the tables as well.

### 7.2.1 Performance of the Reference-Free Compensation Algorithm

Table 7.6 indicates the mean improvements in peak Signal-to-Noise ratio (in  $dB$ ) of the output image compared to the input image for the long image sequences when the Reference-Free

Compensation algorithm was used.

### 7.2.2 Performance of the Constant-Statistics Compensation Algorithm

The mean improvements in peak Signal-to-Noise ratio (in  $dB$ ) of the output image compared to the input image for the long image sequences when the Constant-Statistics Compensation algorithm was used is presented in Table 7.7.

### 7.2.3 Performance of the Fading-Memory Polynomial Filters

Tables 7.8, 7.9 and 7.10 present the improvements in peak Signal-to-Noise ratio (in  $dB$ ) of the output image compared to the input image when Fading-Memory Polynomial filters were implemented on the long sequences. Exponential window sizes of 20, 50 and 100 were used.

Table 7.1: PSNR Improvement in the Short Sequences using the Reference-Free Compensation Algorithm

Short Sequence Used		Portion of Standard Deviation Used				
		0.00	0.33	0.50	0.67	0.90
S. Sequence 1 (Day)	Mean	14.4846	12.2755	10.8256	9.0162	5.4148
	StdDev	1.5848	1.5426	1.5050	1.4448	1.2670
S. Sequence 2 (Day)	Mean	9.0060	7.4729	6.5154	5.3749	3.2785
	StdDev	0.6263	0.6763	0.7150	0.7704	0.9147
S. Sequence 3 (Day)	Mean	14.2960	12.6366	11.5303	10.1296	7.2940
	StdDev	0.6326	0.6009	0.5828	0.5638	0.5599
S. Sequence 4 (Day)	Mean	17.4666	14.8787	13.1039	10.7775	5.5624
	StdDev	0.6667	0.6842	0.7035	0.7387	0.8588
S. Sequence 5 (Night)	Mean	12.1335	10.9419	10.2137	9.3718	7.9456
	StdDev	1.0338	1.0565	1.0665	1.0750	1.0830
$\bar{M}$		13.4773	11.6411	10.4378	8.9340	5.8991
$\sigma_{\bar{M}}$		3.1384	2.7266	2.4437	2.1032	1.8268
$\bar{\sigma}$		0.9088	0.9121	0.9145	0.9185	0.9307
$\sigma_{\bar{\sigma}}$		0.4145	0.3946	0.3762	0.3470	0.2749

Table 7.2: PSNR Improvement in the Short Sequences using the Constant-Statistics Compensation Algorithm

Short Sequence Used		Portion of Standard Deviation Used				
		0.00	0.33	0.50	0.67	0.90
S. Sequence 1 (Day)	Mean	14.4846	12.3504	10.9555	9.2224	5.7961
	StdDev	1.5848	1.4900	1.4175	1.3131	1.0459
S. Sequence 2 (Day)	Mean	9.0060	7.4577	6.4607	5.2732	3.0339
	StdDev	0.6263	0.6648	0.6964	0.7439	0.8773
S. Sequence 3 (Day)	Mean	14.2960	12.4828	11.2669	9.7176	6.5224
	StdDev	0.6326	0.5672	0.5251	0.4732	0.3663
S. Sequence 4 (Day)	Mean	17.4666	14.8214	13.0032	10.6147	5.2395
	StdDev	0.6667	0.6781	0.6923	0.7027	0.8309
S. Sequence 5 (Night)	Mean	12.1335	10.8558	10.0707	9.1567	7.5838
	StdDev	1.0338	0.9642	0.9125	0.8437	0.7041
$\bar{M}$		13.4773	11.5912	10.3514	8.7969	5.6351
$\sigma_{\bar{M}}$		3.1384	2.7171	2.4123	2.0542	1.6980
$\bar{\sigma}$		0.9088	0.8729	0.8488	0.8153	0.7649
$\sigma_{\bar{\sigma}}$		0.4145	0.3755	0.3464	0.3096	0.2542

7.2. RESULTS OF LONG SEQUENCE ANALYSIS

Table 7.3: PSNR Improvement in the Short Sequences using the Fading-Memory Polynomial Filter with Window Size 20

Short Sequence Used		Portion of Standard Deviation Used				
		0.00	0.33	0.50	0.67	0.90
S. Sequence 1 (Day)	Mean	14.5527	12.5222	11.2288	9.6716	6.8318
	StdDev	2.0287	2.0743	2.1122	2.1704	2.3301
S. Sequence 2 (Day)	Mean	20.6341	19.0462	18.0532	16.8740	14.7577
	StdDev	3.7844	3.7596	3.7447	3.7279	3.7010
S. Sequence 3 (Day)	Mean	22.4671	20.6815	19.5293	18.1077	15.2813
	StdDev	3.5407	3.5537	3.5658	3.5871	3.6629
S. Sequence 4 (Day)	Mean	21.5562	19.1014	17.4466	15.3248	10.8353
	StdDev	4.6839	4.7685	4.8341	4.9269	5.1321
S. Sequence 5 (Night)	Mean	18.9844	17.6568	16.8496	15.9215	14.3707
	StdDev	4.0929	4.0922	4.0915	4.0905	4.0877
$\bar{M}$		19.6389	17.8016	16.6215	15.1799	12.4154
$\sigma_{\bar{M}}$		3.1210	3.1395	3.1749	3.2540	3.5776
$\bar{\sigma}$		3.6261	3.6497	3.6697	3.7006	3.7828
$\sigma_{\bar{\sigma}}$		0.9901	0.9928	0.9970	1.0014	1.0056

Table 7.4: PSNR Improvement in the Short Sequences using the Fading-Memory Polynomial Filter with Window Size 50

Short Sequence Used		Portion of Standard Deviation Used				
		0.00	0.33	0.50	0.67	0.90
S. Sequence 1 (Day)	Mean	14.0185	12.0370	10.7658	9.2197	6.3264
	StdDev	3.0341	3.1163	3.1776	3.2598	3.4185
S. Sequence 2 (Day)	Mean	18.4290	16.8621	15.8817	14.7162	12.6166
	StdDev	3.5626	3.5372	3.5228	3.5092	3.5056
S. Sequence 3 (Day)	Mean	18.9390	17.2473	16.1433	14.7624	11.9418
	StdDev	4.1057	4.2257	4.3345	4.5092	5.0022
S. Sequence 4 (Day)	Mean	19.6840	17.0726	15.2931	12.9812	7.91623
	StdDev	3.7929	3.8537	3.9001	3.9673	4.1302
S. Sequence 5 (Night)	Mean	15.7733	14.4559	13.6532	12.7270	11.1640
	StdDev	2.7894	2.7680	2.7551	2.7404	2.7155
$\bar{M}$		17.3688	15.5350	14.3472	12.8813	9.9930
$\sigma_{\bar{M}}$		2.3833	2.2615	2.2237	2.2554	2.7299
$\bar{\sigma}$		3.4569	3.5002	3.5380	3.5972	3.7544
$\sigma_{\bar{\sigma}}$		0.5407	0.5780	0.6141	0.6754	0.8591

7.2. RESULTS OF LONG SEQUENCE ANALYSIS

Table 7.5: PSNR Improvement in the Short Sequences using the Fading-Memory Polynomial Filter with Window Size 100

Short Sequence Used		Portion of Standard Deviation Used				
		0.00	0.33	0.50	0.67	0.90
S. Sequence 1 (Day)	Mean	13.9308	11.7993	10.4170	8.7185	5.4786
	StdDev	3.1597	3.7553	3.0091	2.9093	2.6263
S. Sequence 2 (Day)	Mean	14.1200	12.5625	11.5865	10.4236	8.3178
	StdDev	3.4554	3.3448	3.2735	3.1903	3.0700
S. Sequence 3 (Day)	Mean	15.1571	13.2762	12.0318	10.4560	7.1845
	StdDev	2.0862	2.1842	2.2629	2.3796	2.6902
S. Sequence 4 (Day) cline2-7	Mean	18.0273	15.3414	13.5010	11.0940	5.7479
	StdDev	1.7172	1.7299	1.7348	1.7347	1.6943
S. Sequence 5 (Night)	Mean	12.9678	11.6674	10.8725	9.9522	8.3879
	StdDev	1.4757	1.4416	1.4199	1.3937	1.3439
$\bar{M}$		14.8406	12.9294	11.6818	10.1289	7.0233
$\sigma_{\bar{M}}$		1.9436	1.4952	1.1933	0.8868	1.3763
$\bar{\sigma}$		2.3788	2.3552	2.3400	2.3215	2.2849
$\sigma_{\bar{\sigma}}$		0.8814	0.8296	0.7965	0.7597	0.9300

Table 7.6: PSNR Improvement in the Long Sequences using the Reference-Free Compensation Algorithm

Long Sequence Used		Portion of Standard Deviation Used				
		0.00	0.33	0.50	0.67	0.90
L. Sequence 1 (Day)	Mean	14.2385	12.1418	10.7937	9.1229	5.8678
	StdDev	2.1264	2.0694	2.0288	1.9767	1.8825
L. Sequence 2 (Day)	Mean	13.4169	11.6537	10.4828	9.0035	6.0765
	StdDev	0.8927	0.9881	1.0503	1.1230	1.2303
L. Sequence 3 (Night)	Mean	13.7081	12.7037	12.0855	11.3641	10.1205
	StdDev	4.0333	3.9567	3.9111	3.8597	3.7763
$\bar{M}$		13.7878	12.1687	11.1207	9.8302	7.3549
$\sigma_{\bar{M}}$		0.4166	0.5253	0.8499	1.3298	2.3973
$\bar{\sigma}$		2.3508	2.3381	2.3301	2.3198	2.2964
$\sigma_{\bar{\sigma}}$		1.5823	1.5024	1.4540	1.4002	1.3225

7.2. RESULTS OF LONG SEQUENCE ANALYSIS

Table 7.7: PSNR Improvement in the Long Sequences using the Constant-Statistics Compensation Algorithm

Long Sequence Used		Portion of Standard Deviation Used				
		0.00	0.33	0.50	0.67	0.90
L. Sequence 1 (Day)	Mean	14.2385	12.2926	11.0343	9.4866	6.4810
	StdDev	2.1264	2.0620	2.0207	1.9734	1.9101
L. Sequence 2 (Day)	Mean	13.4169	11.5519	10.3118	8.7480	5.5993
	StdDev	0.8927	0.9409	0.9671	0.9887	0.9720
L. Sequence 3 (Night)	Mean	13.7081	12.6203	11.9493	11.1648	9.8061
	StdDev	4.0333	3.9290	3.8660	3.7944	3.6782
$M$		13.7878	12.1549	11.0985	9.7998	7.2955
$\sigma_M$		0.4166	0.5473	0.8207	1.2385	2.2185
$\bar{\sigma}$		2.3508	2.3106	2.2846	2.2522	2.1868
$\sigma_{\bar{\sigma}}$		1.5823	1.5095	1.4674	1.4235	1.3741

Table 7.8: PSNR Improvement in the Long Sequences using the Fading-Memory Polynomial Filter with Window Size 20

Long Sequence Used		Portion of Standard Deviation Used				
		0.00	0.33	0.50	0.67	0.90
L. Sequence 1 (Day)	Mean	16.3992	14.5726	13.4279	12.0703	9.6561
	StdDev	4.1038	4.2389	4.3392	4.4767	4.7821
L. Sequence 2 (Day)	Mean	22.6915	20.7441	19.4831	17.9288	14.8693
	StdDev	3.4796	3.5150	3.5488	3.6048	3.7680
L. Sequence 3 (Night)	Mean	16.3208	15.0548	14.3079	13.4753	12.1635
	StdDev	3.7015	3.7248	3.7386	3.7539	3.7766
$M$		18.4705	16.7905	15.7396	14.4915	12.2296
$\sigma_M$		3.6557	3.4324	3.2717	3.0586	2.6072
$\bar{\sigma}$		3.7616	3.8262	3.8755	3.9451	4.1089
$\sigma_{\bar{\sigma}}$		0.3164	0.3725	0.4126	0.4663	0.5830

7.2. RESULTS OF LONG SEQUENCE ANALYSIS

Table 7.9: PSNR Improvement in the Long Sequences using the Fading-Memory Polynomial Filter with Window Size 50

Long Sequence Used		Portion of Standard Deviation Used				
		0.00	0.33	0.50	0.67	0.90
L. Sequence 1 (Day)	Mean	15.0228	13.2674	12.1655	10.8550	8.5071
	StdDev	3.5543	3.6564	3.7350	3.8468	4.1097
L. Sequence 2 (Day)	Mean	20.0358	18.1357	16.8989	15.3626	12.2812
	StdDev	3.1235	3.1691	3.2238	3.3243	3.6431
L. Sequence 3 (Night)	Mean	14.5885	13.5148	12.8855	12.1867	11.0884
	StdDev	2.8717	2.8495	2.8375	2.8253	2.8090
$\bar{M}$		16.5490	14.9726	13.9833	12.8014	10.6256
$\sigma_{\bar{M}}$		3.0274	2.7421	2.5505	2.3158	1.9291
$\bar{\sigma}$		3.1832	3.2694	3.6254	3.3321	3.5206
$\sigma_{\bar{\sigma}}$		0.3452	0.4445	0.4502	0.5108	0.6589

Table 7.10: PSNR Improvement in the Long Sequences using the Fading-Memory Polynomial Filter with Window Size 100

Long Sequence Used		Portion of Standard Deviation Used				
		0.00	0.33	0.50	0.67	0.90
L. Sequence 1 (Day)	Mean	14.2985	12.5366	11.4383	10.1069	7.7224
	StdDev	2.6448	2.6806	2.7300	2.8265	3.1444
L. Sequence 2 (Day)	Mean	17.1414	15.1523	13.8472	12.2145	8.9264
	StdDev	3.1235	3.1691	3.2238	3.3243	3.6431
L. Sequence 3 (Night)	Mean	13.3229	12.2774	11.6525	10.9452	9.7931
	StdDev	2.5628	2.5836	2.6062	2.6424	2.7299
$\bar{M}$		14.9209	13.3221	12.3093	11.0889	8.8140
$\sigma_{\bar{M}}$		1.9839	1.5903	1.3365	1.0611	1.0399
$\bar{\sigma}$		2.4376	2.4632	2.4889	2.5427	2.7285
$\sigma_{\bar{\sigma}}$		0.2634	0.2965	0.3165	0.3447	0.4167

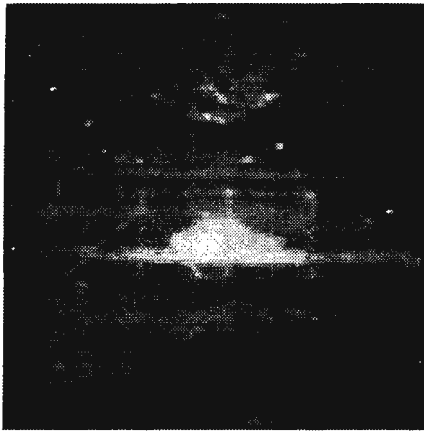
## Chapter 8

# Discussion

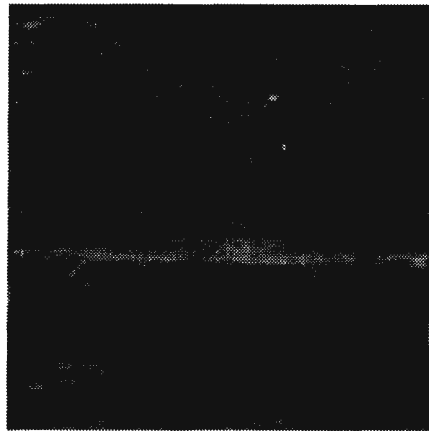
### 8.1 Visible Differences between Original and Compensated Images

A visual inspection of the compensated output images in all of the tested algorithms, confirmed the removal of noise fingerprints that result from fixed pattern spatial noise. The visible results for the Reference-Free Compensation algorithm using the Long Night sequence were presented in Fig. 7.1. Here, a single image frame is repeated at different points in the compensation process to indicate the overall progress of the algorithm. An advantage of using the same image frame is that visible differences between the input image and the compensated output image can be more easily noted. This allows for a relative comparison of the progress of the algorithm as the number of iterations increase. Visible differences between the input and compensated output image can be seen in terms of image uniformity and contrast as the compensated images are presented at 10, 50, 100, 500 and 900 iterations in Fig. 7.1(b) to Fig. 7.1(f). The degree of fixed pattern noise removal is noted to improve as the iteration count increases (i.e. as more images are used for the compensation process resulting in more image statistics). The original image and output image after 900 iterations are repeated in Fig. 8.1(a) and Fig. 8.1(b). Once again, the portion of standard deviation  $P$  used was 0.5.

The original image scene contains a car, a fence and a small building in the camera field of view. Upon a first glance of the image, these objects do not appear very distinct and are almost indiscernible. The appearance of trees in the background together with the rest of the scene is masked by a cloudy, or misty, fixed pattern noise. The image also appears to be brighter in the centre compared to the edges. Pixels in the centre regions of the image seem to have higher values than their neighbours on the edges. Certain dead pixel elements also leave the impression that they are point sources, perhaps of distant infrared light sources far



(a) Original Image



(b) Output Image after 900 Iterations

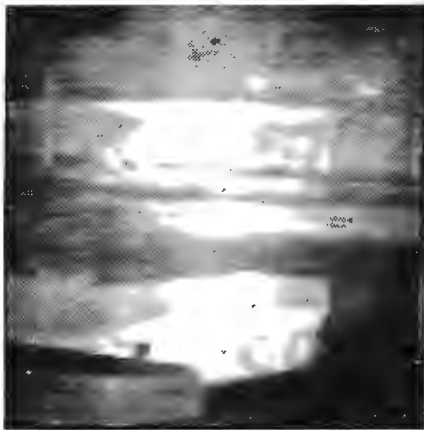
Figure 8.1: Original Image compared to Output Image corrected using the Reference-Free Compensation scheme

in the background. The overall image quality is low. There is visible lack of contrast and pertinent detail in this input image.

Examining the output image given by the Reference-Free Compensation technique after 900 iterations, a vast difference can be seen between the original image and the compensated image. The compensated image appears significantly more uniform with a greater degree of contrast between objects. The car, fence and small building are also much more identifiable. An increased amount of detail can be seen in the trees in the background. The haziness, or cloudiness, associated with fixed pattern noise that troubled the original image has been corrected for. The problem wherein the centre of the image appears brighter than the edges has also been addressed. Note that the car now appears less bright in the output than it does in the original. Dead pixel elements, that appear like infrared light sources in the distance, have also been corrected for. The elimination of these spurious artifacts arising from dead pixels helps prevent the detection of these false point sources. This results in making the detection of true point targets much easier.

Overall, the output image corrected using the Reference-Free Compensation scheme appears to be a significant improvement over the original image visually in terms of image clarity. The effects of the noise fingerprint is noted to diminish as more images are used during the iteration process. Another pair, comprising of an input and output image corrected by the Reference-Free Compensation scheme, is presented in Fig. 8.2(a) and Fig. 8.2(b). This scene is of a tanker, and was obtained after 900 iterations using the Long Night Sequence. The  $P$  value used was 0.5.

## 8.1. VISIBLE DIFFERENCES BETWEEN ORIGINAL AND COMPENSATED IMAGES



(a) Original Image



(b) Output Image after 900 Iterations

Figure 8.2: Output Image corrected using the Reference-Free Compensation scheme compared to Original Image

Once again, note that the removal of the fixed pattern noise fingerprint allows the output image to appear more uniform than the input image. The centre and edges of the output image are of similar brightness. There is also a higher level of contrast between the tanker and the background. The fence in the background is now more visible. The output image is a vast improvement over the original image in terms of uniformity as objects in the scene are more easily recognisable and discerned. The output image is also more clear than the original image.

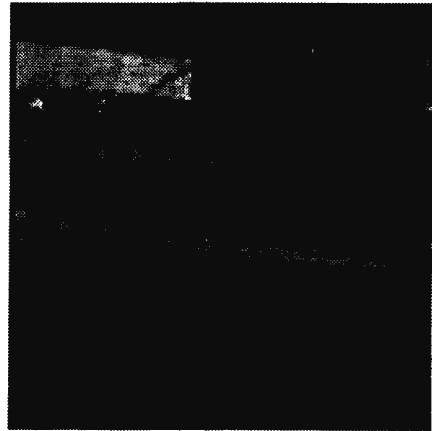
Output images obtained using the other compensation schemes are presented in Fig 8.3(b) to Fig. 8.3(f). Here the original input image, in Fig. 8.3(a), is compared to the output image of the Reference-Free Compensation algorithm, the Constant-Statistics algorithm and Fading-Memory polynomial windows with exponential window sizes of 20, 50 and 100. All of the outputs were obtained after 500 iterations and the portion of standard deviation used,  $P$ , was 0.5. The side view of a building is shown in this scene.

Comparing the various output images from their respective compensation schemes to the input image, a remarkable difference can be seen in terms of the compensated output image quality compared to the input image quality. All of the output images appear more uniform with a greater level of contrast more evident between the objects and landscape in the scene. The cloudiness or haziness that troubles the input image has been removed by all of the algorithms. All of them display an increase in overall clarity due to the removal of fuzzy haziness associated with the fixed pattern noise fingerprint. Although the outputs from individual algorithms are not exactly the same, they all yield output images which are better than the original input

8.1. VISIBLE DIFFERENCES BETWEEN ORIGINAL AND COMPENSATED IMAGES



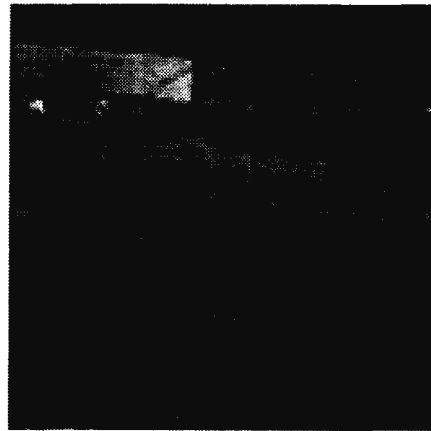
(a) Original Picture



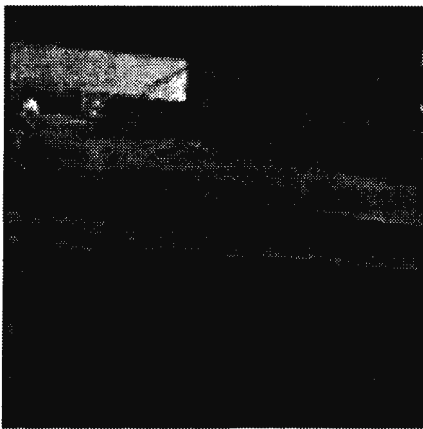
(b) Output Image using Reference-Free Correction Algorithm



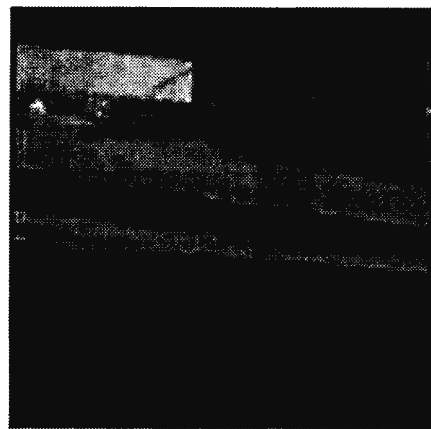
(c) Output Image using Constant-Statistics Algorithm



(d) Output Image using Fading-Memory Polynomial Filter: Exponential Window 20



(e) Output Image using Fading-Memory Polynomial Filter: Exponential Window 50



(f) Output Image using Fading-Memory Polynomial Filter: Exponential Window 100

Figure 8.3: Visible Performance of Various Compensation Algorithms on the Same Sequence

image.

The output images from the Constant-Statistics algorithm looked similar to those given by Reference-Free Compensation scheme. Output images obtained using the Fading-Memory Polynomial filters also displayed greater uniformity. Once again, the visual correction of nonuniformities, where central regions in the input image appear brighter than the edges, were noted in the compensated output images of the Fading-Memory Polynomial filters. The presence of dead pixels and noise fingerprints were also removed. The output images displayed good contrast with objects in the camera field of view appearing much clearer.

Thus, evaluating the performance of the compensation algorithms solely from a visual perspective, the tested algorithms do offer adequate nonuniformity compensation. All of them improve overall image quality by removing artifacts of fixed pattern spatial noise, and correcting for dead pixels and noise fingerprints.

## 8.2 Analytical Differences between Original and Compensated Images

Tables 8.1 and 8.2 contain a summary of the overall mean improvements in peak Signal-to-Noise ratio (in  $dB$ ) of the output image compared to the input image of the sequence. These results were obtained by taking the mean PSNR improvements of all of the sequences where the respective correction algorithm was used. The standard deviations of these overall mean improvements are also indicated. The results for the short sequences are presented in Table 8.1 and the results for the longer sequences are presented in 8.2.

Table 8.1: Overall PSNR Improvement in the Short Sequences

Correction Method		Portion of Standard Deviation Used				
		0.00	0.33	0.50	0.67	0.90
Averaging	Mean	13.4773	11.6411	10.4378	8.9340	5.8991
	StdDev	3.1384	2.7266	2.4437	2.1032	1.8268
CS Averaging	Mean	13.4773	11.5912	10.3514	8.7969	5.6351
	StdDev	3.1384	2.7171	2.4123	2.0542	1.6980
Exp Window 20	Mean	19.6389	17.8016	16.6215	15.1799	12.4154
	StdDev	3.1210	3.1395	3.1749	3.2540	3.5776
Exp Window 50	Mean	17.3688	15.5350	14.472	12.8813	9.9930
	StdDev	2.3833	2.2615	2.2237	2.2554	2.7299
Exp Window 100	Mean	14.8406	12.9294	11.6818	10.1289	7.0233
	StdDev	1.9436	1.4952	1.1933	0.8868	1.3763

Table 8.2: Overall PSNR Improvement in the Long Sequences

Correction Method		Portion of Standard Deviation Used				
		0.00	0.33	0.50	0.67	0.90
Averaging	Mean	13.7878	12.7037	11.1207	9.8302	7.3549
	StdDev	0.4166	0.5353	0.8499	1.3298	2.3973
CS Averaging	Mean	13.7878	12.1549	11.0985	9.7998	7.2955
	StdDev	0.4166	0.5473	0.8207	1.2385	2.2185
Exp Window 20	Mean	18.4705	16.7905	15.7396	14.4915	12.2296
	StdDev	3.6557	3.4324	3.2717	3.0586	2.6072
Exp Window 50	Mean	16.5490	14.9726	13.9833	12.8014	10.6256
	StdDev	3.0274	2.7421	2.5505	2.3158	1.9291
Exp Window 100	Mean	14.9209	13.3221	12.3093	11.0889	8.8140
	StdDev	1.8939	1.5903	1.3365	1.0611	1.0399

Examining Tables 8.1 and 8.2 presented above, it can be seen that all of the nonuniformity compensation algorithms implemented yielded significant improvements in the peak Signal-to-Noise ratio of the output image compared to that of the input. The standard deviations of these mean improvements are also fairly low indicating that these improvements do not depend on the type of sequence used but rather on the compensation process itself. This feature asserts that similar results may be expected when other sequences are used.

The Reference-Free Compensation scheme performed well achieving minimum and maximum PSNR improvements of approximately 6 dB and 13 dB respectively in both the long and short sequences. Low standard deviations associated with the mean improvements indicate that there is not much variation in the mean performance of this algorithm when different sequences are used. The performance of the Constant-Statistics algorithm was similar to that of the Reference-Free Compensation algorithm in terms of high PSNR improvement and low standard deviations of the mean improvement. The Reference-Free Compensation scheme did perform only marginally better than the Constant-Statistics algorithm, thus verifying Chiang's statement [6]. The average differences between the both of these techniques was only 0.1344 dB and 0.1652 dB for the short and long sequences respectively.

This slight improvement in performance is a high penalty to pay when one compares the superior computational saving the Constant-Statistics algorithm offers over the Reference-Free Compensation scheme. Both the Reference-Free Compensation algorithm and Constant-Statistics algorithms performed better on the longer sequences compared to the shorter sequences. This characteristic is attributed to better averaging as more frames were averaged when longer sequences were used compared to when the shorter sequences were used.

The results for the Fading-Memory Polynomial filters are also slightly better for the longer

sequences. In both the long and short sequences, the filters with smaller exponential windows displayed a much better PSNR improvement compared to filters with larger windows. The filter with the exponential window of length 20 performed the best in terms of overall PSNR improvement. This filter, as illustrated in Chapter 5.2.3, has the highest cut-off frequency of the three. In having a small exponential window and high forgetfulness factor, it is able to cope slightly faster with sudden changes in the input image compared to the other two filters. It does, however, suffer from a higher standard deviation in its mean PSNR improvement compared to the other two. The filter of window size 100 offers adequate PSNR improvement and greater stability in terms of a much lower standard deviation about the mean improvement when compared to the others. It is also interesting to note that in all cases the results obtained using Fading-Memory Polynomial filters were better than those given by the Constant-Statistics algorithm and Reference-Free Compensation scheme. This feature is attributed to the exponential weighting of most recent scenes that Fading-Polynomial filters present over the Reference-Free Compensation and Constant-Statistics algorithms. Both the Reference-Free Compensation and Constant-Statistics methods weight input frames equally and do not have any forgetfulness factors associated with them.

Ultimately, when implemented in a real camera system, the most appropriate Fading-Memory Polynomial filter would depend on the type of  $1/f$  noise present in the system. This characterisation would require examining the performance of the camera over extended periods of time (perhaps hours or even days) to obtain an estimate of the overall system  $1/f$  noise. A detailed frequency response of the system would also need to be obtained. This will contribute to the understanding of how system as a whole drifts due to the influence of  $1/f$  noise.

It was also noted that as the portion  $P$  of standard deviation used in the compensation process is increased, the PSNR improvements of all of the compensation methods decrease. This decrease in PSNR does correspond to the increase in the overall output image contrast and is discussed in greater detail in the section following on Contrast Enhancement.

Hence, from an analytical perspective, all of the implemented algorithms performed well in improving the overall PSNR of the input camera image. They all yielded consistent nonuniformity compensation correcting for the effects of fixed pattern noise.

### 8.3 Contrast Enhancement

As stated earlier in Section 6.6, a greater degree of contrast enhancement may be achieved by using an increased portion  $P$  of individual pixel standard deviation. When  $P$  is increased the gain or responsivity of each pixel increases. Higher values of  $P$  allow pixels to have a greater output range of display, leading to an image with greater contrast between individual pixels.

Lower values of  $P$  correspond to little contrast enhancement whereas higher values lead to much greater contrast between pixels in the infrared image. Figure 8.4 presents a comparison between the input image and output images with different  $P$  values. The performances of the Reference-Free Compensation technique with variations in  $P$  values are displayed in these output images. The images were obtained from the Long Day Sequence 1 after 500 iterations.

As visibly indicated in Fig. 8.4(b) through to Fig. 8.4(f), the level of contrast enhancement in the output image depends on the value of  $P$  selected. Output images having good contrast look better visually than those with low contrast as more information is conveyed. One would thus expect the PSNR improvement evaluated for contrast enhanced output images to be superior to the PSNR improvement evaluated for output images that do not have any contrast enhancement.

However, examining the results of PSNR improvement for the various sequences, it can be seen that when higher  $P$  values are used (corresponding to greater contrast), the overall mean level of PSNR improvement decreases. Thus, output images with higher levels of contrast between pixels appear to have experienced a lower overall mean PSNR improvement. This discrepancy can be explained when considers how the PSNR improvement is actually calculated. The Output peak Signal-to-Noise ratio is evaluated by averaging the output images of the sequence in time and calculating how far away from a uniform grey background of value 128 this time averaged output image is. If an ideal or perfect sequence was used, the time average of each pixel in a compensated output image frame would equal 128, yielding an almost infinite PSNR. However, due to individual sequence characteristics and variations, as well as the limited number of averaged frames, the time average of individual pixels in the compensated output image may not equal the value of 128, but only approximate or approach this value.

When contrast enhancement is performed on individual pixels in the output image by variations in the  $P$  value, the individual display responsivities of these pixels are increased. These pixels therefore exhibit both raised and lowered intensity values. When time averaged, pixels in the contrast enhanced compensated output image would thus experience greater deviations from their normal time averaged values. This results in a greater level of noise being detected in the contrast enhanced (or responsivity enhanced) output image compared to the normally compensated output image, where only offset effects are corrected for. It is due to this reason that the improvement in PSNR calculated for sequences with a great degree of contrast enhancement (high  $P$  values) is lower than that for the same sequence when no or lower contrast enhancement (no or smaller  $P$  values) is used.



(a) Original Picture

(b) Output Image with  $P = 0.0$ (c) Output Image with  $P = 0.25$ (d) Output Image with  $P = 0.50$ (e) Output Image with  $P = 0.75$ (f) Output Image with  $P = 0.90$ Figure 8.4: Indication of Contrast Enhancement in the Output Image by variation of  $P$  Value

## 8.4 Motion Dependence and Ghosting Artifacts

All of the implemented scene based reference free correction algorithms require that objects in the field of view of the camera do not remain stationary for too long, hence the need for camera panning and motion within the infrared scene. However, if an object in the image remains stationary or the camera is not adequately panned, this assumption is violated. The object in the image will blend into the background as the compensation procedure would assume that the object is a part of the fixed pattern noise and correct for it. If this stationary object does eventually move within or out of the camera field of view, it will leave a reverse ghost image in the scene. This ghost image results from the modified offset coefficients that compensation process had to calculate in order to correct for the stationary image. Hence, the fixed pattern noise detected by the compensation process due to the ghost image is not a true reflection of the fixed pattern noise actually affecting the system. These ghost images are especially apparent when only a small number of input image frames have been used for calibration, as is the case during the initial start up or beginning stages of the compensation procedure. An example of ghosting artifacts is shown in Fig. 8.5. Here, the output image as it should appear is compared to the output image with ghosting artifacts. Note also that time averaged ghost output image shows greater spatial variations compared to the time averaged true output image. This indicates that either the camera was staring at the same scene for too long and was then suddenly moved or that far too few frames were used in the compensation process so far.

The problems associated with the motion dependence requirements of all of the presented compensation algorithms may be solved in part by using a buffer to temporarily hold or save output image offset and responsivity compensation coefficients when no motion within the scene or of the camera assembly is detected. This practice would help eliminate ghosting artifacts as well as prevent the input scene from fading into the background. Once camera motion is restored or scene motion detected, the compensation coefficients may be re-evaluated and corrected, thereby updating the holding buffers. This proposed method should work well when the camera is not required to stare at single objects for extended periods of time. If the camera is required to stare at objects for long time periods, then the effects of  $1/f$  noise would become more pronounced. Temperature reference compensation methods would be more appropriate and suitable to these types of staring camera systems.

## 8.5 Compensated Image Post-Processing

Image post-processing may be used to highlight and identify significant features in the nonuniformity corrected output images. These processes are normally user defined and depend upon



(a) Original Image



(b) True Output Image



(c) Output Image with Ghosting Artifacts



(d) Time Averaged True Output



(e) Time Averaged Ghost Output

Figure 8.5: True Output Image compared to Output Image with Ghosting Artifacts

individual user requirements. Users of infrared camera systems usually determine what they would like to see or recognise in the infrared scene and implement post-processing techniques accordingly. Such image post-processing techniques may include image histogram equalisation, image segmentation and object motion estimation in the scenes or imagery under view.

Compensated output infrared images and visible images of the scene may also be used together in multi-sensor fusion applications. This techniques aids in automating target detection. Data obtained from radar and sonar devices may also be used in the target recognition/detection process. Thus, the use of image post-processing techniques contribute to making resultant compensated images more appealing and more useful to computers and human operators as well as to increase the overall level of information conveyed in these images.

## Chapter 9

# Conclusions and Recommendations

### 9.1 Conclusions

Reference free correction techniques have been shown to be successful in correcting for the effects of fixed pattern spatial noise that troubles a mercury cadmium telluride infrared focal plane array. These easily implemented techniques operate without the need for traditional temperature references and use scene-based methods to evaluate responsivity and offset compensation coefficients. In all of the compensation techniques, the updating of the correction terms are continuous: the field of view of the camera is not interrupted as no complex optical shutter assemblies are used.

All of the implemented algorithms were successful in removing artifacts of fixed pattern spatial noise that limit the sensitivity of the infrared camera. The compensated images appeared to be visually much more uniform and clearer than the original camera images. The levels of contrast between objects and the background in the scenes also increased as a result of the implemented nonuniformity compensation processes. Dead pixel elements, that can be misinterpreted as infrared point targets, were also corrected for. This correction also helped contribute to the greater uniformity in the compensated output image.

All of the correction algorithms yielded significant improvements in the peak Signal-to-Noise ratio of the compensated output image compared to the original input image. The Reference-Free Compensation algorithm and Constant-Statistics algorithm, were noted to give similar results. However, the Constant-Statistics algorithm did offer significant computational saving over the Reference-Free Compensation scheme, whilst maintaining similar performance. This led to the favourable selection of the Constant-Statistics algorithm over the Reference-Free Compensation scheme.

The implementation of Fading-Memory Polynomial filters also indicated a significant improvement in the peak Signal-to-Noise ratio of the compensated output image compared to the original camera image. These Fading-Memory Polynomial filters performed better than both the Reference-Free Compensation scheme and Constant-Statistics algorithm in terms of overall peak Signal-to-Noise ratio improvement. The use of Fading-Memory Polynomial filters, allow the computed offsets to continually track variations in detector offset currents due to changes in dewar temperature and  $1/f$  noise mechanisms. Thus, any variations in the offset currents corresponding to environmental factors, like temperature changes and varying operating conditions, are monitored with compensation occurring immediately.

Thus, reference free corrective techniques offer many advantages over traditional temperature based methods. Apart from the relative ease of implementation, these methods allow immediate compensation with no hardware requirements or special calibration procedures/images. The ability to compensate for the effects of spatial noise using scene-based methods and statistics of the scenes under view contribute to making infrared camera systems more robust. This increase in robustness complements these systems, suiting them to quick field deployment and rugged field use.

## 9.2 Recommendations

If reference free corrective techniques are to be applied to an existing camera system, many precautionary measures would need to be implemented. The need for these precautions arise from the scene degradation and ghosting artifacts that result when the camera lies still. Techniques that detect motion within the infrared scene under view, as well as the relative panning motion of the camera, would need to be implemented to prevent the above mentioned problems. These techniques would allow for the updating of buffers holding compensation coefficients only when motion is detected, thereby compensating for the problems associated with scene fading/degradation and ghosting artifacts.

Unfortunately, no standard method was discovered by this author to characterise image quality based on the image's inherent spatial characteristics. Perhaps, such a method may be agreed upon in the future allowing for detailed analytical comparisons between the reference free corrective techniques, presented herein, and other compensation techniques. It is hoped that such a method would also be able to quantify, with some degree of accuracy, what we are all looking for in an image. After all,

*An image, in all of its simplicity, is just a reflection of the moment captured in time.*

# Bibliography

- [1] N. BLUZER AND A. S. JENSEN. Current readout in infrared detectors. *Optical Engineering*, 26(3):241–248, March 1987.
- [2] N. BLUZER. Sensitivity limitations in IRFPA's imposed by detector nonuniformities. *SPIE Infrared Detectors and Arrays*, 930:64–72, 1988.
- [3] G. D. BOREMAN AND C. CONSTANZO. Compensation for gain nonuniformity and nonlinearity in HgCdTe infrared charge-coupled-device focal planes. *Optical Engineering*, 26(10):981–984, October 1987.
- [4] G. D. BOREMAN AND P. L. HERON. Description of fixed pattern noise in CCD's using the spatial power spectrum. *SPIE Thermal Imaging*, 636:55–59, 1986.
- [5] B. D. BUCKNER. Mercury cadmium telluride photodiodes. <http://enuxsa.eas.asu.edu/buckner/mct.html>.
- [6] Y. M. CHIANG AND J. G. HARRIS. Nonuniformity correction using the constant statistics constraint: Analog and digital implementations. In B. F. ANDRESEN AND M. STROJNIK, editors, *SPIE Aerospace/Defense Sensing and Controls: Infrared Technology and Applications XXIII*, volume 3061, pages 895–905, April 1997.
- [7] V. DHAR AND R. ASHOKAN. Computer simulation of fixed-pattern-noise-limited noise-equivalent-temperature differences in mercury cadmium telluride focal-plane arrays. *Optical Engineering*, 34(5):1316–1323, May 1995.
- [8] V. GOPAL AND V. DHAR. Control and design of nonuniformities in a hybrid focal plane array. *Optical Engineering*, 31(11):2330–2335, November 1992.
- [9] V. GOPAL. Model for response nonuniformity calculations of a direct-injection readout hybrid focal plane array. *Optical Engineering*, 33(3):809–819, March 1994.
- [10] HANSEN, SCHMIDT, AND CASSELMAN. Energy gap vs. alloy composition and temperature in HgCdTe. *Journal of Applied Physics*, (55):7099–7101, 1982.

- 
- [11] F. N. HOOGE. 1/f noise sources. *IEEE Transactions on Electron Devices*, 41(11):1926–1934, November 1994.
- [12] R. C. HUNSPERGER, editor. *Photonic Devices and Systems*. Marcel Dekker, INC, Marcel Dekker, INC, 270 Madison Avenue, New York, New York, 1994.
- [13] R. H. KINGSTON. *Detection of Optical and Infrared Radiation*. Springer-Verlang, Springer-Verlang, Berlin, Heidelberg, 1978.
- [14] P. MACKEY, F. R. BARONE, AND N. A. CHU. real time nonuniformity correction for focal plane arrays using 12 bit digital electronics. *SPIE Processing of Images and Data from Optical Sensors*, 292:210–217, 1981.
- [15] J. L. MILLER. *Principles of Infrared Technology*. Van Nostrand Reinhold, Van Nostrand Reinhold, 115 Fifth Avenue, New York, NY 10003, 1994.
- [16] A. F. MILTON, F. R. BARONE, AND M. R. KRUER. The influence of nonuniformity on IR focal plane array performance. In *Second Conference on Advanced IR Detectors and Systems*, 1983.
- [17] M. MOODLEY. Cranial ultrasonography, CK-BB and neurological assessment as predictors of outcome in hypoxic ischaemic encephalography. *Adhikari Annals of Tropical Paediatrics*, 13(2):195–200, 1993.
- [18] J. M. MOONEY. Effect of spatial noise on the minimum resolvable temperature of a staring sensor. *Applied Optics*, 30(23):3324–3332, August 1991.
- [19] J. M. MOONEY, F. D. SHEPARD, W. S. EWING, J. E. MURGUIA, AND J. SILVERMAN. Response nonuniformity limited performance of infrared staring cameras. *Optical Engineering*, 28(11):1151–1161, November 1989.
- [20] N. MORRISON. *Introduction to Sequential Smoothing and Prediction*. McGraw-Hill Book Comapany, 1969.
- [21] P. M. NARENDRA. Reference free nonuniformity correction for IR imaging arrays. *SPIE Smart Sensors 2*, 252:10–17, 1980.
- [22] S. B. PARKER, editor. *Optics Source Book*. Mcgraw Hill, 1988.
- [23] G. V. PAROPAT. Nonlinear compensation for responsivity nonuniformities in cadmium mercury telluride focal plane arrays. *Optical Engineering*, 28(8):887–896, August 1989.
- [24] D. L. PERRY. Linear theory of nonuniformity correction in platinum silicide focal plane arrays. *SPIE Infrared Technology XVIII*, 1762:60–69, 1992.

- 
- [25] D. L. PERRY AND E. L. DERENIAK. Linear theory of nonuniformity correction in infrared staring arrays. *Optical Engineering*, 32(8):1854–1859, August 1993.
- [26] A. ROGALSKI. New trends in semiconductor infrared detectors. *Optical Engineering*, 33(5):1395–1412, May 1994.
- [27] D. A. SCRIBNER, M. R. KRUER, AND J. C. GRIDLEY. Physical limitations to nonuniformity correction in IR focal plane arrays. *SPIE Focal Plane Arrays: Technology and Applications*, 865:185–202, 1987.
- [28] D. A. SCRIBNER, M. R. KRUER, K. SARKADY, AND J. C. GRIDLEY. Spatial noise in staring IR focal plane arrays. *SPIE Infrared Detectors and Arrays*, 930:56–63, 1988.
- [29] D. A. SCRIBNER, K. A. SARKADY, M. R. KRUER, AND J. T. CAULFIELD. Adaptive nonuniformity correction for IR focal plane arrays using neural networks. *SPIE Infrared Sensors, Detectors, Electronics and Signal Processing*, 1541:100–109, 1991.
- [30] D. A. SCRIBNER *et al.* Nonuniformity correction for staring IR focal plane arrays using scene-based techniques. *SPIE Infrared Detectors and Focal Plane Arrays*, 1308:224–233, 1990.
- [31] L. SHANGQIAN, L. CHIWEI, P. JIHONG, AND W. CHANGLUAN. Fixed pattern noise of IRCCD camera and method of correction. *SPIE Infrared Technology XVIII*, 1762:531–535, 1992.
- [32] I. SIMON. *Infrared Radiation*. D. van Nostrand Company, INC, D. van Nostrand Company, INC, 120 Alexander Street, Princeton, New Jersey, United States, 1966.
- [33] F. A. SOWAN, editor. *Applications of Infrared Detectors*. Mullard Limited, Mullard Limited, Mullard House, Torrington Place, London WC1E 7HD, 1971.
- [34] S. P. TOBIN, S. IWASA, AND T. J. TREDWELL. 1/f noise in HgCdTe photodiodes. *IEEE Transactions on Electron Devices*, 27(1):43–48, January 1980.
- [35] M. L. TOISON. *Infrared and Its Thermal Implications*. Philips Technical Library, N.V. Philips' Gloeilampenfabrieken, Eindhoven, The Netherlands, 1964.
- [36] R. WAYNANT AND M. EDIGER. *Electro-optics Handbook*. Optical and Electro-optical series. McGraw Hill, 1994.
- [37] D. T. WHINRAY. Fixed pattern noise correction for staring arrays in guidance systems. In *Advanced IR Detectors and Systems*, 1981.
- [38] J. WILSON AND J. F. B. HAWKES. *Optoelectronics: An Introduction*. Prentice Hall International, Prentice Hall International, Great Britain, 1983.

- [39] H. C. WRIGHT. *Infrared Techniques*. Clarendon Press Oxford, Oxford University Press, Ely House, London, 1973.
- [40] C. YEH. *Applied Photonics*. Academic Press INC, Academic Press Limited, 24-28 Oval Road, London NW1 7DX, 1994.

## Appendix A

# Graphical Results Obtained using the Reference-Free Compensation Algorithm

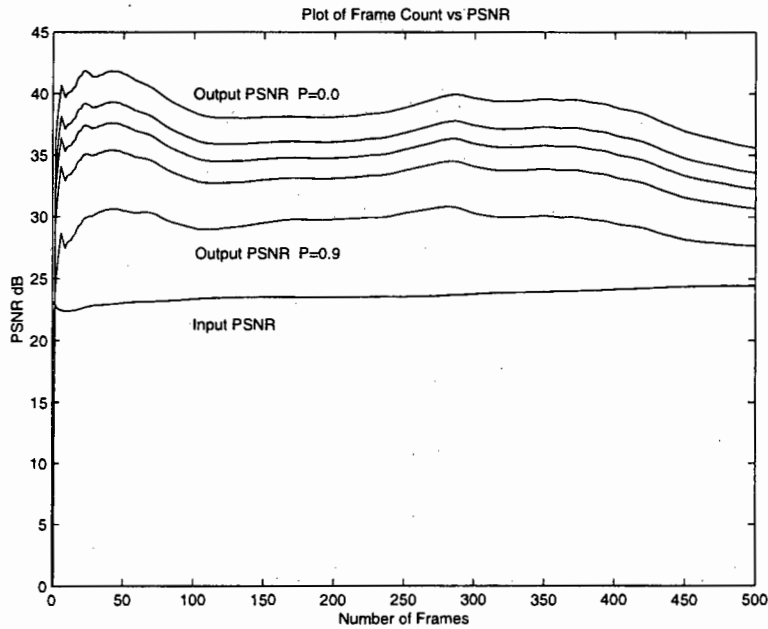


Figure A.1: Performance of Reference-Free Compensation Scheme on Short Day Sequence 1

APPENDIX A. GRAPHICAL RESULTS OBTAINED USING THE REFERENCE-FREE  
COMPENSATION ALGORITHM

---

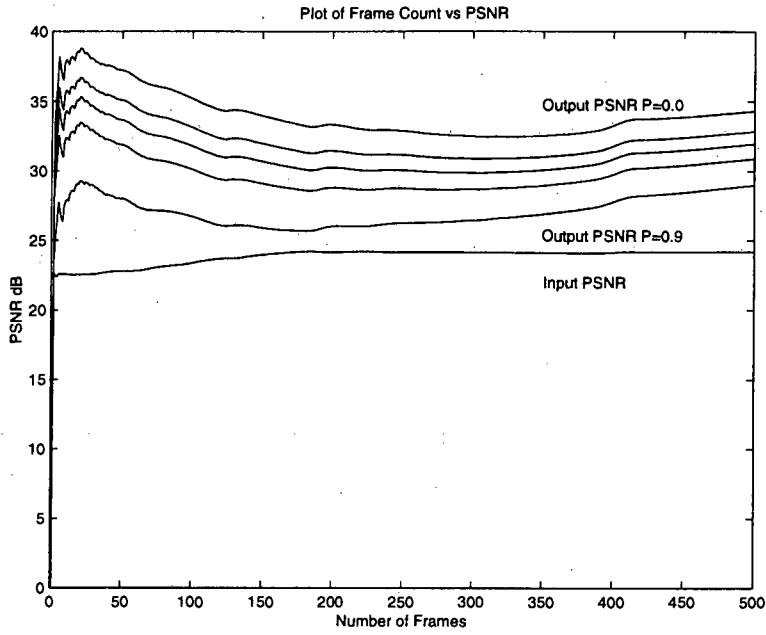


Figure A.2: Performance of Reference-Free Compensation Scheme on Short Day Sequence 2

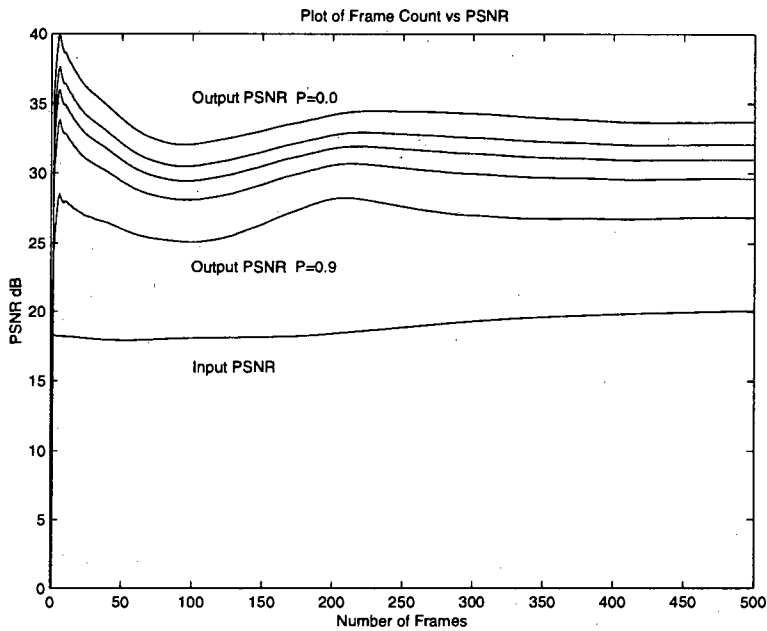


Figure A.3: Performance of Reference-Free Compensation Scheme on Short Day Sequence 3

APPENDIX A. GRAPHICAL RESULTS OBTAINED USING THE REFERENCE-FREE  
COMPENSATION ALGORITHM

---

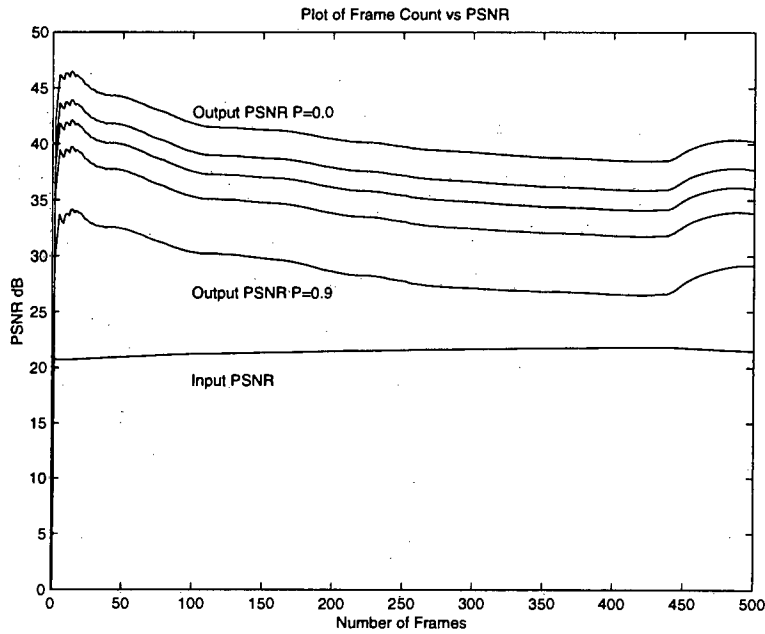


Figure A.4: Performance of Reference-Free Compensation Scheme on Short Day Sequence 4

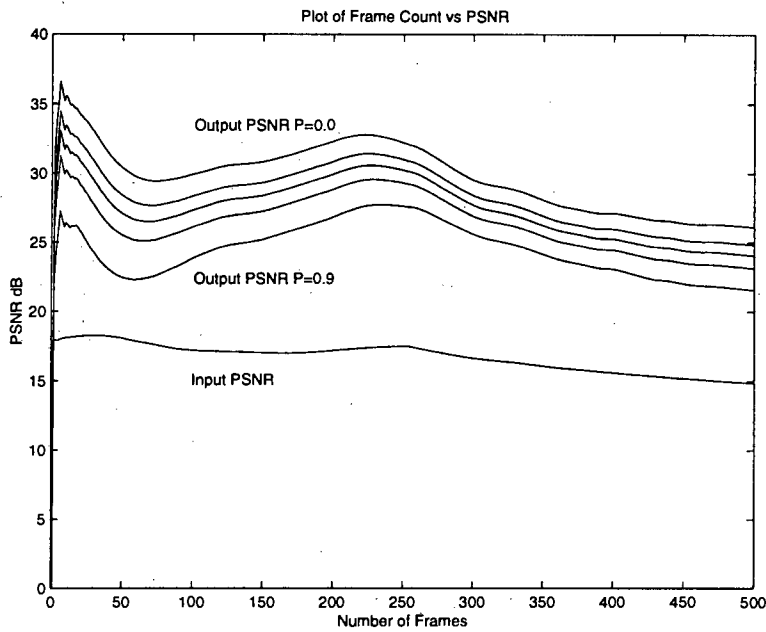


Figure A.5: Performance of Reference-Free Compensation Scheme on Short Night Sequence

APPENDIX A. GRAPHICAL RESULTS OBTAINED USING THE REFERENCE-FREE  
COMPENSATION ALGORITHM

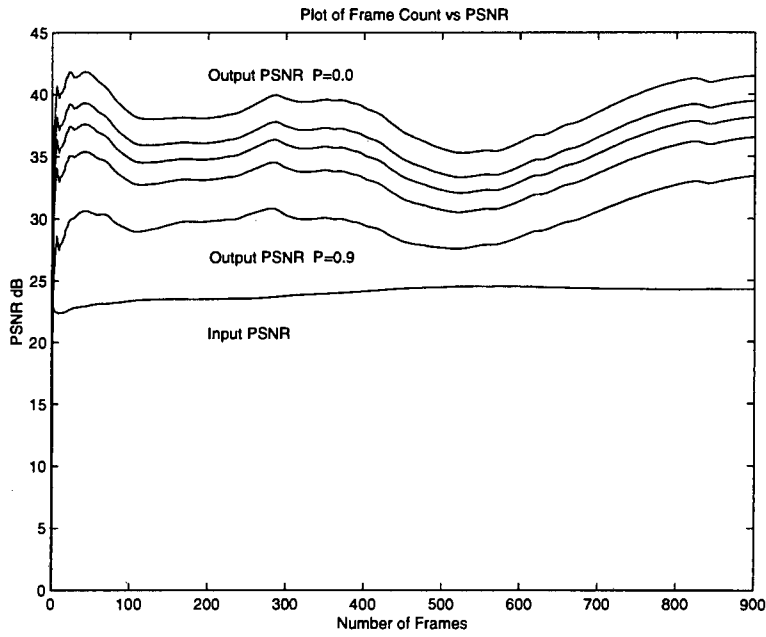


Figure A.6: Performance of Reference-Free Compensation Scheme on Long Day Sequence 1

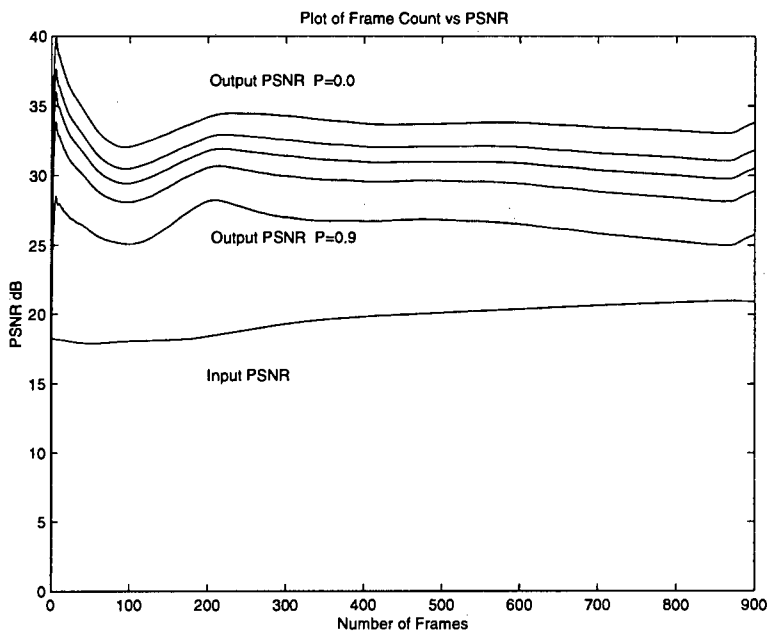


Figure A.7: Performance of Reference-Free Compensation Scheme on Long Day Sequence 2

APPENDIX A. GRAPHICAL RESULTS OBTAINED USING THE REFERENCE-FREE  
COMPENSATION ALGORITHM

---

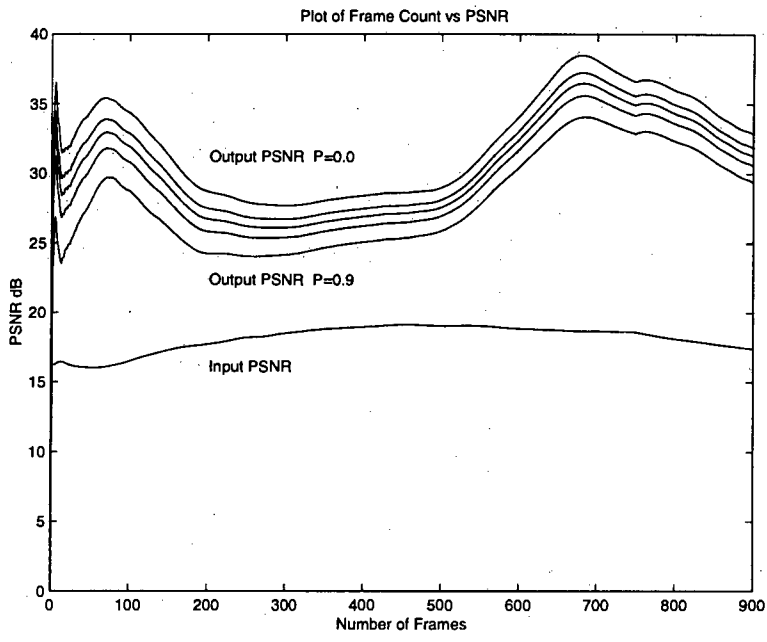


Figure A.8: Performance of Reference-Free Compensation Scheme on Long Night Sequence

## Appendix B

# Graphical Results Obtained using the Constant-Statistics Algorithm

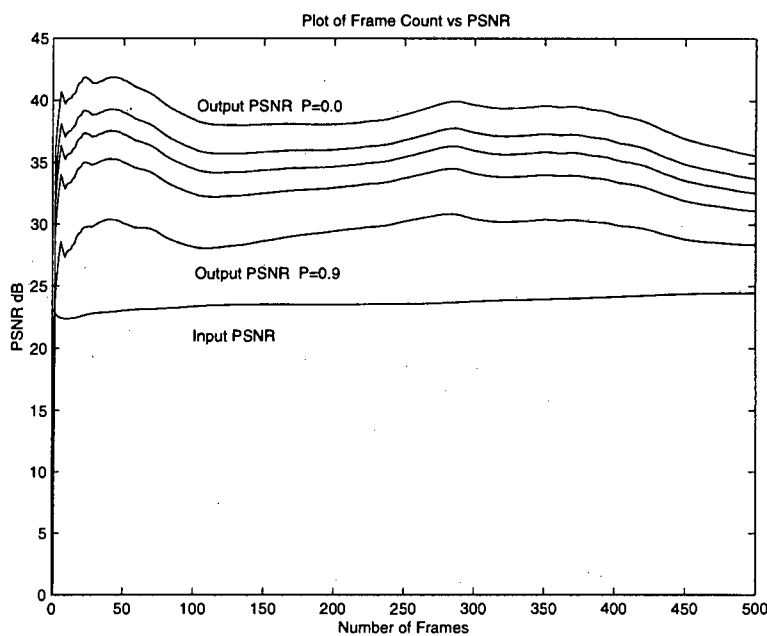


Figure B.1: Performance of Constant-Statistics Algorithm on Short Day Sequence 1

APPENDIX B. GRAPHICAL RESULTS OBTAINED USING THE  
CONSTANT-STATISTICS ALGORITHM

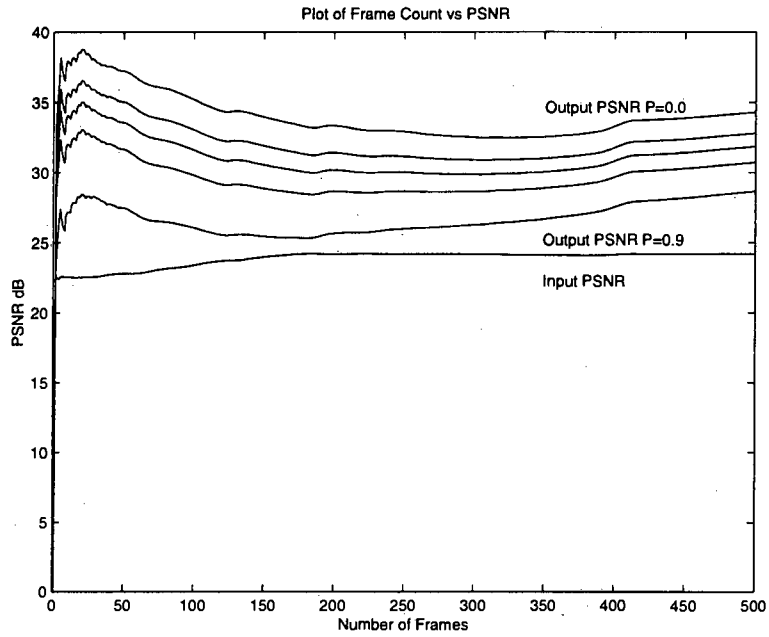


Figure B.2: Performance of Constant-Statistics Algorithm on Short Day Sequence 2

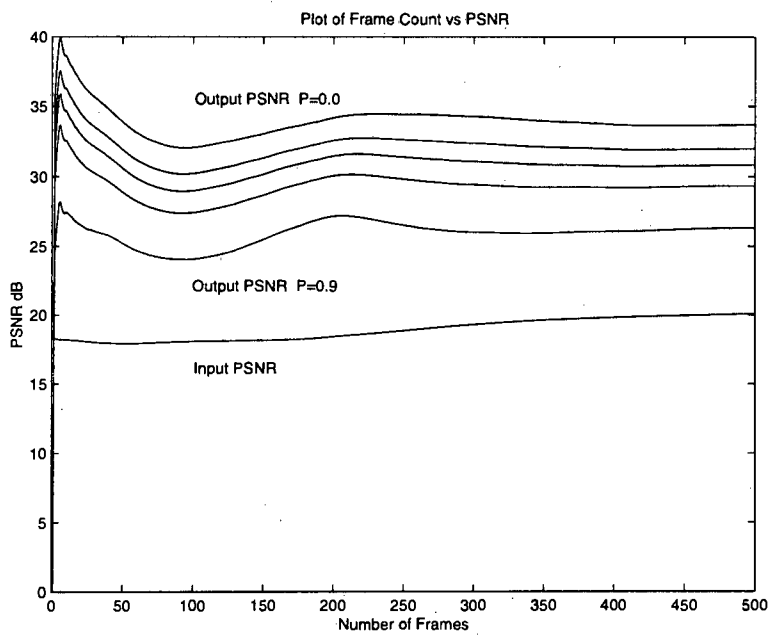


Figure B.3: Performance of Constant-Statistics Algorithm on Short Day Sequence 3

APPENDIX B. GRAPHICAL RESULTS OBTAINED USING THE  
CONSTANT-STATISTICS ALGORITHM

---

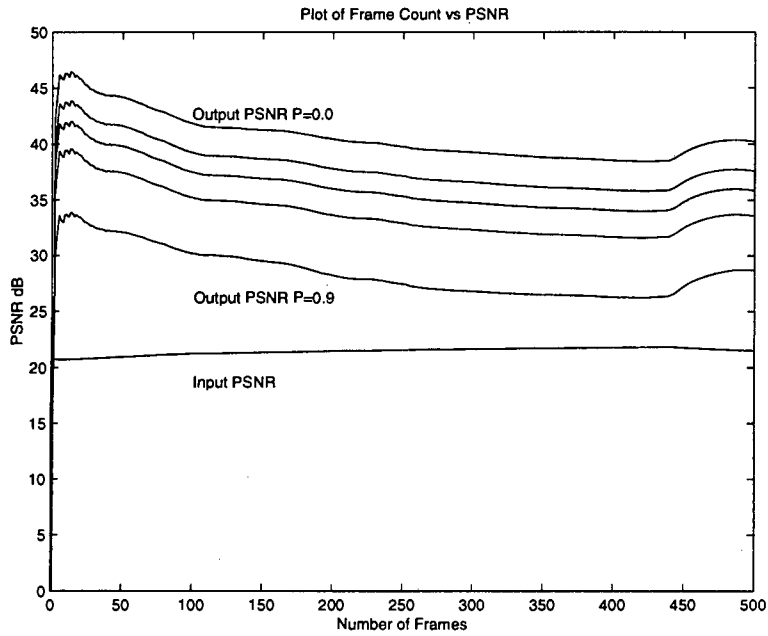


Figure B.4: Performance of Constant-Statistics Algorithm on Short Day Sequence 4

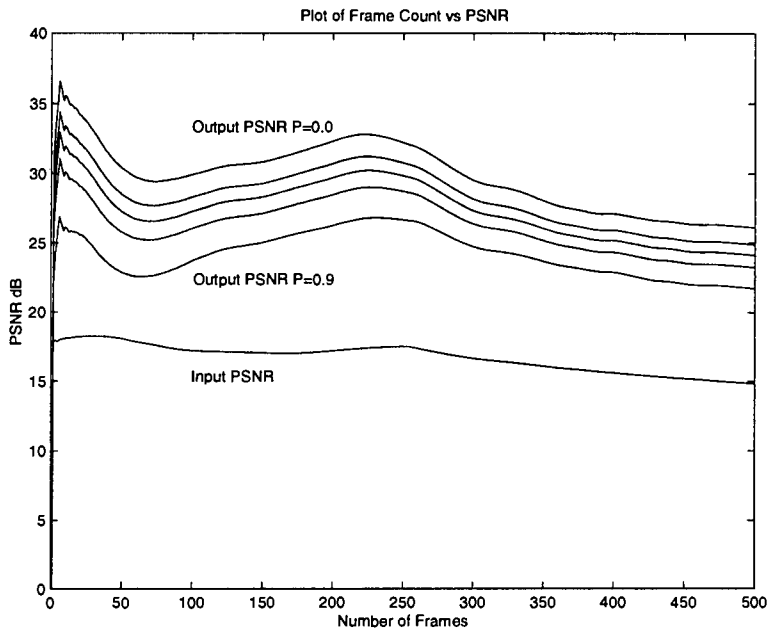


Figure B.5: Performance of Constant-Statistics Algorithm on Short Night Sequence

APPENDIX B. GRAPHICAL RESULTS OBTAINED USING THE  
CONSTANT-STATISTICS ALGORITHM

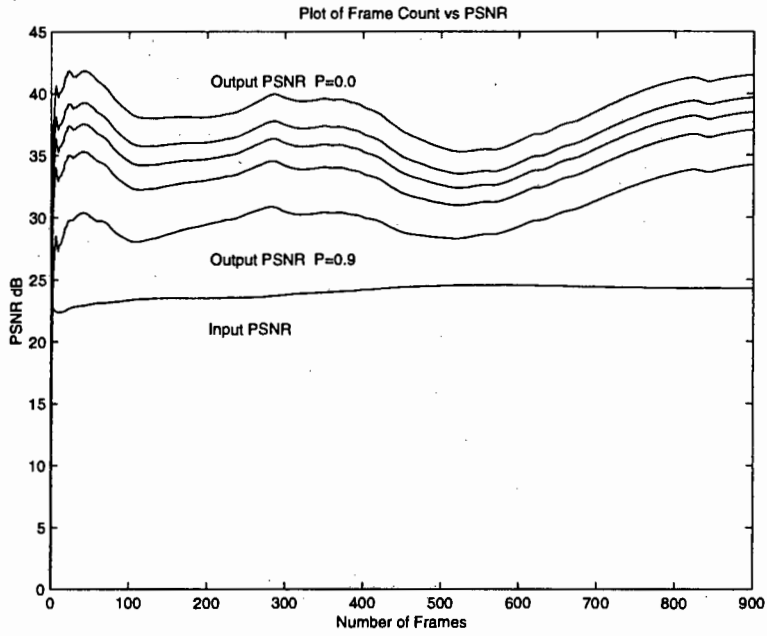


Figure B.6: Performance of Constant-Statistics Algorithm on Long Day Sequence 1

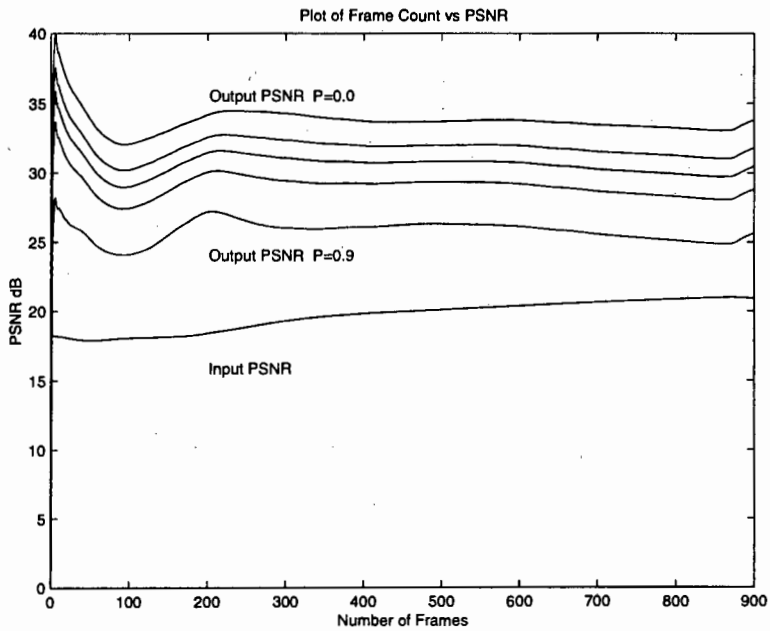


Figure B.7: Performance of Constant-Statistics Algorithm on Long Day Sequence 2

APPENDIX B. GRAPHICAL RESULTS OBTAINED USING THE  
CONSTANT-STATISTICS ALGORITHM

---

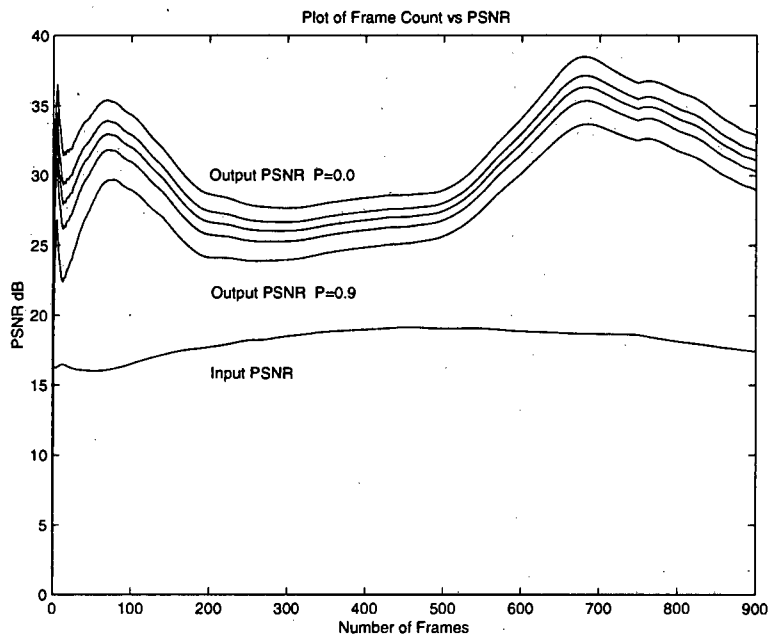


Figure B.8: Performance of Constant-Statistics Algorithm on Long Night Sequence

## Appendix C

# Graphical Results Obtained using the Fading-Memory Polynomial Filter with a Window Size of 20

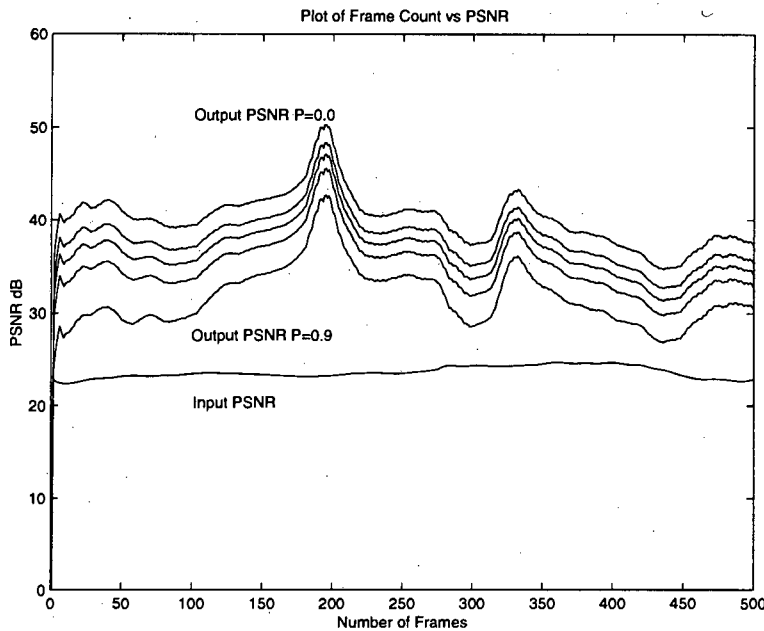


Figure C.1: Performance of Fading-Memory Polynomial Filter (Window Size = 20) on Short Day Sequence 1

APPENDIX C. GRAPHICAL RESULTS OBTAINED USING THE FADING-MEMORY POLYNOMIAL FILTER WITH A WINDOW SIZE OF 20

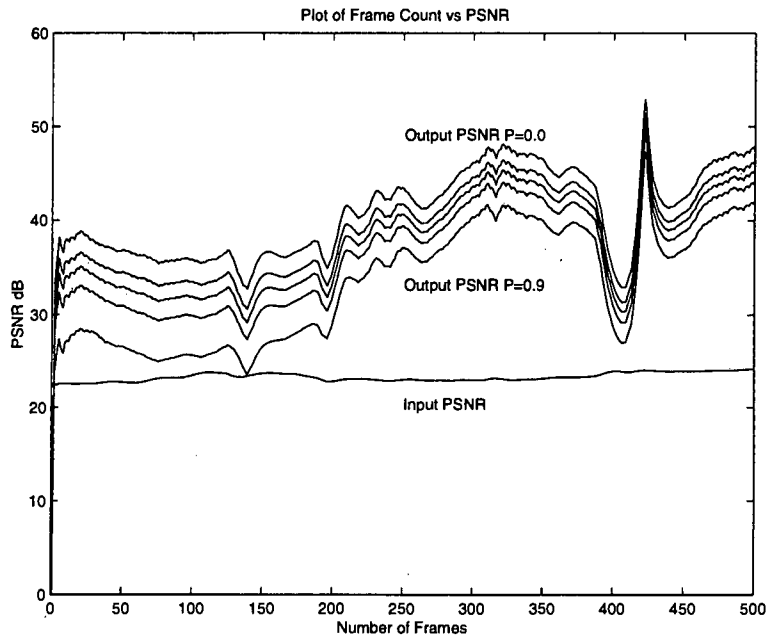


Figure C.2: Performance of Fading-Memory Polynomial Filter (Window Size = 20) on Short Day Sequence 2

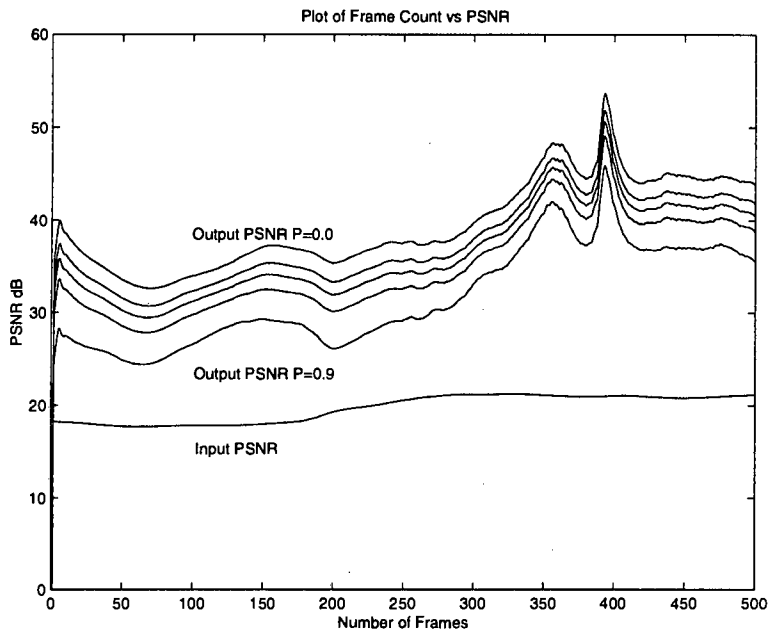


Figure C.3: Performance of Fading-Memory Polynomial Filter (Window Size = 20) on Short Day Sequence 3

APPENDIX C. GRAPHICAL RESULTS OBTAINED USING THE FADING-MEMORY POLYNOMIAL FILTER WITH A WINDOW SIZE OF 20

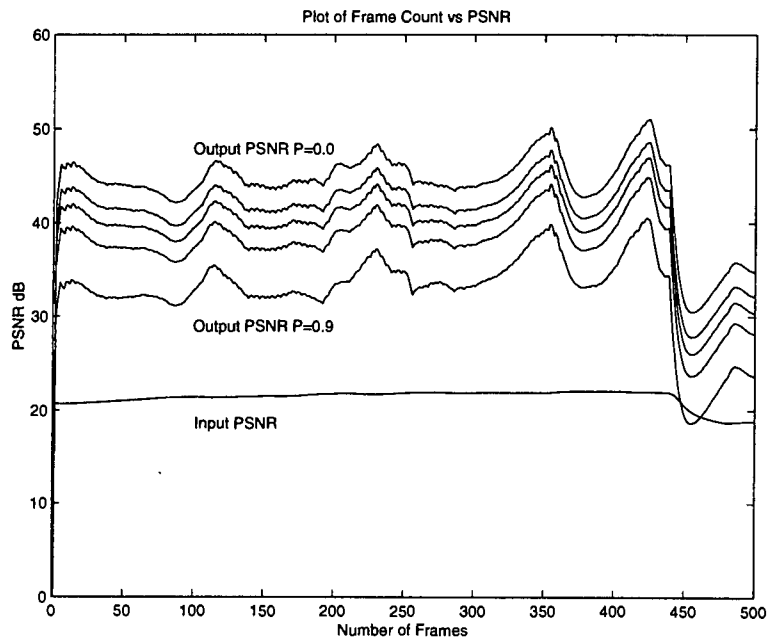


Figure C.4: Performance of Fading-Memory Polynomial Filter (Window Size = 20) on Short Day Sequence 4

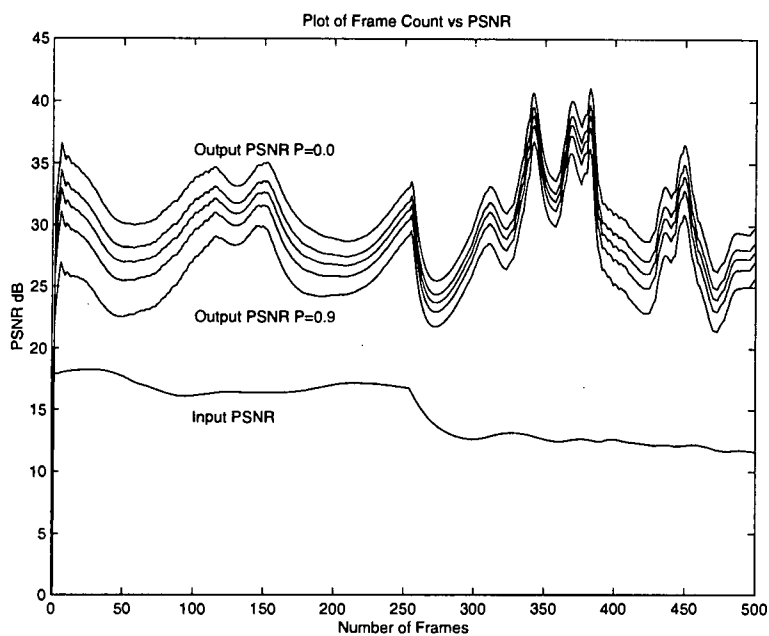


Figure C.5: Performance of Fading-Memory Polynomial Filter (Window Size = 20) on Short Night Sequence

APPENDIX C. GRAPHICAL RESULTS OBTAINED USING THE FADING-MEMORY  
POLYNOMIAL FILTER WITH A WINDOW SIZE OF 20

---

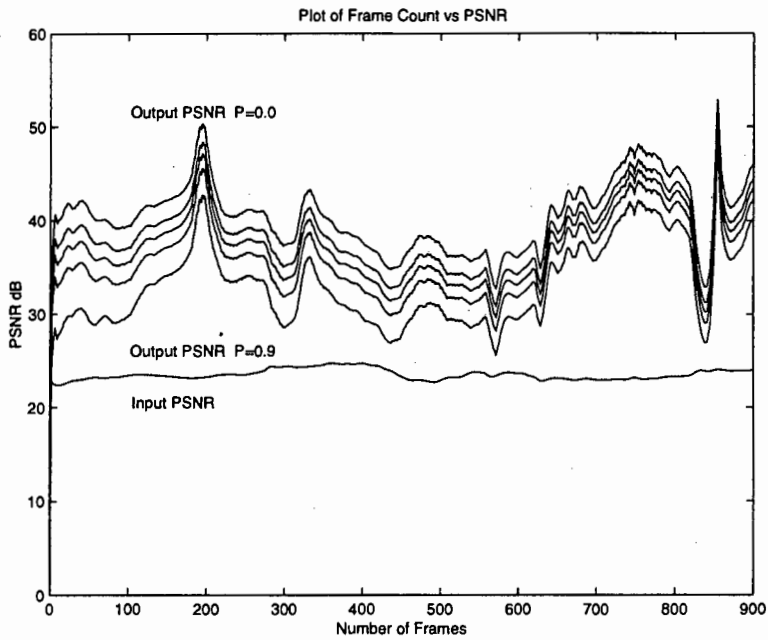


Figure C.6: Performance of Fading-Memory Polynomial Filter (Window Size = 20) on Long Day Sequence 1

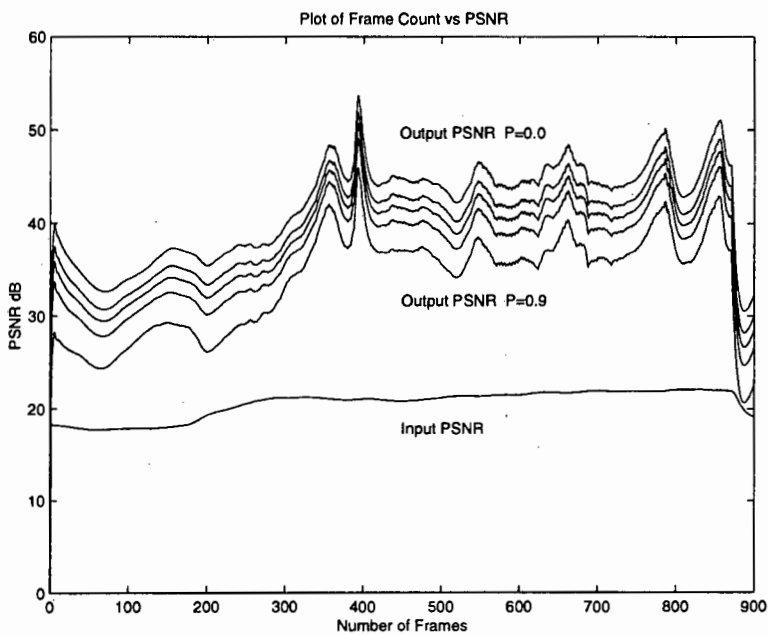


Figure C.7: Performance of Fading-Memory Polynomial Filter (Window Size = 20) on Long Day Sequence 2

APPENDIX C. GRAPHICAL RESULTS OBTAINED USING THE FADING-MEMORY  
POLYNOMIAL FILTER WITH A WINDOW SIZE OF 20

---

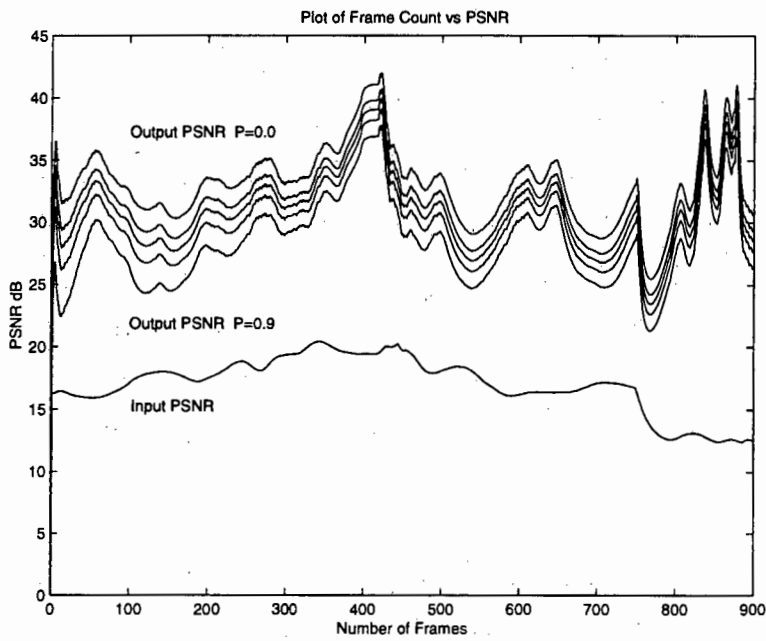


Figure C.8: Performance of Fading-Memory Polynomial Filter (Window Size = 20) on Long Night Sequence

## Appendix D

# Graphical Results Obtained using the Fading-Memory Polynomial Filter with a Window Size of 50

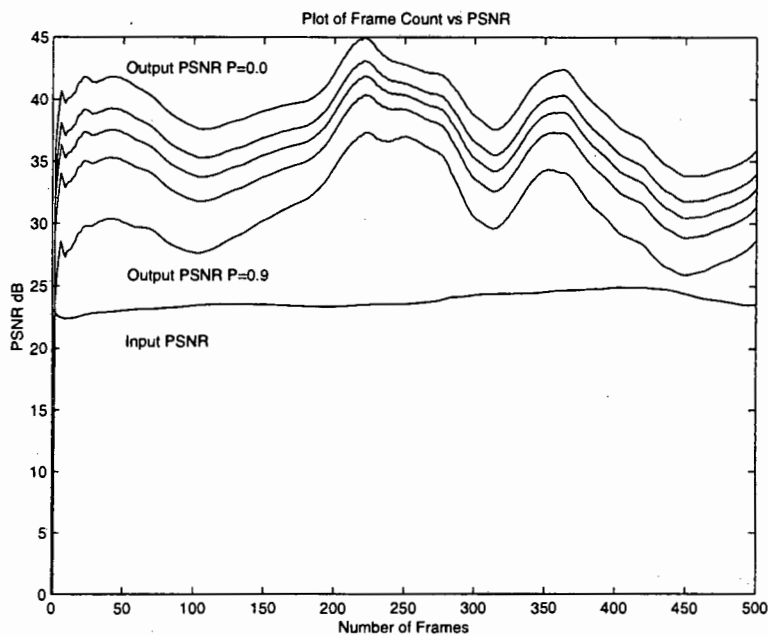


Figure D.1: Performance of Fading-Memory Polynomial Filter (Window Size = 50) on Short Day Sequence 1

APPENDIX D. GRAPHICAL RESULTS OBTAINED USING THE FADING-MEMORY POLYNOMIAL FILTER WITH A WINDOW SIZE OF 50

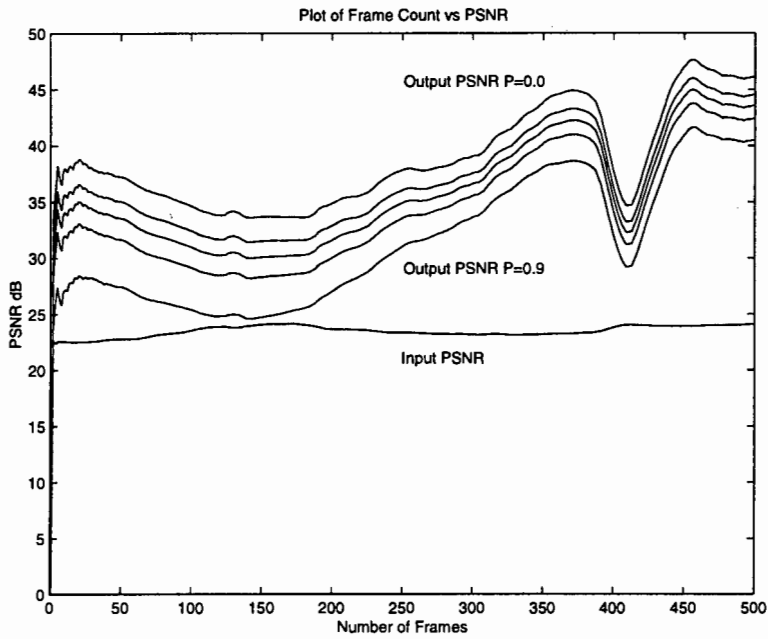


Figure D.2: Performance of Fading-Memory Polynomial Filter (Window Size = 50) on Short Day Sequence 2

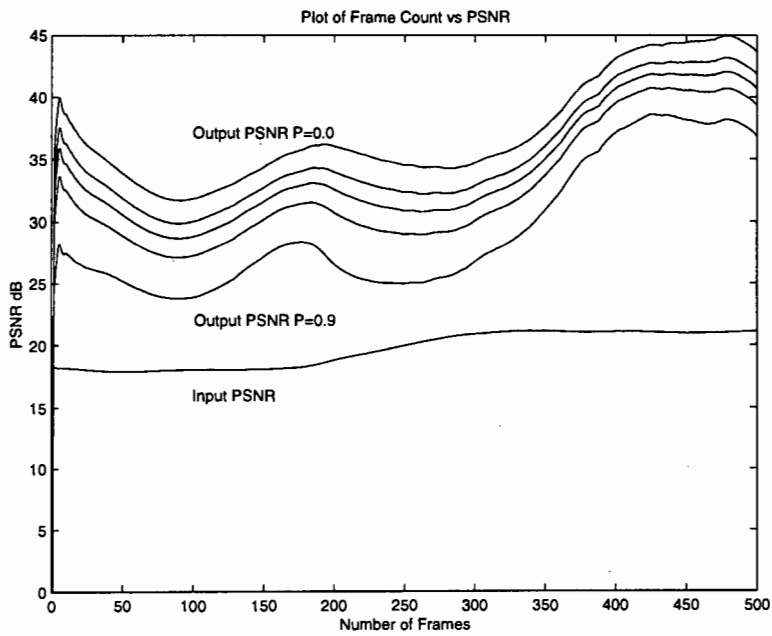


Figure D.3: Performance of Fading-Memory Polynomial Filter (Window Size = 50) on Short Day Sequence 3

APPENDIX D. GRAPHICAL RESULTS OBTAINED USING THE FADING-MEMORY POLYNOMIAL FILTER WITH A WINDOW SIZE OF 50

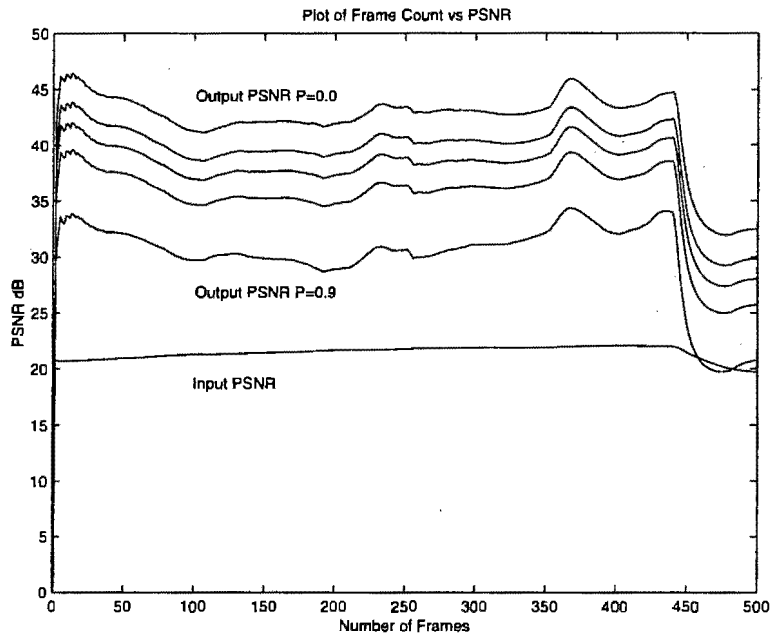


Figure D.4: Performance of Fading-Memory Polynomial Filter (Window Size = 50) on Short Day Sequence 4

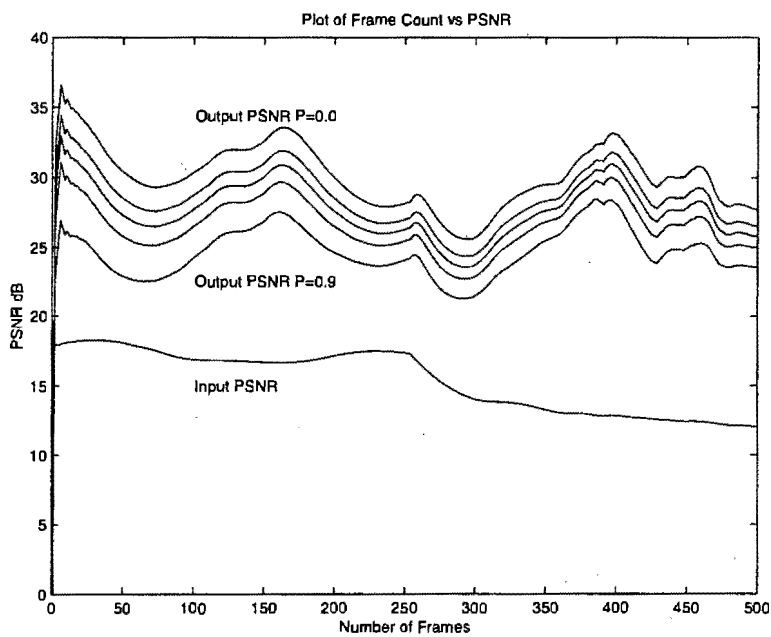


Figure D.5: Performance of Fading-Memory Polynomial Filter (Window Size = 50) on Short Night Sequence

APPENDIX D. GRAPHICAL RESULTS OBTAINED USING THE FADING-MEMORY POLYNOMIAL FILTER WITH A WINDOW SIZE OF 50

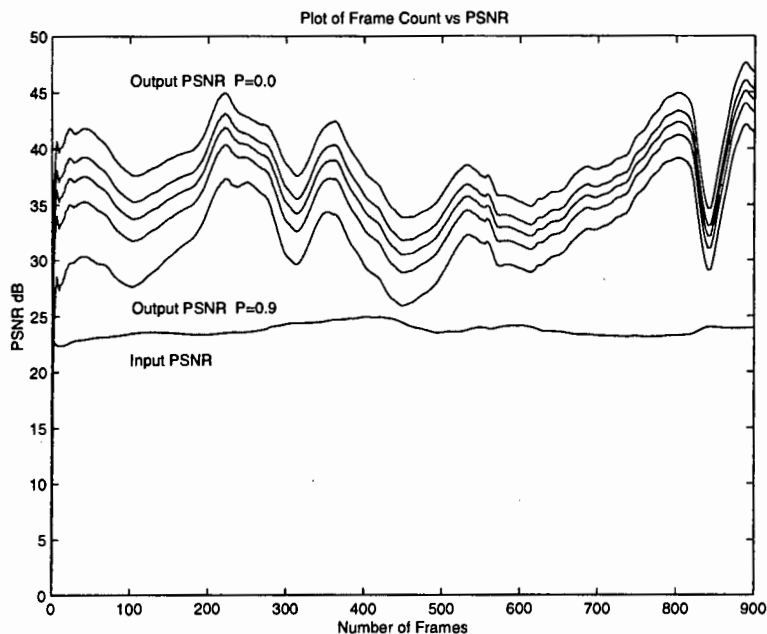


Figure D.6: Performance of Fading-Memory Polynomial Filter (Window Size = 50) on Long Day Sequence 1

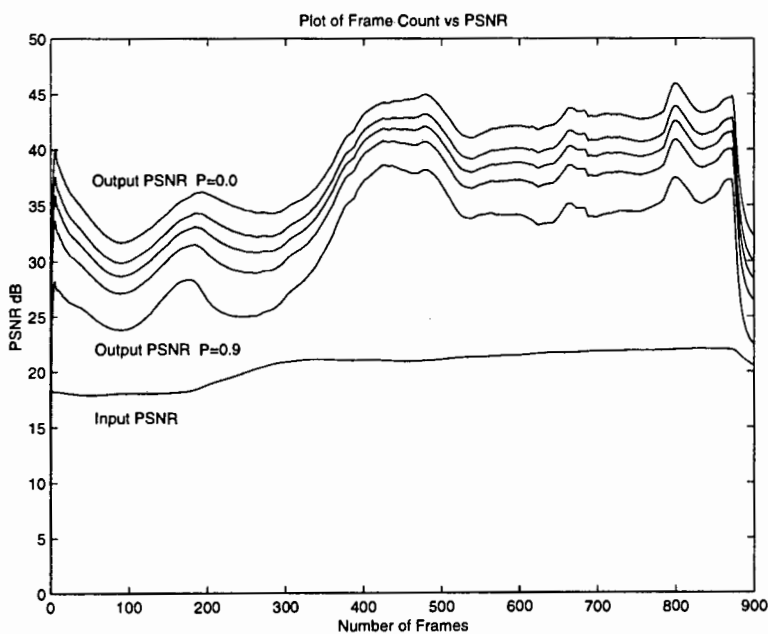


Figure D.7: Performance of Fading-Memory Polynomial Filter (Window Size = 50) on Long Day Sequence 2

APPENDIX D. GRAPHICAL RESULTS OBTAINED USING THE FADING-MEMORY  
POLYNOMIAL FILTER WITH A WINDOW SIZE OF 50

---

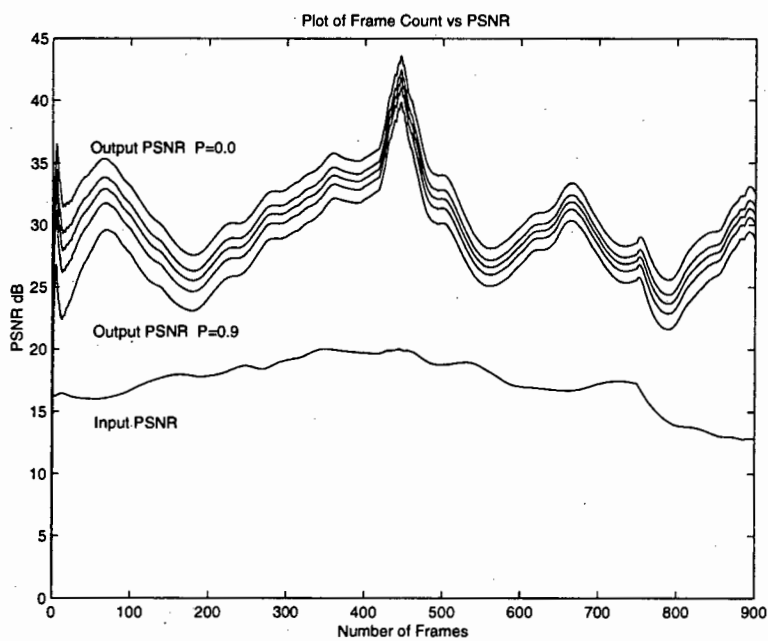


Figure D.8: Performance of Fading-Memory Polynomial Filter (Window Size = 50) on Long Night Sequence

## Appendix E

# Graphical Results Obtained using the Fading-Memory Polynomial Filter with a Window Size of 100

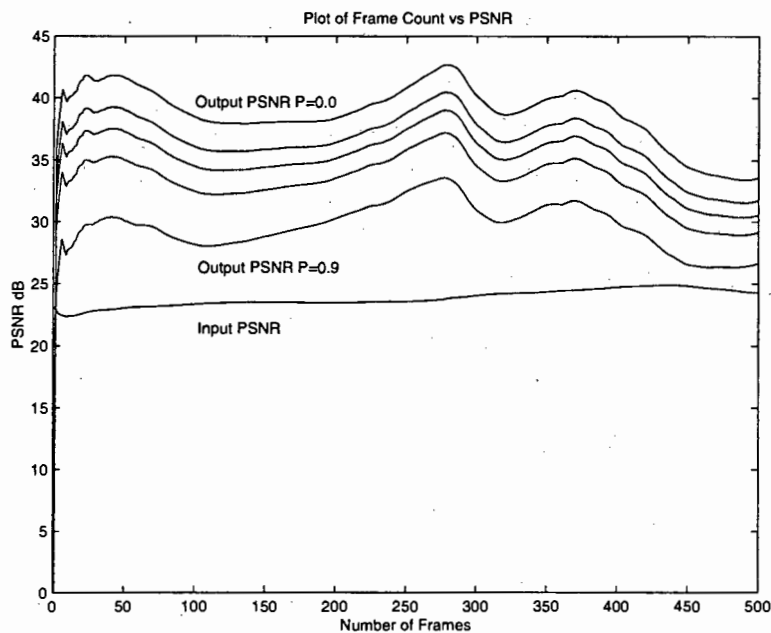


Figure E.1: Performance of Fading-Memory Polynomial Filter (Window Size = 100) on Short Day Sequence 1

APPENDIX E. GRAPHICAL RESULTS OBTAINED USING THE FADING-MEMORY POLYNOMIAL FILTER WITH A WINDOW SIZE OF 100

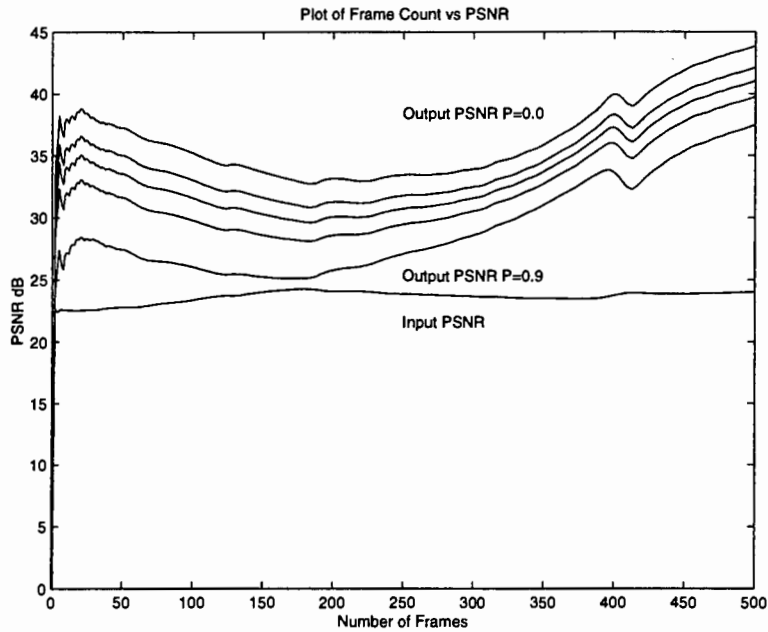


Figure E.2: Performance of Fading-Memory Polynomial Filter (Window Size = 100) on Short Day Sequence 2

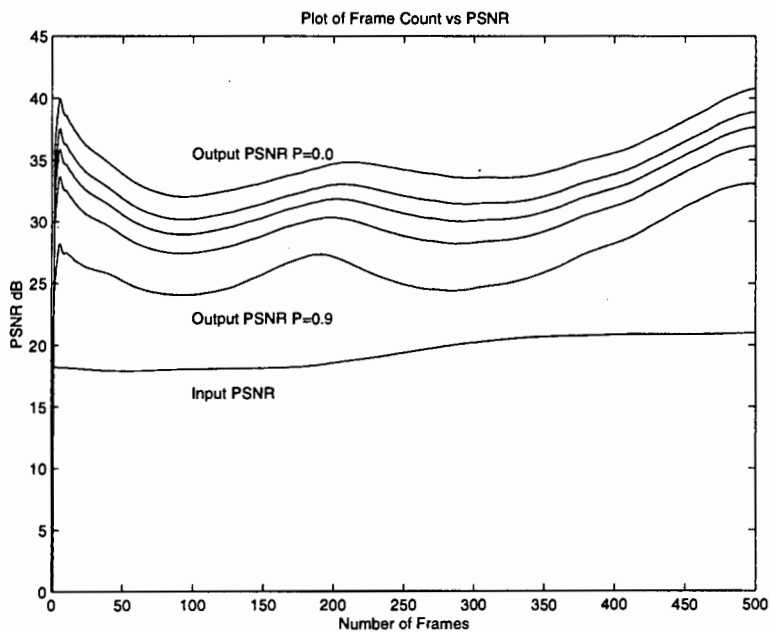


Figure E.3: Performance of Fading-Memory Polynomial Filter (Window Size = 100) on Short Day Sequence 3

APPENDIX E. GRAPHICAL RESULTS OBTAINED USING THE FADING-MEMORY POLYNOMIAL FILTER WITH A WINDOW SIZE OF 100

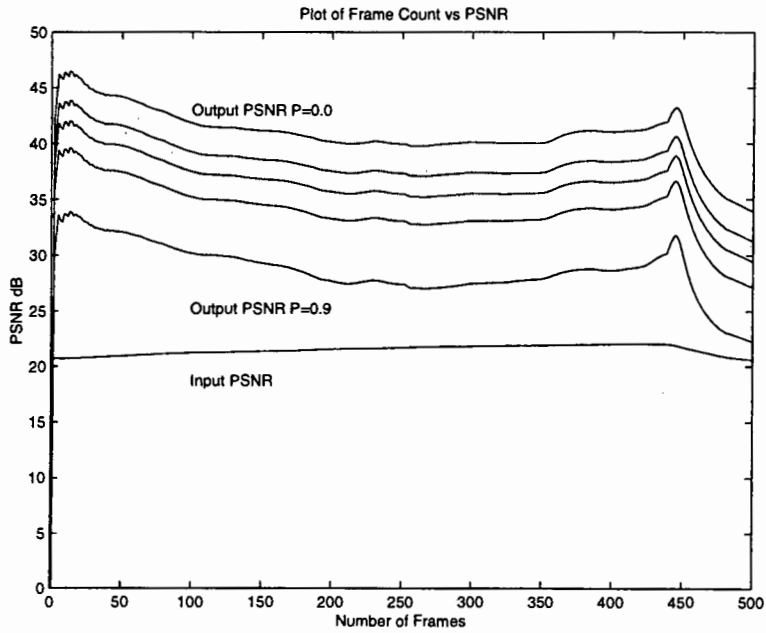


Figure E.4: Performance of Fading-Memory Polynomial Filter (Window Size = 100) on Short Day Sequence 4

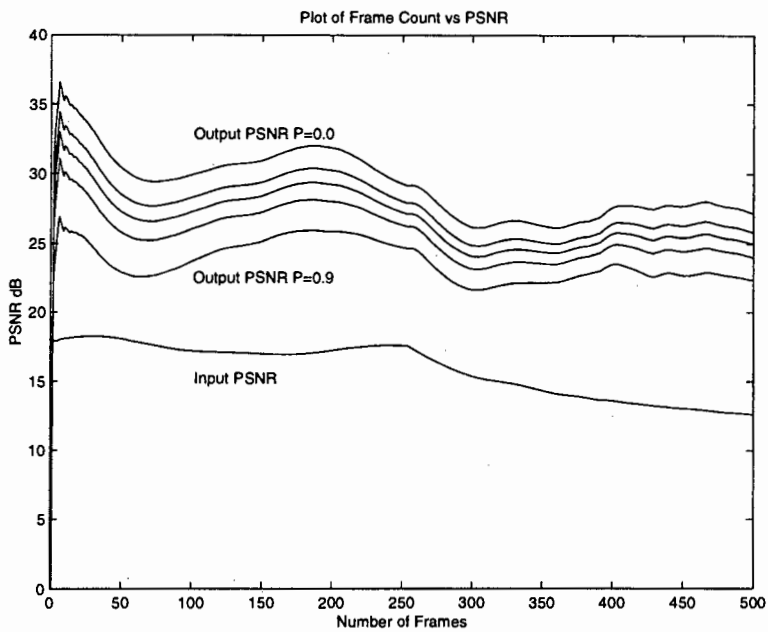


Figure E.5: Performance of Fading-Memory Polynomial Filter (Window Size = 100) on Short Night Sequence

APPENDIX E. GRAPHICAL RESULTS OBTAINED USING THE FADING-MEMORY POLYNOMIAL FILTER WITH A WINDOW SIZE OF 100

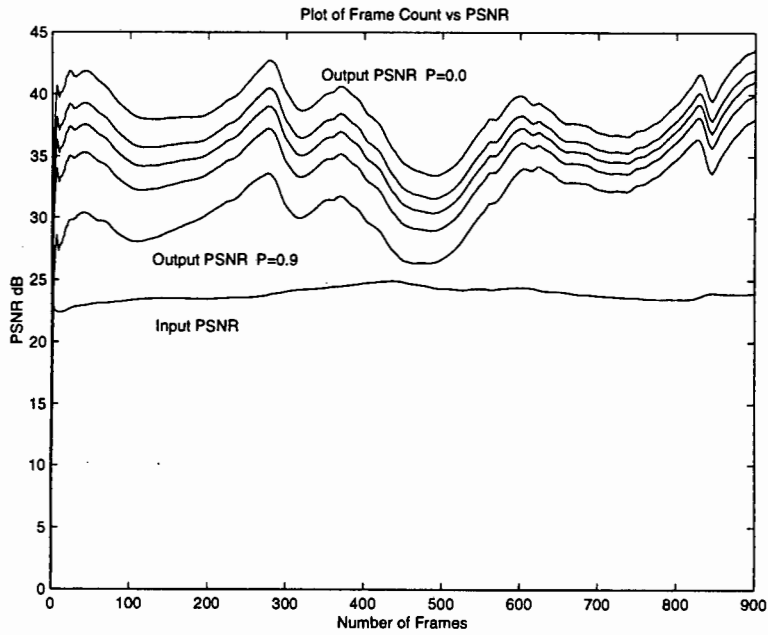


Figure E.6: Performance of Fading-Memory Polynomial Filter (Window Size = 100) on Long Day Sequence 1

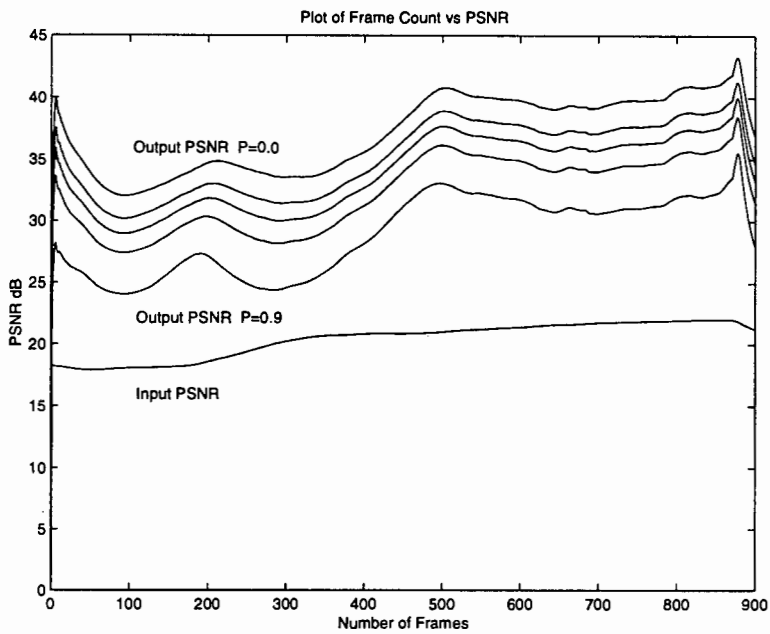


Figure E.7: Performance of Fading-Memory Polynomial Filter (Window Size = 100) on Long Day Sequence 2

APPENDIX E. GRAPHICAL RESULTS OBTAINED USING THE FADING-MEMORY  
POLYNOMIAL FILTER WITH A WINDOW SIZE OF 100

---

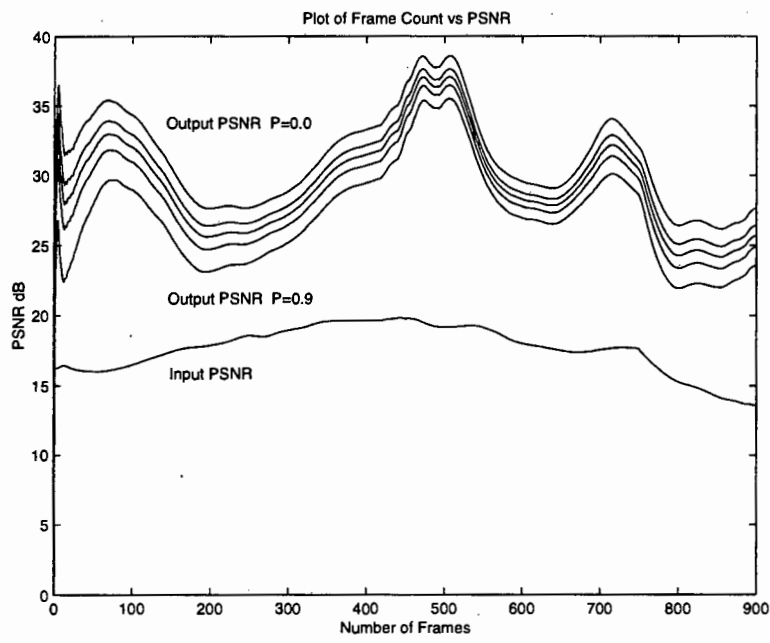


Figure E.8: Performance of Fading-Memory Polynomial Filter (Window Size = 100) on Long Night Sequence

## Appendix F

# Graphical Results Comparing the Peak Signal-to-Noise Ratios of the Output Image using Horizontal and Vertical Band Regions

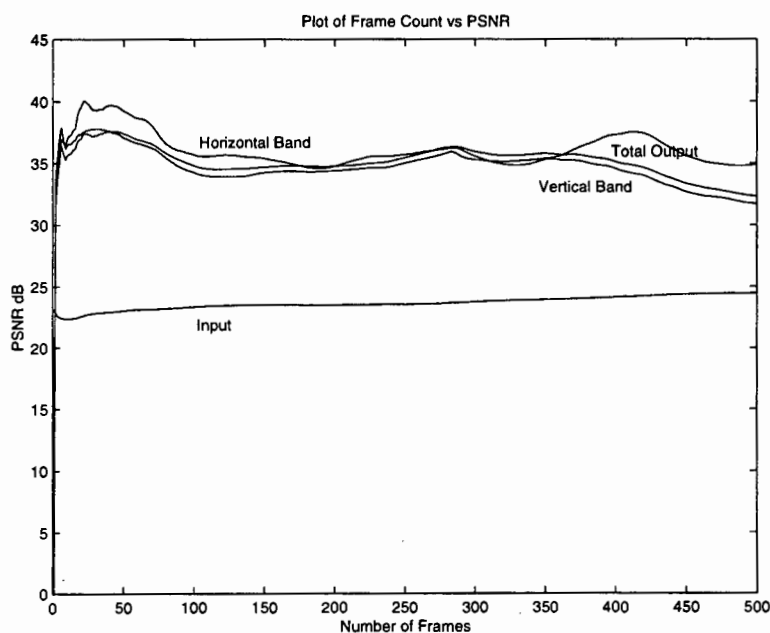


Figure F.1: PSNR of Output Image obtained using the Total Image as well as Horizontal and Vertical Band Regions for Short Day Sequence 1

APPENDIX F. GRAPHICAL RESULTS COMPARING THE PEAK SIGNAL-TO-NOISE RATIOS OF THE OUTPUT IMAGE USING HORIZONTAL AND VERTICAL BAND REGIONS

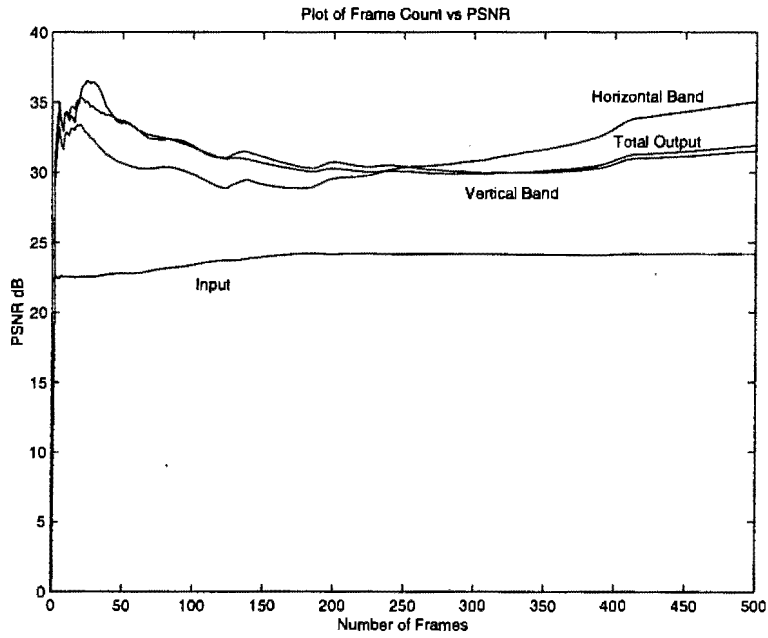


Figure F.2: PSNR of Output Image obtained using the Total Image as well as Horizontal and Vertical Band Regions for Short Day Sequence 2

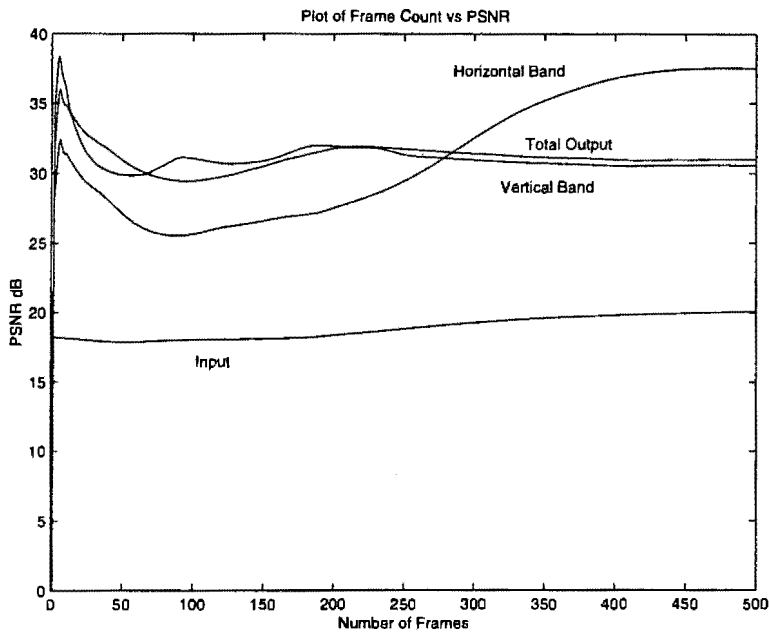


Figure F.3: PSNR of Output Image obtained using the Total Image as well as Horizontal and Vertical Band Regions for Short Day Sequence 3

APPENDIX F. GRAPHICAL RESULTS COMPARING THE PEAK SIGNAL-TO-NOISE RATIOS OF THE OUTPUT IMAGE USING HORIZONTAL AND VERTICAL BAND REGIONS

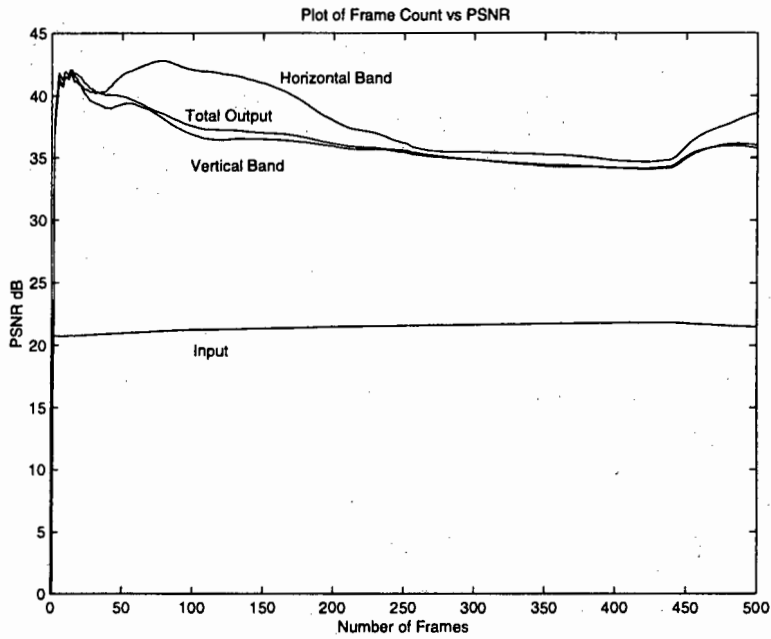


Figure F.4: PSNR of Output Image obtained using the Total Image as well as Horizontal and Vertical Band Regions for Short Day Sequence 4

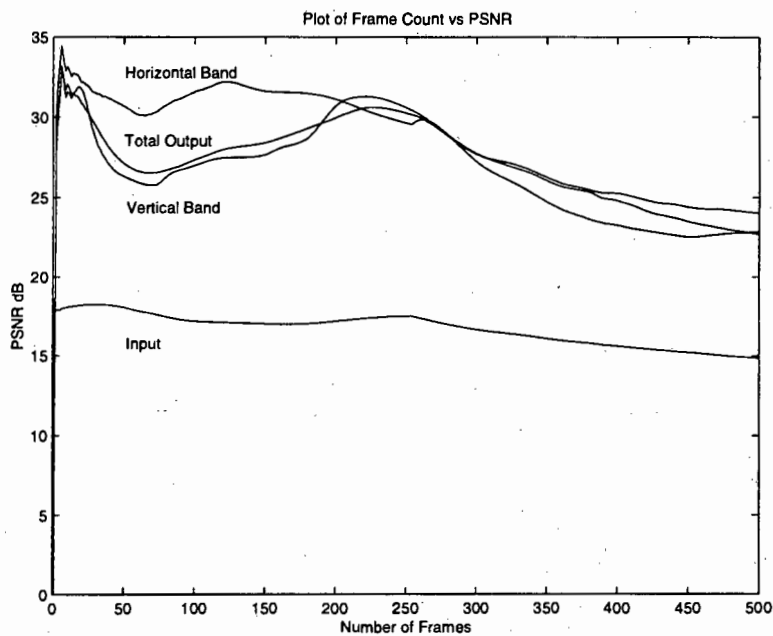


Figure F.5: PSNR of Output Image obtained using the Total Image as well as Horizontal and Vertical Band Regions for Short Night Sequence

APPENDIX F. GRAPHICAL RESULTS COMPARING THE PEAK SIGNAL-TO-NOISE RATIOS OF THE OUTPUT IMAGE USING HORIZONTAL AND VERTICAL BAND REGIONS

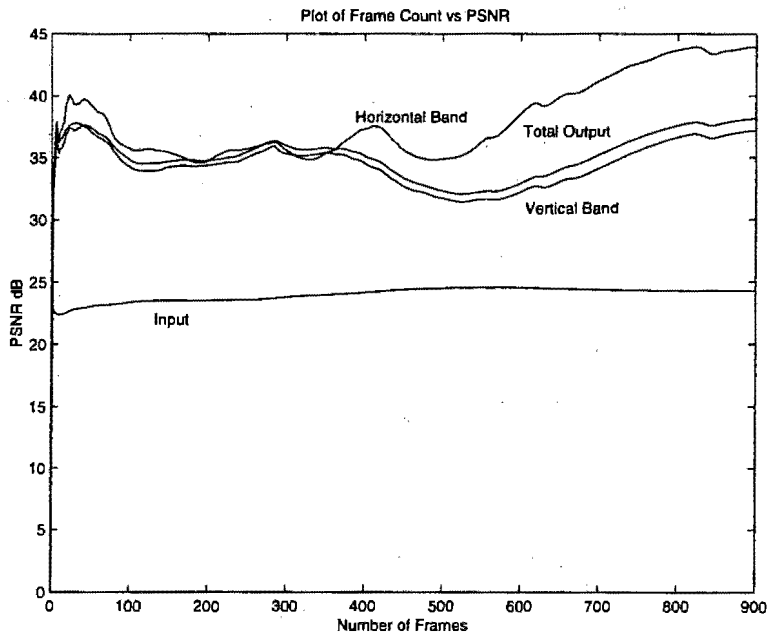


Figure F.6: PSNR of Output Image obtained using the Total Image as well as Horizontal and Vertical Band Regions for Long Day Sequence 1

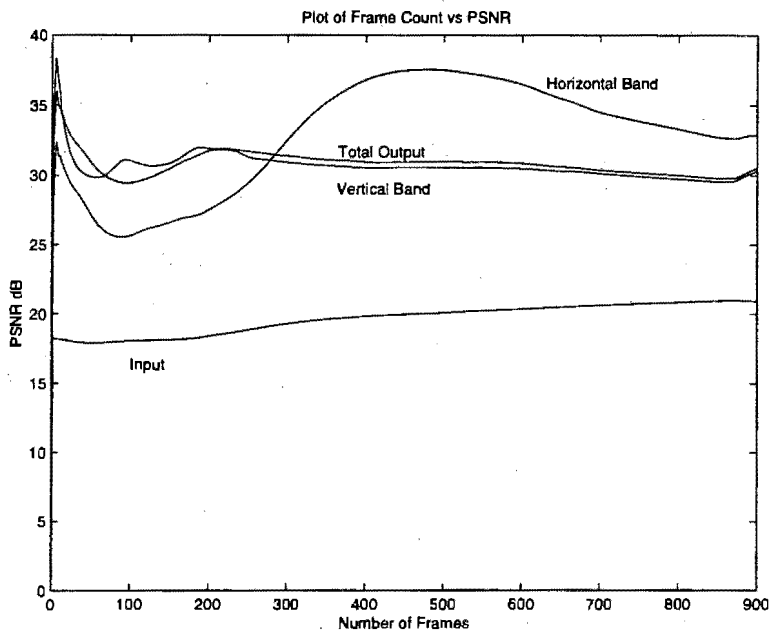


Figure F.7: PSNR of Output Image obtained using the Total Image as well as Horizontal and Vertical Band Regions for Long Day Sequence 2

APPENDIX F. GRAPHICAL RESULTS COMPARING THE PEAK SIGNAL-TO-NOISE RATIOS OF THE OUTPUT IMAGE USING HORIZONTAL AND VERTICAL BAND REGIONS

---

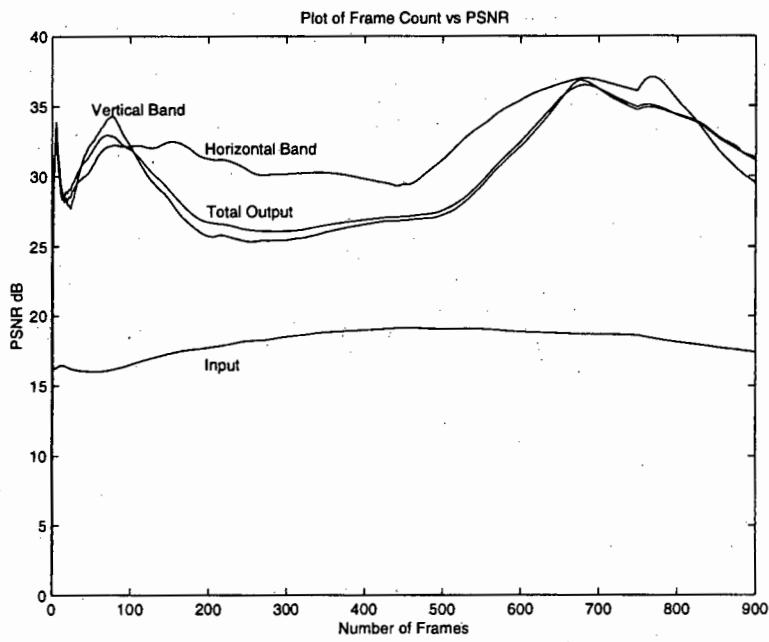


Figure F.8: PSNR of Output Image obtained using the Total Image as well as Horizontal and Vertical Band Regions for Long Night Sequence

## Appendix G

# True Input and Output Image PSNR compared to Time Averaged Input and Output Image PSNR

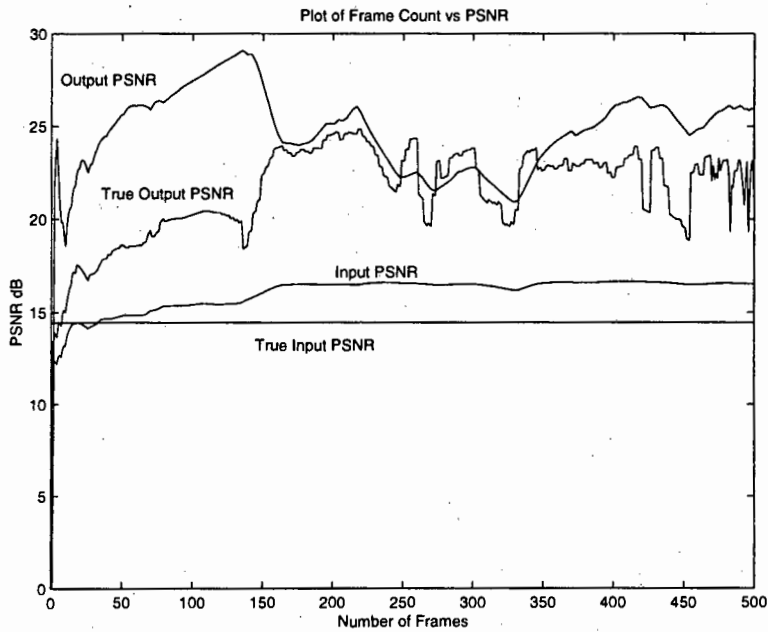


Figure G.1: True Input and True Output Image PSNR compared to Time Averaged Input and Output PSNR when Noise Fingerprint 1 is used

APPENDIX G. TRUE INPUT AND OUTPUT IMAGE PSNR COMPARED TO TIME  
AVERAGED INPUT AND OUTPUT IMAGE PSNR

---

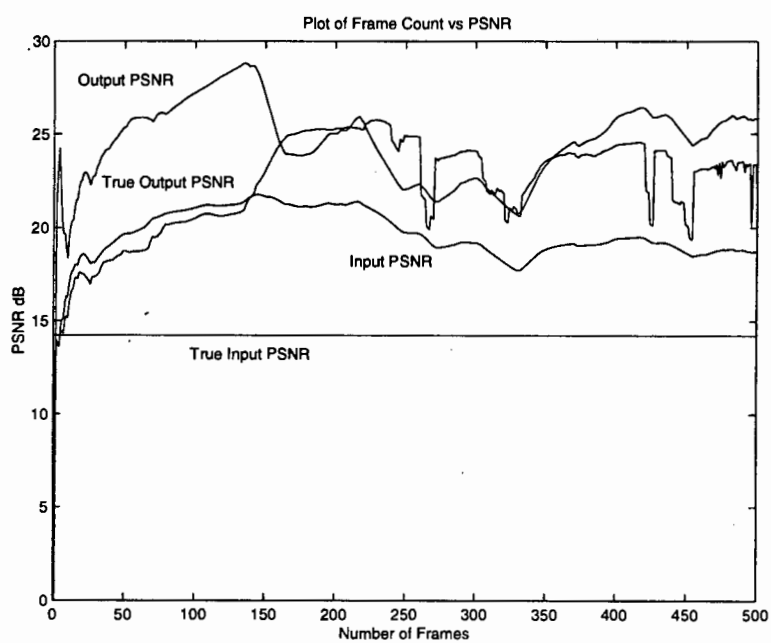


Figure G.2: True Input and True Output Image PSNR compared to Time Averaged Input and Output PSNR when Noise Fingerprint 2 is used

## Appendix H

# The CD-ROM

The CD-ROM contains

- Matlab Source Code for the Reference-Free Compensation Scheme, the Constant-Statistics Algorithm and the Fading-Memory Polynomial Filters.
- An Original Camera Sequence (jayv.avi) and the Compensated Sequence (cmpjv.avi). The compensation was performed using the Reference-Free Compensation Scheme with a  $P$  value of 0.5. Note that the original sequence is of resolution  $256 \times 256$  and the compensated sequence is of resolution  $128 \times 128$ .

# Fixed Pattern Noise Compensation in a Mercury Cadmium Telluride Infrared Focal Plane Array

by

**Praven Reddy**

Postgraduate Electrical Engineering Student  
Digital Image Processing Research Group  
Department of Electrical Engineering  
University of Cape Town

under the guidance of

**Professor Gerhard de Jager**

Digital Image Processing Research Group  
Department of Electrical Engineering  
University of Cape Town

30 September 1998

The University of Cape Town has been given  
the right to reproduce this thesis in whole  
or in part. Copyright is held by the author.

Prof B. Downing  
Department of Electrical Engineering  
University of Cape Town  
Rondebosch  
7700

P. Reddy  
1 Cathay View  
12 Devonshire Hill Road  
Rondebosch  
7701

Dear Sir

**Corrections to Minor Errors in Masters Dissertation**

I have corrected the minor errors in my masters dissertation and return the two unbound copies to you.

I include within this letter a summary of the corrected errors.

[1] indicates corrections that the internal examiner asked for.

[2] indicates corrections that the external examiner requested.

- Page xvi - The Stefan-Boltzmann constant has been changed to  $5.67 \times 10^{-8} \text{ W.m}^{-2}.\text{K}^{-4}$ . [2]
- Page 3 - The first sentence, second paragraph has been corrected to read "... and to determine if they offer adequate ..." instead of "... and to determine offer adequate ...". [2]
- Page 11 - The Stefan-Boltzmann constant has been changed to  $5.67 \times 10^{-8} \text{ W.m}^{-2}.\text{K}^{-4}$ . [2]
- Page 19 - Decimal point is used in Planck's constant instead of a comma. [2]
- Page 28 -  $D^*$  equation now reads  $D^* = (A_d \Delta F)^{1/2} / \text{NEP}$ . [2]
- Page 29 - Extra space after the word "amperage" in the last sentence has been deleted. [2]
- Page 36 - The second sentence, first paragraph now reads "... it is not able to directly drive ..." instead of "...it is not able directly drive ...". [2]
- Page 39 - The sixth sentence, second paragraph now reads "... The presence of spatial noise ..." instead of "... The presence spatial noise ...". [2]
- Page 61 - The first sentence, second paragraph now reads "... was operated during the day and at night with panning in ..." instead of "... was operated during the day and at night the day with panning in ...". [1] [2]
- Page 77 - *There may have been some confusion arising from the figure labels as the figure label in the previous sentence was also incorrect. I have corrected both these figure labels. The first sentence, third paragraph refers to Fig 6.6 (e) (instead of Fig. 6.6 (d)) and the second sentence, third paragraph refers to Fig. 6.5 (a) (instead of Fig 6.5 (e), which does not exist).* [2]
- Page 78 - The first sentence, last paragraph now reads "... this comparison was to see how well ..." instead of "... this comparison was see how well ...". [2]
- Page 99 - The first sentence, second paragraph now reads "... in Fig. 8.4 (b) through to Fig. 8.4 (f) ..." instead of "... in Fig. 4 (b) through to Fig. 4 (f) ...". [2]
- Page 101 - The first sentence, last paragraph now reads "... may be used to highlight ..." instead of "... may be used highlight ...". [2]
- Page 108 - Reference 31 now reads "... noise of IRCCD camera ..." instead of "... noise of irccd camera ...". [2]

I have also included a copy of the **Examiners Report** outlining the errors and the need for correction.

Yours faithfully  
Praven Reddy

MEMORANDUM

TO: J R Galvin  
Faculty Officer  
ENGINEERING

FROM: .....

---

MASTERS DISSERTATION OF: \_\_\_\_\_

I certify that the above candidate's dissertation has been amended to my satisfaction in accordance with the recommendations of the examiners. The two unbound copies of the dissertation are returned herewith and may now be deposited in the Library.

SIGNED: .....

DATE: ...../...../19.....

# UNIVERSITY OF CAPE TOWN - FACULTY OF ENGINEERING

109

MASTERS DEGREE CANDIDATE: P REDDY

REGISTRATION: MSC(ENG)      DEPARTMENT: ELECTRICAL ENGINEERING

DISSERTATION (FULL/HALF): HALF

FIXED PATTERN NOISE COMPENSATION IN A MERCURY CADMIUM TELLURIDE  
INFRARED FOCAL PLANE ARRAY

SUPERVISOR(S): 1) PROFESSOR G DE JAGER (2)

EXAMINERS:

INTERNAL:

PROFESSOR G DE JAGER

EXTERNAL:

DR W GUNTER  
INSTITUTE OF MARITIME TECHNOLOGY  
MARTELLO ROAD  
P O BOX 181  
SIMONSTOWN  
7995

COURSES COMPLETED:

REDDY, P MR		RDDPRA005																		
1997	ENGM01	CON																15.0	20.0	21.
		EEE502Z	OS	20.0	EEE506V	64 2-	3.0	EEE509Z	66 3 *	3.0	EEE512Z	55 3	3.0							
		EEE516Z	75 1	3.0	EEE584Z	74 2+	3.0	EEE590Z	67 3 *	3.0	EEE591Z	61 2-	3.0							
1998	ENGM01	BME202F	87 1	2.0	BME302F	72 2+	2.0	EEE502Z		20.0								4.0	19.0	

*\* changes on file.*

25

NOTES:

FACULTY OFFICE: ENGINEERING

fcovRED.doc

109(a)

UNIVERSITY OF CAPE TOWN : FACULTY OF ENGINEERING

EXAMINER'S REPORT ON MASTERS DISSERTATION

Section A: for office use

NAME OF CANDIDATE: REDDY, P

DISSERTATION TITLE: FIXED PATTERN NOISE COMPENSATION IN A MERCURY CADMIUM TELLURIDE INFRARED FOCAL PLANE ARRAY

DEPARTMENT: ELECTRICAL ENGINEERING

DEGREE FOR WHICH REGISTERED: MSC(ENG)

HALF DISSERTATION/FULL DISSERTATION: HALF

Section B: to be completed by the examiner

NAME GUNTER, N.H. POSITION HELD Senior Project Scientist

NAME OF INSTITUTION/ORGANISATION IMT

I have read the guidelines for examiners and have examined the dissertation accordingly.

I recommend (please tick the appropriate box) that:

- (a) the dissertation be passed;
(b) the dissertation be passed, but that minor corrections (e.g. spelling, typing, references, etc.) be made, to the satisfaction of the Examinations Board, before copies are lodged in the Library;
(c) the dissertation be passed only after significant changes (as identified within this report) are made to the satisfaction of the Examinations Board;
(d) although the dissertation does NOT meet the standard required for a pass, the candidate be invited to undertake further work, revise and submit it for re-examination;
(e) the dissertation be NOT passed.

It is the practice of the Faculty to make examiners' reports available to candidates after the Examinations Board meeting.

I DO NOT WISH MY NAME TO BE DISCLOSED TO THE CANDIDATE

I HAVE NO OBJECTION TO MY NAME BEING DISCLOSED TO THE CANDIDATE

My full report follows overleaf:

SIGNED: DATE: 27 November 1998

c:\forms\massexrc.doc

109(b)

GUNTER - Examiner Report - P Reddy

**Examiner Report on Masters Dissertation of P Reddy: Fixed Pattern Noise Compensation in a Mercury Cadmium Telluride Infrared Focal Plane Array**

**Examiner: Dr. W H Gunter, IMT (Simon's Town)**

**Evaluation of Dissertation**

**1. Meeting of Requirements**

Examination of this dissertation (and CD-ROM) has convinced me that the work conducted by Mr. Reddy satisfies all the requirements with regard to a Degree of Master namely:

- That he understands the nature and purpose of the dissertation.
- That he has an adequate acquaintance with the relevant literature.
- That he has mastered the relevant techniques and understands the scientific methods.
- That he is capable of independent thought and making of sound deductions.

**2. Minor Corrections**

I recommend that the following minor corrections be made before the final dissertation is issued:

- Page xvi - The Stefan-Boltzman constant should be  $5.67 \times 10^{-8} \text{ W.m}^{-2}.\text{K}^{-4}$
- Page 3 - The first sentence, second paragraph should read "... and to determine if they offer adequate ..."
- Page 11 - The Stefan-Boltzman constant should be  $5.67 \times 10^{-8} \text{ W.m}^{-2}.\text{K}^{-4}$
- Page 19 - Decimal comma iso point is used in Planck's constant.
- Page 28 -  $D^*$  equation should read
 
$$D^* = (A_d \times \Delta F)^{1/2} / \text{NEP}$$
- Page 29 - Last sentence on page, extra space after "amperage"
- Page 36 - The second sentence, first paragraph should read "... it is not able to directly drive ..."
- Page 39 - The sixth sentence, second paragraph should read "... The presence of spatial noise ..."
- Page 61 - The first sentence, second paragraph should read "...was operated during the day and at night with panning in ..."
- Page 77 - The second sentence, third paragraph should read "... shown in Fig. 6.6 (e). ..."
- Page 78 - The first sentence, last paragraph should read "... this comparison was to see how well ..."
- Page 99 - The first sentence, second paragraph should read "... in Fig. 8.4(b) through to Fig. 8.4(f) ..."

109(c)

GUNTER-Examiner Report - P Reddy

- Page 101 - The first sentence, last paragraph should read " ... may be used to highlight ..."
- Page 108 - Reference [32] should read " ... noise of IRCCD camera ..."

3. General Comments

- It would have been an advantage if direct digitization of the infrared video was possible in stead of storing the data on videotape. This would have eliminated signal degradation due to the storage/playback from magnetic tape.
- If cost-effective implementation of these techniques can be achieved for real time system applications then there should be a significant military/civilian market.

4. Recommendation

I recommend that the dissertation be passed, but that minor corrections are made (see par. 2).

Signed: .....

Date: 27/11/98

UNIVERSITY OF CAPE TOWN : FACULTY OF ENGINEERING

EXAMINER'S REPORT ON MASTERS DISSERTATION

Section A: for office use

110

NAME OF CANDIDATE: P REDDY

DISSERTATION TITLE: FIXED PATTERN NOISE COMPENSATION IN A MERCURY  
CADMIUM TELLURIDE INFRARED FOCAL PLANE ARRAY.

DEPARTMENT: ELECTRICAL ENGINEERING

DEGREE FOR WHICH REGISTERED: MSC (ENG)

HALF DISSERTATION/FULL DISSERTATION: HALF

Section B: to be completed by the examiner

NAME G DE JAGER POSITION HELD PROFESSOR

NAME OF INSTITUTION/ORGANISATION UCT

I have read the guidelines for examiners and have examined the dissertation accordingly.

I recommend (please tick the appropriate box) that:

- (a) the dissertation be passed;
- (b) the dissertation be passed, but that minor corrections (e.g. spelling, typing, references, etc.) be made, to the satisfaction of the Examinations Board, before copies are lodged in the Library;
- (c) the dissertation be passed only after significant changes (as identified within this report) are made to the satisfaction of the Examinations Board;
- (d) although the dissertation does NOT meet the standard required for a pass, the candidate be invited to undertake further work, revise and submit it for re-examination;
- (e) the dissertation be NOT passed.

It is the practice of the Faculty to make examiners' reports available to candidates after the Examinations Board meeting.

I DO NOT WISH MY NAME TO BE DISCLOSED TO THE CANDIDATE

I HAVE NO OBJECTION TO MY NAME BEING DISCLOSED TO THE CANDIDATE

My full report follows overleaf:

SIGNED: ..... DATE: 29/11/98

\*10 11:10/21/ MON, 23 NOV 1998 11:55:55 T0100 (MST)  
\*Message-ID: <36593BCF.2FD6F216@esat.kuleuven.ac.be>  
Date: Mon, 23 Nov 1998 11:41:19 +0100  
From: Gerhard de Jager <Gerhard.dejager@esat.kuleuven.ac.be>  
Organization: KU Leuven  
X-Mailer: Mozilla 4.5 [en] (Win98; I)  
X-Accept-Language: en  
MIME-Version: 1.0  
To: engaes@engfac.uct.ac.za  
Subject: Hi Ann Reddy report  
Content-Type: text/plain; charset=us-ascii  
Content-Transfer-Encoding: 7bit  
X-PMFLAGS: 34078848

///  
DE JAGER : REDDY

Report on the MSc thesis

Fixed Pattern Noise Compensation in a Mercury Cadmium Telluride Infrared focal plane array.

By Praven Reddy

=====  
All infrared imaging devices suffer from a non-uniform image output even when the input to the device is a uniform grey field, the "fixed pattern noise". This thesis investigates methods of compensating for this fixed pattern noise and proposes improvements on the existing techniques. These suggestions lead to significantly better signal to noise ratios and should be published.

After introducing the problem in chapter 1, the general field of infrared radiation and thermal imaging is surveyed in chapter 2 in perhaps too much detail. The description of mercury cadmium telluride detectors presented here is very clear. The infrared camera system used in the present investigation is described in detail in chapter 3, after which noise mechanisms, both temporal and spatial, is discussed in chapter 4.

Single point compensation for non-uniformities in sensitivity between pixels in the detector, two point compensation and multipoint schemes are then discussed in chapter 5. The main area of investigation of the thesis, reference free compensation schemes, are then discussed in detail and the properties of the fading memory polynomial filter is presented. Chapter 6 presents detailed experiments performed on a number of infrared sequences; chapter 7 presents the results and in chapter 8 these results are discussed in detail. Chapter 9 summarises the results and provides some recommendations.

The thesis presents much original material that is worthy of publication. In particular, the application of the fading memory polynomial filter is shown to lead to greater improvements in signal to noise ratio and image quality than the other methods. The report goes even further in that it evaluates the way in which image quality is assessed and discusses this in detail.

The thesis is clearly written, provides an exhaustive review of all the relevant literature, is well presented and satisfies all the requirements for the degree.

I recommend the award of the degree.

I have found only one typographical error on page 61 line 13: "... during the day and at night [the day] with panning in horizontal ... "

Gerhard de Jager  
20 November 1998

# UNIVERSITY OF CAPE TOWN - FACULTY OF ENGINEERING

## MASTERS DEGREE REQUIREMENTS: EVIDENCE OF SUBMISSION OF A PAPER FOR PRESENTATION AT A CONFERENCE OR PUBLICATION IN A JOURNAL RECOGNISED BY SENATE

This form is to be completed by the candidate and the supervisor and submitted to the Faculty Officer by not later than 30 May in the case of a candidate hoping to graduate in June or 25 November in the case of a candidate hoping to graduate in December.

112

1. NAME OF CANDIDATE: REDDY, P
2. MASTERS DEGREE FOR WHICH REGISTERED: MSC(ENG)
3. DEPARTMENT: ELECTRICAL ENGINEERING
4. DISSERTATION (STATE TITLE AND INDICATE WHETHER HALF OR FULL DISSERTATION)  
HALF/FULL: HALF

TITLE: FIXED PATTERN NOISE COMPENSATION IN A MERCURY CADMIUM TELLURIDE INFRARED FOCAL PLANE ARRAY

COMPLETE EITHER 5 OR 6 BELOW

### 5. DETAILS OF CONFERENCE FOR WHICH PAPER WAS PREPARED :

- (i) NAME OF CONFERENCE Proceedings of the 1998 South African Symposium on Communications and Signal Processing (COMSIG '98)
- (ii) DATE OF CONFERENCE 7-8 September 1998
- (iii) VENUE OF CONFERENCE UCT
- (iv) TITLE OF PAPER Reference Free Nonuniformity Correction for Mercury Cadmium Telluride Infrared Focal Plan Arrays
- (v) HAS THE PAPER BEEN ACCEPTED FOR PRESENTATION?..... Yes
- (vi) HAS THE PAPER BEEN PRESENTED TO THE CONFERENCE?..... Yes

NB: ATTACH A COPY OF THE PAPER PAPER ON FILE IN F10.

### 6. NAME OF JOURNAL FOR WHICH PAPER WAS PREPARED:

- (i) NAME OF JOURNAL.....
- (ii) TITLE OF PAPER.....
- (iii) DATE OF SUBMISSION OF PAPER.....
- (iv) HAS THE PAPER BEEN ACCEPTED FOR PUBLICATION?.....
- (v) HAS THE PAPER BEEN PUBLISHED? .....

NB: ATTACH A COPY OF THE PAPER

NOTE: IF EXEMPTION IS TO BE SOUGHT FROM THE ABOVE REQUIREMENT, THE SECTION ON THE REVERSE SIDE OF THIS PAGE MUST BE COMPLETED.

SUPERVISOR'S COMMENTS .....

SUPERVISOR'S NAME..... G DE JAGER SIGNATURE.....

# UNIVERSITY OF CAPE TOWN



## Faculty of Engineering

30 November 1998

Dean's Office, Rondebosch, 7701  
Postal Address: University Private Bag, Rondebosch 7701, Republic of South Africa  
Telegraphic Address: "Alumni Cape Town"  
Telex No: 5-21439 · Telefax: (021) 650 3782  
~~Dean: Professor K M Rennie, Telephone (021) 650 2701~~  
Faculty Officer: J R Galvin, Telephone (021) 650 2698

Dean: Prof C T O'Connor Telephone (021) 650 2701

Mr P Reddy  
P O Box 1096  
STANGER  
4450

Dear Mr Reddy

I am pleased to inform you that the Examinations Board of the Faculty of Engineering has considered the examiners' reports on your dissertation and has resolved that your dissertation be passed. The Board also resolved that certain minor corrections to your dissertation, specified by the examiner(s), must be completed by you in consultation with your supervisor before the two unbound copies are deposited in the Library. I have sent the two unbound copies to your supervisor, together with the relevant examiners' reports. I shall be grateful if you would arrange to complete the corrections as soon as possible.

On behalf of the Faculty of Engineering, the Chairman of the Examinations Board (the Dean) has asked me to convey his congratulations to you on having qualified for your Masters degree and to wish you all the very best for the future.

Yours sincerely,

J R GALVIN  
FACULTY OFFICER  
for Registrar  
c:eng-let/sidtd17.doc

### IMPORTANT NOTES:

1. The University will not permit degree/diploma qualifiers to graduate if they have any outstanding University fees, fines, interest or dues. The date for payment of outstanding amounts including the examination fee of R1 000 is 5 June in the case of qualifiers for June graduation and 20 November in the case of qualifiers for December graduation.
2. Information on the graduation ceremony is sent to finalists in the first week of May (in the case of those expecting to graduate in June) and the first week in October in the case of those expecting to graduate in December. Contact the Students Records Office, (021) 650 2118, if you have any queries about the graduation ceremony or if you have not received this information.
3. The Faculty has a policy which allows for successful Masters degree candidates to submit their comments on the supervision they have received and on the quality of facilities available. We invite you to complete the enclosed form and to return it to the Dean at the above address.

cc HOD :  
Supervisor :  
encl.